



**Politecnico
di Torino**

Politecnico di Torino

Department of Mechanical and Aerospace Engineering

Master of Science Degree in Automotive Engineering

**Development of simplified
vehicle models for barrier impact**

Supervisor:

Alessandro Scattina

Candidate:

Grigorios Theodoridis



JRC

EUROPEAN COMMISSION

December 2022

Abstract

The scope of this thesis is the development of a generic vehicle model that will be used in the validation of the design of barriers for terrorist attack mitigation. More specifically, performing simulations of a vehicle colliding on specific barriers, to assess their structural integrity. These barriers are going to be used in city centres to protect areas that could be considered as potential targets for terrorist attacks. The model this thesis studies refers to a vehicle of the category N1 according to the standard IWA 14. It is designed by the company SVS FEM and co-developed in collaboration with the European Commission Joint Research Centre and Politecnico Di Torino. The model has to be simple enough, for the reduction computational cost, parametrizable, to easily modify the dimensions of the model within the N1 category, and to be code independent in order for the results of the simulations to not be affected by the solver used by the user. Literature studies have been conducted on the barrier design and the comparison between the two solvers, LS-Dyna which is the main tool for developing the model and Europlexus, a solver co-developed and used by the Joint Research Centre. The initial task of the thesis is to perform a verification of the model developed by SVS to assess the model's stability and proper operation. The next task is to perform a code comparison between the two solvers by performing sensitivity analysis on different parameters to parts extracted from the N1 Generic Vehicle Model, with increasing complexity, investigating possible differences between the two solvers, in order to develop a model that is independent from the software on which it is used.

Table of Contents

Abstract.....	ii
List of figures.....	v
List of tables	xi
1. Introduction.....	1
2. Barrier design.....	2
2.1. Definition of a barrier	2
2.2. Barriers against terrorist attacks.....	2
2.3. Use of vehicles as an attack median	4
2.4. Types of security barriers.....	5
2.4.1. Passive barriers	5
2.4.2. Active barriers	8
2.5. Certification.....	10
3. Finite element method.....	14
3.1. What is Finite Element Analysis (FEA)	14
3.2. How does FEA Work?	14
3.3. Advantages of Finite Element Method in the design process	15
3.4. LS-Dyna	16
3.5. Europlexus	16
3.5.1. From LS-Dyna to EPX.....	17
3.5.2. Contact model	17
3.6. Parallel computing for improvement of the computational cost.....	19
3.7. Mesh Quality and mass scaling.....	20
3.8. Simplification of the adopted vehicle numerical model.....	21
4. NI generic vehicle model development.....	22
4.1. Scope of the simulations.....	22
4.2. Vehicle model.....	22
4.3. Simulations	26
4.3.1. First task	27
4.3.2. Second task	28
4.3.3. Third task.....	31
5. EPX Simulations.....	35

5.1. Scope of the simulations.....	35
5.2. Stages of code comparison	36
5.3. Cross Beam Part.....	36
5.3.1. Code comparison with elastic material.....	37
5.3.2. Code comparison with different element formulations on elastic material	39
5.3.3. Code comparison with elastoplastic material (perfect plasticity law)	42
5.3.4. Code comparison with elastoplastic material (perfect plasticity law) with added mass.....	47
5.3.5. Code comparison with elastoplastic material with hardening curve.....	51
5.4. Submodel 1.....	57
5.4.1. Code comparison with elastic material	58
5.4.2. Code comparison with elastoplastic material	60
5.4.3. Code comparison with elastoplastic material on a refined mesh	62
5.5. Submodel 2	65
5.5.1. Code comparison with elastic material	67
5.5.2. Code comparison with elastoplastic material	69
5.5.3. Code comparison with elastoplastic material from NI vehicle model.....	72
5.6. Submodel 3	74
5.6.1. Code comparison of connections from both versions of NI and JRC model	77
5.6.2. Submodel 3 Frame mesh sensitivity analysis	82
5.6.2.1. Quadrilateral vs Triangular element comparison on frame	83
5.6.2.2. Quadrilateral vs Triangular element comparison on example from Dynaexamples	85
5.6.2.3. Quadrilateral vs Triangular elements comparison on frame mesh refining.....	88
5.6.2.4. Quadrilateral vs Triangular elements comparison on frame mesh refining control card effect.....	95
5.6.3. Submodel 3 remeshing	98
5.6.3.1. "Frame crush zone" remeshing without transitioning zone	98
5.6.3.2. "Frame crush zone" remeshing with transitioning zone	101
6. Conclusion and future work.....	105
Acknowledgements	108
Bibliography.....	109

List of figures

Figure 1 - Safety barrier [13]	2
Figure 2 - Security barrier [16]	3
Figure 3 - Vehicle ramming attacks [15]	4
Figure 4 - Laden weight per vehicle type [2]	5
Figure 5 - Round bollards [14]	6
Figure 6 - Concrete bollard [17]	6
Figure 7 - Jersey barrier [18]	6
Figure 8 - Concrete planters [19]	7
Figure 9 - Examples of street furniture [20]	7
Figure 10 - Difference between using manmade barriers with the use of natural elements as protective barriers [22]	8
Figure 11 - Retractable barriers [21]	9
Figure 12 - Road blocker [23]	9
Figure 13 - Retractable barrier [24]	10
Figure 14 - High security gate [25]	10
Figure 15 - Representation of a conventional contact method [11]	18
Figure 16 - Pinball concept and interpenetration of two pinballs [11]	18
Figure 17 - Domain decomposition for the tractor numerical model [7]	19
Figure 18 - N1 vehicle model (preliminary version)	22
Figure 19 - Geometry simplifications [12]	23
Figure 20 - Model design tree [12]	23
Figure 21 - Parametrizable masses	24
Figure 22 - Parametrizable dimensions	24
Figure 23 - N1 model Ackerman steering [12]	25
Figure 24 - Front axle degrees of freedom [12]	25
Figure 25 - Rear axle degrees of freedom [12]	26
Figure 26 - Vehicle impact on simple barrier	27
Figure 27 - Wall barrier impact energy balance	27
Figure 28 - Wall barrier impact resultant acceleration	28
Figure 29 - Wall barrier impact resultant contact force	28
Figure 30 - Vehicle impact on bollard	28
Figure 31 - Bollard impact (1000 kg cargo mass) energy balance	29
Figure 32 - Bollard impact (1000 kg cargo mass) parts with significant hourglass energy	29
Figure 33 - Parts with significant hourglass energy	29
Figure 34 - Parts linked to "Floor partition"	30
Figure 35 - Animation comparison of bollard impact (left) versus simple wall impact (right) on 1000 kg cargo mass	30
Figure 36 - Part "Floor reinforcement" behaviour on bollard impact (left) and simple wall impact (right) on 1000 kg cargo mass	30
Figure 37 - Bollard impact (1000 kg cargo mass) resultant acceleration	31
Figure 38 - Bollard impact (1000 kg cargo mass) resultant contact force	31
Figure 39 - Bollard impact (500 kg vs 100 kg) total and internal energy comparison	31
Figure 40 - Bollard impact (500 kg vs 100 kg) hourglass energy comparison with limit value of total energy of each cargo mass (5% of total energy)	32
Figure 41 - Bollard impact (500 kg cargo mass) parts with significant hourglass energy	32
Figure 42 - Bollard impact (100 kg cargo mass) parts with significant hourglass energy	32
Figure 43 - Animation comparison on bollard impact of 500 kg (left) vs 100 kg (right) cargo mass	33

Figure 44 - Part "Floor reinforcement" behaviour on bollard impact of 500 kg (left) vs 100 kg (right) cargo mass	33
Figure 45 - Bollard impact resultant contact force for all cargo mass cases unfiltered (top) and filtered (bottom)	34
Figure 46 - Bollard impact resultant contact force for all cargo mass cases unfiltered (top) and filtered (bottom) detailed initial peak.....	34
Figure 47 - Bollard impact for all cargo mass cases resultant acceleration	35
Figure 48 - Cross beam part extraction.....	36
Figure 49 - Cross beam part with indicated nodes for measurements.....	37
Figure 50 - Cross beam elastic material energy balance.....	38
Figure 51 - Cross beam elastic material node 32 x-axis acceleration	38
Figure 52 - Cross beam elastic material node 32 x-axis velocity.....	38
Figure 53 - Cross beam elastic material node 32 x-axis displacement.....	39
Figure 54 - Cross beam element formulation comparison total energy	40
Figure 55 - Cross beam element formulation comparison hourglass energy.....	40
Figure 56 - Cross beam element formulation comparison internal energy	41
Figure 57 - Cross beam element formulation comparison node 32 displacement.....	41
Figure 58 - Stress-strain curves of elastic material (left) and elastoplastic with perfect plasticity (right) [26]	42
Figure 59 - Cross beam with elastoplastic material (perfect plasticity) (@10 m/s) total energy	42
Figure 60 - Cross beam with elastoplastic material (perfect plasticity) (@10 m/s) internal energy	43
Figure 61 - Cross beam with elastoplastic material (perfect plasticity) (@10 m/s) hourglass energy with the corresponding limit values (5% of total energy).....	43
Figure 62 - Cross beam with elastoplastic material (perfect plasticity) (@10 m/s) node 32 x-axis displacement.....	43
Figure 63 - Cross beam with elastoplastic material (perfect plasticity) (@20 m/s) total energy	44
Figure 64 - Cross beam with elastoplastic material (perfect plasticity) (@20 m/s) internal energy	44
Figure 65 - Cross beam with elastoplastic material (perfect plasticity) (@20 m/s) hourglass energy with the corresponding limit values (5% of total energy).....	44
Figure 66 - Cross beam with elastoplastic material (perfect plasticity) (@20 m/s) node 32 x-axis displacement.....	45
Figure 67 - Cross beam with elastoplastic material (perfect plasticity) effective plastic strain at 10 m/s and 20 m/s	45
Figure 68 - Cross beam with elastoplastic material (perfect plasticity) residual kinetic energy of EL. FORM 2 (top) and EL. FORM 16 (bottom).....	46
Figure 69 - Cross beam with elastoplastic material (perfect plasticity) node 32 x-axis velocity of EL. FORM 2 (top) and EL. FORM 16 (bottom).....	47
Figure 70 - Punctual mass position	48
Figure 71 - Cross beam with elastoplastic material (perfect plasticity) with punctual masses (10 kg, 10 m/s) energy balance	48
Figure 72 - Cross beam with elastoplastic material (perfect plasticity) with punctual masses (10 kg, 10 m/s) node 32 x-axis displacement.....	48
Figure 73 - Cross beam with elastoplastic material (perfect plasticity) with punctual masses (10 kg, 10 m/s) effective plastic strain of EL. FORM 2 (top) and EL. FORM 16 (bottom)	49
Figure 74 - Cross beam with elastoplastic material (perfect plasticity) with punctual masses (20 kg, 20 m/s) energy balance	49

Figure 75 - Cross beam with elastoplastic material (perfect plasticity) with punctual masses (20 kg, 20 m/s) node 32 x-axis displacement	50
Figure 76 - Cross beam with elastoplastic material (perfect plasticity) with punctual masses (20 kg, 20 m/s) effective plastic strain of EL. FORM 2 (top) and EL. FORM 16 (bottom).....	50
Figure 77 - Cross beam with material from NI vehicle model internal energy at 10 m/s (top) and 20 m/s (bottom).....	51
Figure 78 - Cross beam with material from NI vehicle model (with density correction) total energy (@ 10 m/s).....	52
Figure 79 - Cross beam with material from NI vehicle model (with density correction) internal energy (@ 10 m/s).....	53
Figure 80 - Cross beam with material from NI vehicle model (with density correction) x-axis displacement of node 32 (@ 10 m/s).....	53
Figure 81 - Cross beam with material from NI vehicle model (with density correction) x-axis contact force (@ 10 m/s)	53
Figure 82 - Cross beam with material from NI vehicle model (with density correction) x-axis momentum (@ 10 m/s).....	54
Figure 83 - Cross beam with material from NI vehicle model (with density correction) total energy (@20 m/s).....	54
Figure 84 - Cross beam with material from NI vehicle model (with density correction) internal energy (@ 20 m/s)	54
Figure 85 - Cross beam with material from NI vehicle model (with density correction) node 32 x-axis displacement (@20 m/s)	55
Figure 86 - Cross beam with material from NI vehicle model (with density correction) x-axis contact force (@ 20 m/s)	55
Figure 87 - Cross beam with material from NI vehicle model (with density correction) x-axis momentum (@ 20 m/s).....	55
Figure 88 - Cross beam with material from NI vehicle model (with density correction) effective plastic strain maps (@20 m/s)	56
Figure 89 - Submodel 1 model extraction.....	57
Figure 90 - Submodel 1 parts.....	57
Figure 91 - Submodel 1 elastic material energy balance.....	58
Figure 92 - Submodel 1 elastic material internal energy by part.....	59
Figure 93 - Submodel 1 elastic material x-axis contact force.....	59
Figure 94 - Submodel 1 elastic material x-axis momentum	59
Figure 95 - Elastoplastic material proposed by JRC	60
Figure 96 - Submodel 1 elastoplastic material energy balance.....	60
Figure 97 - Submodel 1 elastoplastic material internal energy by part.....	60
Figure 98 - Submodel 1 elastoplastic material x-axis contact force.....	61
Figure 99 - Submodel 1 elastoplastic material x-axis momentum complete graph (top) and zoomed section (bottom)	61
Figure 100 - Submodel 1 elastoplastic material effective plastic strain maps.....	62
Figure 101 - Submodel 1 original model (left) and fine mesh model (right).....	62
Figure 102 - Submodel 1 elastoplastic material fine mesh (FM) and coarse mesh (CM) internal energy complete graph (top) and zoomed section (bottom)	63
Figure 103 - Submodel 1 elastoplastic material fine mesh (FM) and coarse mesh (CM) "Front bumper absorbing member" internal energy	63
Figure 104 - Submodel 1 elastoplastic material fine mesh (FM) and coarse mesh (CM) x-axis contact force	64
Figure 105 - Submodel 1 elastoplastic material fine mesh (FM) and coarse mesh (CM) x-axis momentum complete graph (top) and zoomed section (bottom).....	64
Figure 106 - Submodel 1 elastoplastic material fine mesh effective plastic strain maps.....	65

Figure 107 – Submodel 2 extraction	65
Figure 108 – Submodel 2 parts.....	66
Figure 109 – Submodel 2 with elastic material energy balance.....	67
Figure 110 – Submodel 2 with elastic material “Front vertical member” internal energy.....	68
Figure 111 – Submodel 2 with elastic material “Front bumper absorbing member” internal energy	68
Figure 112 – Submodel 2 with elastic material x-axis contact force.....	68
Figure 113 – Submodel 2 with elastic material x-axis momentum	69
Figure 114 – Submodel 2 with elastoplastic material energy balance.....	69
Figure 115 – Submodel 2 with elastoplastic material “Front vertical member” internal energy	70
Figure 116 – Submodel 2 with elastoplastic material “Front cross member” internal energy ..	70
Figure 117 – Submodel 2 with elastoplastic material x-axis contact force	70
Figure 118 – Submodel 2 with elastoplastic material x-axis momentum	71
Figure 119 – Submodel 2 with elastoplastic material effective plastic strain maps	71
Figure 120 – Submodel 2 model with elastoplastic material rotation upon impact with the wall barrier	72
Figure 121 – Submodel 2 with materials from N1 vehicle model energy balance	72
Figure 122 – Submodel 2 with materials from N1 vehicle model “Front vertical member” internal energy	73
Figure 123 – Submodel 2 with materials from N1 vehicle model “Front cross member” internal energy	73
Figure 124 – Submodel 2 with materials from N1 vehicle model “Front vertical member” x-axis momentum.....	73
Figure 125 – Submodel 3 model extraction.....	74
Figure 126 – Submodel 3 parts.....	75
Figure 127 – Connection between gearbox and drive axle	77
Figure 128 – Connection between gearbox and drive axle	78
Figure 129 – Submodel 3 energy balance.....	78
Figure 130 – Submodel 3 “Engine surface” internal energy.....	79
Figure 131 – Submodel 3 total energy.....	79
Figure 132 – Submodel 3 “Engine bolts” internal energy	79
Figure 133 – Submodel 3 internal eroded energy	80
Figure 134 – Submodel 3 x-axis contact force.....	80
Figure 135 – Submodel 3 x-axis momentum	80
Figure 136 – Parts connected by the constraint nodal rigid bodies (CNRBs) defined by the nodal set (NSET) 7 and 8.....	81
Figure 137 – Submodel 3 internal energy time evolution of parts “Frame longitudinal beams” (part 1), “Frame crush zone” (part 3) and “Front bumper absorbing member” (part 142)	82
Figure 138 – Frame quadrilateral element case (left) and triangular element case (right).....	83
Figure 139 – Frame quadrilateral vs triangular elements total energy	83
Figure 140 – Frame quadrilateral vs triangular elements internal energy	84
Figure 141 – Submodel 3 frame quadrilateral vs triangular elements x-axis contact force	84
Figure 142 – Frame quadrilateral vs triangular elements x-axis momentum	84
Figure 143 – Frame quadrilateral vs triangular elements effective plastic strain of quadrilateral elements of Europlexus (left) and LS-Dyna (right)	85
Figure 144 – Frame quadrilateral vs triangular elements effective plastic strain of triangular elements of Europlexus (left) and LS-Dyna (right)	85
Figure 145 – Simple tube.....	86
Figure 146 – Quadrilateral (left) and Triangular (right) element case.....	86
Figure 147 – Rigidwall (left) and DOF constraints (right)	86

Figure 148 – Simple tube example total energy.....	86
Figure 149 – Simple tube example internal energy.....	87
Figure 150 – Simple tube example eroded energy	87
Figure 151 – Simple tube example force vs displacement graph.....	87
Figure 152 – Frame mesh refinement cases of quadrilateral (top) and triangular (bottom) elements of original (left), fine (middle) and very fine mesh (right)	88
Figure 153 – Frame mesh refinement internal energy of original model (top), fine mesh (middle) and finer mesh (bottom)	89
Figure 154 – Frame mesh refinement internal energy of quadrilateral (top) and triangular (bottom) elements.....	90
Figure 155 – Frame mesh refinement total energy of quadrilateral (top) and triangular (bottom) elements.....	91
Figure 156 – Frame mesh refinement x-axis contact force of original model (top), fine mesh (middle) and finer mesh (bottom)	92
Figure 157 – Frame mesh refinement x-axis momentum of quadrilateral (top) and triangular (bottom) elements.....	93
Figure 158 – Frame mesh refinement crushing behaviour @ 5 ms of quadrilateral elements case of Europlexus (left) and LS-Dyna (right) of original mesh (top), fine mesh (middle) and very fine mesh (bottom).....	94
Figure 159 – Frame mesh refinement crushing behaviour @ 5 ms of triangular elements case of Europlexus (left) and LS-Dyna (right) of original mesh (top), fine mesh (middle) and very fine mesh (bottom).....	94
Figure 160 – Frame mesh refinement (CONTROL_SHELL influence) internal energy of quadrilateral (top) and triangular (bottom) elements.....	96
Figure 161 – Frame mesh refinement (CONTROL_SHELL influence) total energy of quadrilateral (top) and triangular (bottom) elements.....	96
Figure 162 – Frame mesh refinement (CONTROL_SHELL influence) x-axis momentum of quadrilateral (top) and triangular (bottom) elements.....	97
Figure 163 – Frame mesh refinement (CONTROL_SHELL influence) crushing behaviour @ 5 ms of triangular elements case of Europlexus (left) and LS-Dyna without control card (right) of original mesh (top), fine mesh (middle) and very fine mesh (bottom)	98
Figure 164 – Submodel 3 remeshing (without transitioning zone) original model (left) and modified model (right)	99
Figure 165 – Submodel 3 remeshing (without transitioning zone) modification on the CNRB connection on the remeshed version original connection (left) and modified connection (right).....	99
Figure 166 – Submodel 3 remeshing (without transitioning zone) energy balance.....	99
Figure 167 – Submodel 3 remeshing (without transitioning zone) “Frame longitudinal beams” internal energy.....	100
Figure 168 – Submodel 3 remeshing (without transitioning zone) “Frame cross member under engine” internal energy.....	100
Figure 169 – Submodel 3 remeshing (without transitioning zone) x-axis contact force	101
Figure 170 – Submodel 3 remeshing (without transitioning zone) x-axis momentum	101
Figure 171 – Submodel 3 remeshing (with transitioning zone) original model (left), fine mesh model (middle) and finer mesh model (right).....	102
Figure 172 – Submodel 3 remeshing (with transitioning zone) energy balance	102
Figure 173 – Submodel 3 remeshing (with transitioning zone) “Frame longitudinal beams” internal energy.....	102
Figure 174 – Submodel 3 remeshing (with transitioning zone) “Frame crush zone” internal energy.....	103

Figure 175 - Submodel 3 remeshing (with transitioning zone) "Engine surface" internal energy	103
Figure 176 - Submodel 3 remeshing (with transitioning zone) x-axis contact force	103
Figure 177 - Submodel 3 remeshing (with transitioning zone) x-axis momentum	104
Figure 178 - Submodel 3 remeshing (with transitioning zone) crushing behaviour @ 10 ms of "Frame crush zone" part @ 1 ms on original model (1), fine mesh model (2) and finer mesh model (3)	104

List of tables

Table 1 - Specifications for vehicle security barrier impact assessment [2]	11
Table 2 - Abbreviations for barrier performance ratings [2]	11
Table 3 - Vehicle classes and relevant weight [2]	12
Table 4 - Reference point locations and penetration rating [2]	12
Table 5 - Speed-up level for different number of sub-domains for the tractor numerical model [7]	19

1. Introduction

The scope of this thesis is to present the contribution of the Politecnico di Torino in the co-development, with the Joint Research Centre (JRC), of a generic vehicle model of the NI category. This model will be used to assess the structural rigidity of barriers used in city centers to protect specific areas that can be targeted for terrorist attacks. Chapter 2 is about the barrier design. The use of the vehicle as an attack method is the main drive for the design of barriers. The barriers are divided into different categories depending on whether they are static or can be operated by a user. The most significant barriers are mentioned, with the advantage they offer as well as a method of verifying the barrier's structural rigidity. Chapter 3 makes a reference on the finite element method. The advantages of the usage of FEM, as well as a reference on the two examined solvers. More specifically LS-Dyna, which is one of the software used worldwide for FEM studies and is also the solver used for the development of NI vehicle model, and Europlexus, a solver co-developed and used by the Joint Research Centre (JRC) as an FEM software. Chapters 4 and 5 are about the contribution of the Politecnico di Torino. Namely, chapter 4 contains the development of a preliminary version of the NI vehicle model, in order to verify the model's stability, correct operation, as well as its impact behaviour on a different type of barrier and modifications in cargo mass. Chapter 5 contains the comparison of the results of simulations between the LS-Dyna and Europlexus solvers on parts extracted from the NI Generic Vehicle Model. The simulations performed are based on a sensitivity analysis, modifying different geometrical features and discretizational methods. These analyses are performed to identify any differences between the two solvers, which are significant in the development a model that is independent from the software on which it is used.

2. Barrier design

2.1. Definition of a barrier

According to Merriam-Webster, a barrier is defined as “something material that blocks or is intended to block” or “a natural formation or structure that prevents or hinders movement or action” [1]. A barrier may come in different shapes, sizes, materials, can be manmade or naturally formed. Each type of barrier serves different purpose and has different usage. However, for the scope of this thesis, the barriers designed to mitigate terrorist attacks will be further analysed.

2.2. Barriers against terrorist attacks

In most terrorist attacks, usually the main target is critical infrastructures and public spaces. Normally, these locations have modest or insufficient protection measures. Thus, a tendency has appeared of using vehicles as a ramming median driven at high speed in order to inflict maximum human casualties or transport an improvised explosive device (IED). Over the last decades, various physical protection measures have been developed and applied to these targets. However, these measures are not made specifically for each individual target, resulting in a need for implementing simple and unique solutions for protecting these targets. The aforementioned barriers should be designed to stop an ill-intentioned vehicle that attempts to breach the perimeter of the target and should be placed strategically in order to reduce the speed of the attacking vehicles at a level that will deem them incapable to produce damaging consequences and human casualties. Their layout can also be adapted according to the



Figure 1 - Safety barrier [13]

topography of the target (e.g., can take the form of concrete sitting benches, flower planters, artistic elements, sculptures). Vehicle barriers are divided into two major categories, security barriers and safety barriers. This categorization is a difficult task because of the similarities between them. Safety barriers (figure 1) are used for preventing and/or mitigating the results of an accident (errant vehicle) that can result in life loss, injuries, or environmental destruction. On the other hand, vehicle security barriers (figure 2) are adopted for creating a physical obstacle against unauthorized entry and other form of relevant attacks, aiming at protecting human life and damage of property [2]. Additionally, they can act as a deterrence, functioning as a psychological obstacle against aggressors who are planning an attack [2].



Figure 2 - Security barrier [16]

2.3. Use of vehicles as an attack median

The most popular medium for terrorist attacks is the vehicle. Many vehicle types are eligible for selection to perform a terrorist attack, from small passenger cars to large trucks, with various weight (figure 3). Thus, the most important parameter for a proper design of a security barrier is to calculate the vehicle's kinetic energy at the time of the impact. This parameter depends on the weight and the maximum attained speed of the vehicle.




Vehicle-ramming attacks						
Major deadly attacks using vehicles since July 2016						
						
Nice, France	Berlin, Germany	Jerusalem	London, Britain	Stockholm, Sweden	London, Britain	London, Britain
July 14, 2016	December 19, 2016	January 8, 2017	March 22, 2017	April 7, 2017	June 3, 2017	June 19, 2017
Vehicle used: Truck	Truck	Truck	Car	Truck	Van	Van
Rams into crowd on Promenade des Anglais on night of Bastille Day	Slams into crowd of people at Christmas market	Rams into group of Israeli soldiers visiting a tourist spot	Drives into pedestrians on bridge near parliament and fatally stabs a policeman	Mows down shoppers before ploughing into facade of department store	Runs over pedestrians on London Bridge, people stabbed in nearby market	Rams worshippers leaving a mosque
Killed: 86	12	4	4 by ramming	4	4 by ramming, 4 more in stabbings around 50	At least 1
Injured: at least 300	more than 40	at least 15	more than 30	around 15		about 10
Attacker Mohamed Lahouaiej Bouhlel Tunisian	Anis Amri Tunisian	Fadi al-Qunbar Palestinian	Khalid Masood British	Rakhmat Akilov Uzbek	Khuram Butt (British) Rachid Redouane (Moroccan-Libyan) Youssef Zaghba (Italian-Moroccan)	48-year-old-man
Shot dead at the scene by police	Shot dead by Italian police in Milan, Dec 23	Shot dead at the scene by security forces	Shot dead at the scene by police	Arrested several hours after the attack	Shot dead by police	Detained by members of the public then arrested by police

Figure 3 - Vehicle ramming attacks [15]

Vehicle weight can differ according to the type of vehicle used and its loading capacity. This is especially important when considering trucks. The heavier the vehicle, the higher the threat that it opposes. The standard CWA 16221, 2010, presents some weight values when assessing the design according to the vehicle type (figure 4). To calculate the maximum attained vehicle speed, several parameters must be taken into consideration, such as:

- Initial velocity
- Average acceleration
- Distance between the starting point of the vehicle and the barrier

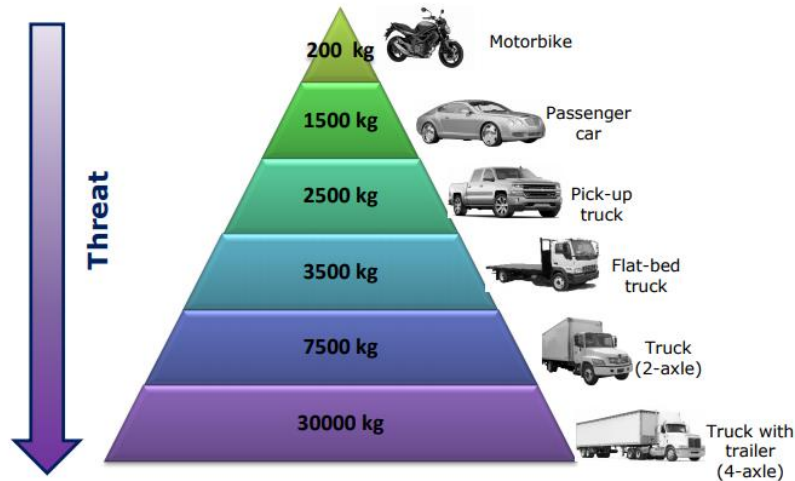


Figure 4 - Laden weight per vehicle type [2]

2.4. Types of security barriers

As described before, security barriers are designed to be capable of stopping a malevolent vehicle breaching the perimeter of a specific area, causing physical damage and human casualties. These barriers are not meant to be used for security reasons. Hence, their goal is not to prevent a vehicle from having an accident, but to stop a vehicle from breaching a given perimeter by absorbing its kinetic energy. Security barriers are divided into passive and active, according to if they are static or if they can be moved, into passive and active.

2.4.1. Passive barriers

These are not equipped with moving parts. The impact energy is absorbed either through strong foundation or by the combined effect of their weight and road friction coefficient.

- Bollards. Bollards are the most preferred barriers. They are versatile, effective, easy to install and produce. Due to their versatility, they can



Figure 5 - Round bollards [14]

be adapted to many shapes and sizes, to fit the surrounding environment (figures 5 and 6). The preferred materials are steel, reinforced concrete, or a combination of both. Their performance depends on the depth and size of their foundation, as long as they are not intervening with underground utilities. Thus, their positioning should be carefully considered, or a more modern shallow base solution should be adopted.



Figure 6 - Concrete bollard [17]

- Temporary barriers. These are re-deployable solutions used in city centres, usually during public events. These barriers rely on their mass in order to either stop a vehicle or progressively halt and incapacitate



Figure 7 - Jersey barrier [18]

a vehicle through the developed friction forces. If they are not anchored or connected, they are limited to stop light vehicles at low speeds. Due to their size, their presence may act as a deterrence and can psychologically influence potential aggressors, but they also create a false sense of security to building inhabitants [2]. The most common temporary barriers used are the Jersey barriers (figure 7), which are precast concrete elements originally used for highway safety, and planters (figure 8) which is an attractive, easy to manufacture and easy to transport solution. Additionally, they are filled with soil (since they host plants) which increases their mass, thus making them more effective as a barrier.



Figure 8 – Concrete planters [19]

- Street furniture. Streetscape elements, such as bus stops, kiosks, signposts, sculptures, trash bins, benches etc. can be integrated into the urban setting seamlessly while providing sufficient levels of security against penetrative attacks (figure 9). An important aspect in the design of these elements, is that they must meet specific performance criteria in order to intercept vehicle penetrative attacks.



Figure 9 – Examples of street furniture [20]

- Landscape. Exploiting the topography for upgrading the security of a certain site, is the most unobtrusive solution. Natural formations (forests, lakes, rivers, berms, pools, ponds etc.) can be used as a protective barrier. If they are absent, the terrain can be appropriately shaped to create formations that cannot be cut across by a moving vehicle, for example to create berm or ditches, to plant trees and to create streams. These formations however may need extensive maintenance and must be properly designed in order to properly incapacitate a vehicle and also to be a minimal obstruction to security forces. Using the natural landscape as a protective measure creates also a very pleasing effect while providing a sufficient level of security. However, this means that in city centres, where there is limited available space, such measures require a complete revision of the urban management plan, which is not always feasible (figure 10).



Figure 10 - Difference between using manmade barriers with the use of natural elements as protective barriers [22]

2.4.2. Active barriers

These types of barriers are equipped with moving parts. They are used in area where there is need for pass through of authorized vehicles (such as parking lots), or if there is a need to block the traffic for a specific time. These barriers may be driver operated, or operated from an external source (e.g., a guard). Due to the moving parts, considerable maintenance of the mechanical system is required.

- Retractable bollards. These bollards remain in a raised position and retract to allow vehicle entrance (figure 11). They can be manually lowered or lowered by using a hydraulic or pneumatic unit. Their great advantage is that it is the least intrusive solution for pedestrian crossing (either raised or retracted). However, it is an expensive solution which requires deep and wide foundations.



Figure 11 - Retractable barriers [21]

- Road blockers. It is a ramp system which characterized by a metal plate that is visible at the surface of the road. When raised this metal plate is angled upwards and disables unauthorized vehicle entrance (figure 12). They are operated hydraulically or electrically, and they offer great protection, without the need for deep foundations. However, due to their size, they may block pedestrian and bicycle access.



Figure 12 - Road blocker [23]

- Drop arm barriers. These barriers consist of a steel arm that is usually supported by properly anchored concrete elements. The steel arm is pneumatically or hydraulically actuated. This is a typical solution often used at parking lots and tool booths (figure 13). It may act as a

deterrent but lacks the stopping force of the more reinforced versions of the active barriers.



Figure 13 - Retractable barrier [24]

- Gates/fences. They are a common security element, and they are usually part of a perimeter fence system (figure 14). Operation is performed either manually or automatically. The selection of a gate capable of stopping incoming threat vehicles is of high importance, as many of the commercially available systems provide low protection, and their operation occur at low speed.



Figure 14 - High security gate [25]

2.5. Certification

In order to verify the barrier's structural integrity and its ability to properly immobilize an incoming vehicle, several tests have been developed to quantify and certify its performance. Many test specifications have been developed, but a universally accepted test methodology is not yet available. Thus, security barriers available in the market, may have been tested under different scenarios according to the standard used, which means that their

performance is presented in a different manner. Additionally, the test standards are developed to access the performance of permanent barriers and not movable and temporary barriers, which imposes a significant

Abbreviation	Type of technical specification	Standardization body	Valid until
IWA 14-1:2013	Workshop agreement	ISO (International Organization for Standardization)	12/2019*
PAS 68:2013	Consultative document	BSI (British Standards Institute)	08/2016
CWA 16221	Workshop agreement	CEN (European Committee for Standardization)	08/2017
ASTM F2656	Standard	ASTM (American Society for Testing and Materials)	01/2023

*(currently under revision)

Table 1 - Specifications for vehicle security barrier impact assessment [2]

obstacle in verifying additional perimeter protection solutions. The most common standards used are displayed on table 1. The performance of vehicle security barriers is demonstrated with the use of certain

<p>IWA 14-1:2013</p> <p>PAS 68:2013</p> <p>CWA 16221</p>	<p><u>X/VS_B/W[A]/V/θ:P/D</u></p> <p><u>X/VS_B/[A]W/V/θ:P/D</u></p> <p>where: X = test type VS_B = security barrier type A = vehicle classification W = vehicle weight [kg] V = vehicle velocity [km/h] θ = angle of impact [deg] P = vehicle penetration [m] D = dispersion of debris [m]</p>
<p>ASTM F2656</p>	<p><u>A/V/P</u></p> <p>where: A = vehicle classification V = vehicle velocity [mph] P = penetration rating</p>

Table 2 - Abbreviations for barrier performance ratings [2]

abbreviations. These indicate the conditions under which the barrier has been tested (table 2). For these tests, vehicle weight is predefined according to the vehicle classification. Also, the vehicle velocity has predefined values at which the tests are concluded (table 3). Vehicle penetration (P) is the distance the attack vehicle travelled after its impact with the security barrier and until it stops. Each testing standard measures this distance differently (for example the standard ASTM2656 has the Penetration rating, which is calculated from the penetration distance and takes only three values

Test standard	Vehicle type	Vehicle classification	Vehicle weight [kg]	Vehicle test speed [km/h]
IWA 14-1:2013	Car	M1	1500 (±75)	16,32,48,64,80,96,112
	Pick-up	N1G	2500 (±75)	16,32,48,64,80,96,112
	Flat bed	N1	3500 (±100)	16,32,48,64,80,96
	Day cab	N2A,N2B,N3C,N3D	7200 (±400)	16,32,48,64,80
	Day cab	N3E	24000 (±400)	16,32,48,64,80
	Day cab	N3F	30000 (±400)	16,32,48,64,80
CWA 16221 PAS 68	Car	M1	1500 (±50)	16,32,48,64,80,96,112
	Pick-up	N1G	2500 (±50)	16,32,48,64,80,96,112
	Flat bed	N1	3500 (±100)	16,32,48,64,80,96
	Day cab	N2	7500 (±100*)	16,32,48,64
	Day cab	N3 (2-axle)	7500 (±150)	16,32,48,64,80
	Day cab	N3 (4-axle)	30000 (±600)	16,32,48,64,80
ASTM F2656	Car	SC	1100 (±25)	50,65,80,100
	Sedan	FS	2100 (±50)	50,65,80,100
	Pick-up	PU	2270 (±50)	50,65,80,100
	Standard truck	M	6800 (±140)	50,65,80
	Class 7 cab-over	C7	7200 (±150)	50,65,80
	Heavy truck	H	29500 (±590)	50,65,80

*At PAS 68 (±150)

Table 3 - Vehicle classes and relevant weight [2]

according to the interval which the distance is located) and it also depends on the type of barrier and vehicle category (table 4). Dispersion of debris (D) shows the distance of detached vehicle, ballast or barrier pieces of

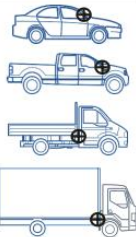
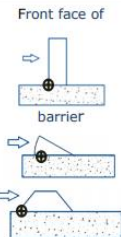
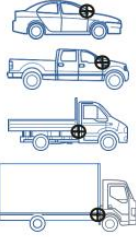
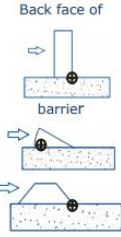
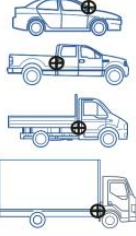
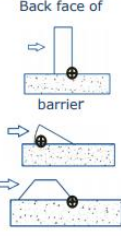
Test standard	Vehicle reference point	Barrier reference point	Penetration rating
IWA 14-1:2013		Front face of barrier 	-
CWA 16221 PAS 68		Back face of barrier 	-
ASTM F2656		Back face of barrier 	P1 (P≤1m) P2 (0m<P≤7m) P3 (7m<P≤30m)

Table 4 - Reference point locations and penetration rating [2]

significant size (weight ≥ 25 kg) from the barrier reference line. Because the test vehicle's weight and speed are available for each test, the vehicle's kinetic energy at impact can be calculated and used as an upper limit when selecting an appropriate protective barrier. These values may be compared with the kinetic energy calculated through the developed attack scenario to determine the most appropriate security barrier [2]. The resulting penetration distance and response of each barrier does not depend only on weight, class and velocity of the vehicles as depicted by their various standards. The geometrical features of the test vehicles are a crucial parameter and vary according to each market, for example US-type vehicles are usually greater in dimensions than European-type. To avoid such discrepancies, selection of the correct barrier should correspond to the predominant vehicle types in the country which the barrier study is performed.

3. Finite element method

3.1. What is Finite Element Analysis (FEA)

FEA is a computer-based process used for modelling complex products and systems. These simulations occur in a virtual environment for the purpose of 'solving' or finding a series of solutions to potentially complex performance issues. It is useful for all degrees of science and engineering disciplines [3]. FEA works by breaking down a large structure, with high degrees of physical complexities and mathematical discontinuities, into smaller, more manageable sections. Each section represents the material properties of its local domain. By slicing the structure into smaller and smaller sections, the simulator gains an understanding of how the larger structure will respond to external or internal stimuli [3].

3.2. How does FEA Work?

The first step of the process is to determine the placement of the "nodes" on the structure. The node is a single point within the 2D or 3D structure. Each node is programmed with the material and structural data of its immediate location [3]. Between the nodes, lines are added to create a structure called mesh, which encloses smaller and simpler sections of the complete part. As the density of the mesh increases, the precision of the results increases, but also computational time and complexity. The regions that are enclosed by the mesh structure are a collection of finite elements, hence, Finite Element Analysis [3]. The elements are defined by simpler equations concerning stress, force, inertia, thickness, strength, acceleration, temperature, etc. in relation to the border conditions along that mesh and those conditions within the element. The software lists the individual elements, their neighbouring elements, and the internal and border conditions. These previously mentioned equations, within the system, are solved at the same time. The results of these equations are used to determine the response of each node when external stimulus is applied to it, or to its neighbouring elements. When a simulation program is executed and stressors are applied to the system, each element begins to adjust its equations [3]. These adjustments will either relieve or create additional stresses throughout the mesh, changing border conditions for its neighbours, just as its neighbours will change its own border conditions [3].

If the programming of the nodes and meshes is performed properly, the system eventually works out all the work all the stresses out of the equations and begin to settle. This settling of the results and the creation of a solution is called "convergence". This solution is applied to each node and a theoretical stress and deflection function for each section of the structure is calculated. The mesh density defines the precision of the response of the local region of the part. Higher node density returns a more accurate result, but the higher the mesh density (i.e., higher number of nodes in a region), more computations are required to obtain a converging result, extending the run-time of the simulation and memory usage of the system. Thus, an increased mesh density should be used in critical points of interest (e.g., regions receiving large amounts of stress or deformation), while maintaining as small as possible mesh density on the rest of the part.

3.3. Advantages of Finite Element Method in the design process

- Increased accuracy. Using FEA requires the designer to create and maintain a 'recipe' of all material parameters for a prototype during its development. With this 'recipe', the designer can model all physical stresses on a part, even those that might be overlooked on initial designs, bringing an immediate increase in accuracy when designing a product.
- Enhanced design. Using FEA when developing a product, a designer can determine how stresses within one piece will affect the materials in another separate, but connected, piece, since it is possible to model an entire system instead of modelling each part separately.
- Better insight into critical design parameters.
- Virtual prototyping. Since initial physical prototypes are very expensive and time consuming to make (and are usually a very crude version of the initial design) designers can simulate the system in FEA software and model different design iterations and materials in very short time, versus the long procedure of hard prototyping.
- Fewer hardware prototypes. Higher-fidelity simulations with faster hardware allows developers to invest in virtual testing much earlier in the process than in the past, thus forcing the designer to rely on fewer

physical prototypes, by uncovering or confirming suspect results throughout the prototyping and manufacturing lifecycle.

- Faster and less expensive design cycle. Creating different design iterations is no longer dependent upon machine shop and manufacturing schedules. Each new design can be virtually tested very quickly compared to a physical prototype.
- Increased productivity and revenue. The use of FEA software allows a company to produce better quality products in a shorter design cycle and with less waste of material and time.

3.4. LS-Dyna

One of the leading software used for finite element simulation is LS-Dyna. LS-DYNA is an advanced general-purpose multiphysics simulation software package developed by the former Livermore Software Technology Corporation (LSTC) (acquired by Ansys in 2019). Its origins and core-competency lie in highly nonlinear transient dynamic finite element analysis (FEA) using explicit time integration. LS-DYNA is used by the automobile, aerospace, construction and civil engineering, military, manufacturing, and bioengineering industries, due to the program's wide spectrum of possibilities for the calculation of many complex real-world problems.

3.5. Europlexus

Europlexus (or EPX) is a simulation software, developed and co-owned by the Commissariat à l'Énergie Atomique et aux Énergies Alternatives (French Alternative Energies and Atomic Energy Commission) (CEA) and the Joint Research Centre of the European Commission (EC/JRC), used to analyse fast transient phenomena regarding structures and fluids in interaction [4]. EPX is based on a space discretization by means of finite elements, SPH particles (Smooth Particle Hydrodynamics) or discrete elements for structures, or by means of finite elements, finite volumes or SPH particles for fluids [4]. Time integration is achieved through a conditionally stable explicit scheme [4], similar to LS-Dyna. The solving algorithm allows different types of non-linearities at both geometric (large displacements; large rotations) and material level (constitutive laws implementing plasticity or damage for example) [4]. The program provides a large number of possibilities for kinematic links between entities, for instance for boundary

conditions, contact between structures or fluid-structure interaction. Contrary to LS-Dyna where most of the kinematic constraints are implemented by using the penalty method, in EPX the purely numerical penalty coefficients can be avoided by applying the Lagrange Multipliers method, where the reaction forces of a given constraint are computed a priori, by solving an additional linear system involving the constrained degrees of freedom [5]. EPX implements specific models able to analyse various mechanical situations, such as shocks, impacts, explosions, wave propagations and their consequences on structures [6]. Spatial discretization for structures is mainly achieved through finite elements, but some meshless models, such as SPH particles, or discrete models are also available [6]. Similar to LS-Dyna, EPX implements various, generally non-linear, constitutive laws for metallic structures (Von Mises laws [perfect, with isotropic or kinematic hardening, with dependency to the strain rate...] and Johnson-Cook law).

3.5.1. From LS-Dyna to EPX

The “.k” input file of LS-DYNA, is the most popular format used in explicit FE analysis, which is also supported by Europlexus. In particular, Europlexus can read all the keywords which could be prohibitively long to convert manually, such as coordinates of the nodes and their connectivity (that define the finite elements), the definition of the groups (SETs and PARTs) and nodal constraints. However, at present, some keywords like those concerning the material properties and the contact surface definition, which are more code specific and appear in very limited number of instances, need to be converted manually from LS-Dyna to Europlexus.

3.5.2. Contact model

The mechanical contact-impact behaviour of a vehicle crash is characterized as fast impact or crash test problem, where the friction can be neglected, and large deformation of the involved bodies may occur [7]. Conventional contact-impact methods of sliding surfaces [8] based on “slave” nodes and “master” surface are widely used in the FEM analyses [7]. Contact-impact algorithms usually consist of two main components:

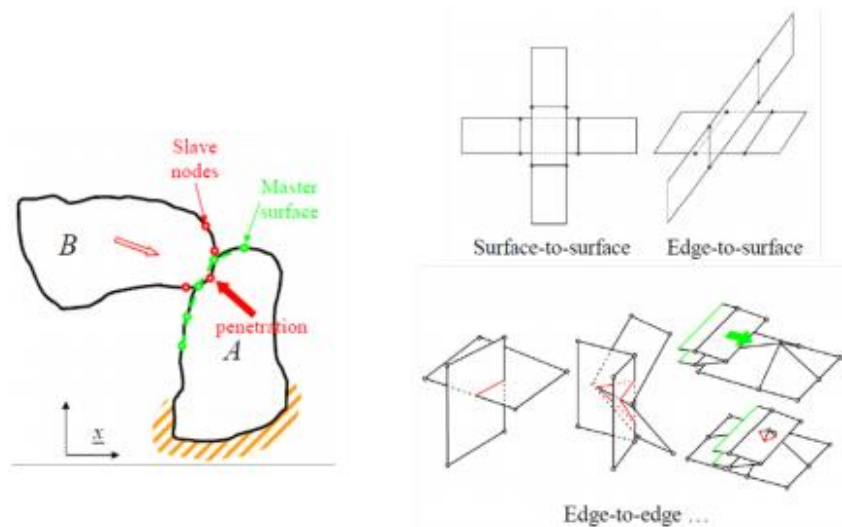


Figure 15 - Representation of a conventional contact method [11]

1. The contact detection module, which is realized by means of node through surface penetration algorithms (figure 15).
2. Contact enforcement technique, which can be introduced via penalty or Lagrange multipliers methods.

Conventional techniques are efficient but suffer from drawbacks related to the node penetration algorithm robustness. The main idea of the pinball algorithm is to enforce the impenetrability condition via a set of spheres (pinballs), which are embedded in the finite elements [7] (figure 16). The contact relationships have been introduced via the Lagrange multipliers method, in order to obtain a reference solution, independent from any kind of calibration of the penalty coefficients [7].

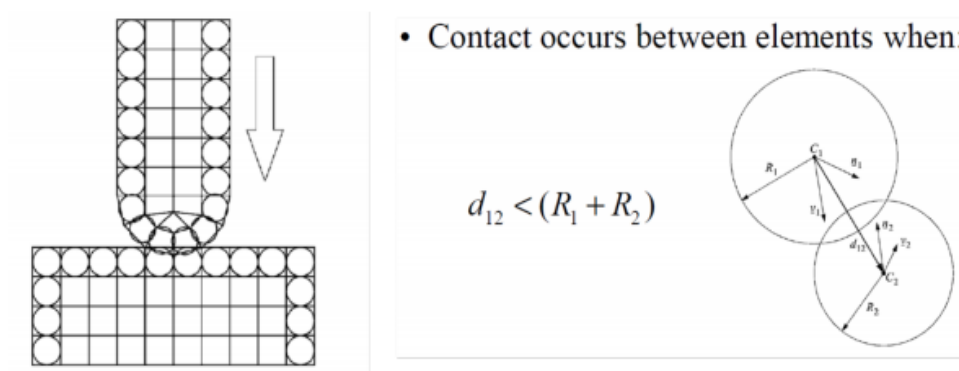


Figure 16 - Pinball concept and interpenetration of two pinballs [11]

3.6. Parallel computing for improvement of the computational cost

An important parameter for the industrial use of numerical simulation is the computational cost. To keep the cost low, the approach of parallel computing through domain decomposition is used. The whole model is split into smaller sub-domains (figure 17) where each sub-domain can be

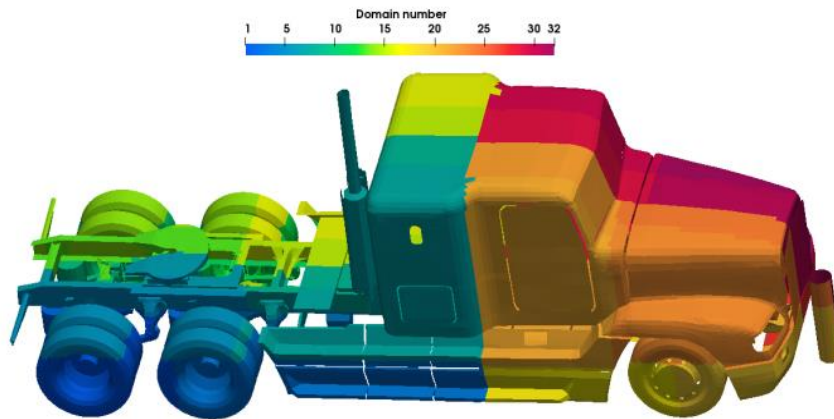


Figure 17 - Domain decomposition for the tractor numerical model [7]

analysed in a different processor at the same time (in parallel). Explicit FE analysis shows a very high scalability level which means that a big number of processors can be engaged to speed up the calculation. High level of scalability implies that, as the number of processors is increased, the speed-up of the computation is increased in a similar manner [7]. For the example with the tractor, the performance of the simulations is shown on table 5. As the number of processors increases, the speed up increases as well (the computational cost decreases). For 4 processors the speed-up is 3.7, which

Number of processors	CPU time [h]	Speed-up
1	300	-
4	81	3.7
8	46	6.5
16	24	12.5
32	18	16.7
64	18	16.7

Table 5 - Speed-up level for different number of sub-domains for the tractor numerical model [7]

is very close to the highest possible value (4). For more processors, the rate of the speed-up increases until the 64 processors, where the speed-up is the same as with 32 processors [7]. This phenomenon is related to model size and the required time for communication between the sub-domains. A fraction of the analysis cost is always dedicated to the communication of each sub-domain with the central processor that forms the complete solution. When the size of the sub-domain is becoming small, then the communication time is becoming significant compared to the computational cost (operations on the elements) [7].

3.7. Mesh Quality and mass scaling

To access the element quality the following criteria are used:

- Aspect ratio: The ratio of maximum element edge length to the minimum length (typical threshold: 3).
- Jacobian: Value of the determinant of the Jacobian matrix calculated for each integration point of the element, the reported deviation is calculated as the ratio of the smallest value over the largest (typical threshold: 0.7).
- Skewness: The deviation of an element's angles from 90° for quadrilateral elements and 60° for triangular elements (typical threshold: 45°).
- Tapering: Angular distortion of quadrilateral elements (typical threshold: 0.25).
- Crash time step: Time needed for a sound wave to travel through an element (typical threshold: 10^{-6} s).

These criteria are related to access the mesh quality of the model in explicit solvers, related to the scope of this thesis. A finite element numerical model with less than 10% of its elements failing the quality criteria is considered acceptable. The time step is controlled by the minimum dimension of the smallest element of the FE mesh in combination with its sound speed, therefore, the mesh size shall be a trade-off between the need for geometrical and numerical accuracy and computational cost: large elements guarantee a large time step but poor model accuracy, while smaller elements provide better accuracy but smaller time step [7]. This is the most important for explicit approaches since it is associated with the

computational cost. Smaller integration time step results to higher number of steps, thus increased CPU time. Explicit integration schemes are conditionally stable. Therefore, the integration time step must be lower than the lowest time a sound wave takes to cross a finite element. The critical time step is related to the material properties and element size. To increase the critical time step, if necessary, the mass scaling technique is applied, where a small amount of mass is added (via the density of the elements) to a limited number of elements in order to increase it. This scaling should be kept as low as possible (less than 2 %), because it may affect the impact results, and it should not be concentrated in critical areas.

3.8. Simplification of the adopted vehicle numerical model

Crashworthiness analysis of a vehicle and security barrier impact tests have fundamental differences. The main focus of the vehicle industry is on the safety aspects related to car impact, by examining vehicle behaviour and consequences on the driver's health. In contradiction with the primary objective of barrier impact tests, which is to define a robust and effective protective structure. In result, barrier analysis concentrates on different aspects, such as the barrier's geometrical details, material characteristics and boundary constraints. Thus, the numerical complexity should focus on the barrier and not on the whole vehicle model. To guarantee the validity of the results, the numerical representation of the vehicle must be accurate enough so that its response is identical to the real vehicle. A simplified numerical model should have the right balance between simulating both the vehicle and the barrier, even if the study of the barrier is the focus of these simulations. Therefore, some parts of the vehicle model can be omitted or substituted by simpler components, leading to the formation of generic numerical models that correspond to different vehicle weight classes. This can be a cost-efficient performance assessment of safety barriers, since it would allow the simulation of different vehicle types impacting a single barrier type, and not the use of only one vehicle, as is usually the case in physical tests (resulting in the certification of a single impact scenario) [7].

4. NI generic vehicle model development

4.1. Scope of the simulations

The initial work performed by Politecnico di Torino, is to contribute on the development of a generic vehicle model of the category NI. The term generic is referred to the design of the model, that does not include brand depending features and that the user can adjust different parameters to describe most of the vehicles within the NI category. The objective of this vehicle model is to simulate impacts on barriers and assess the resistance of given barriers, in a short amount of time. Hence short runtime is another target of this model, besides the target of the generic design.

4.2. Vehicle model

The model is made by the company SVS FEM (figure 18). The NI category according to the IWA 14 standard is:

- Day cab vehicle – flatbed
- Rear wheel drive
- Vehicle mass: 3500 ± 100 kg
- Overall vehicle length 6200 ± 380 mm
- Wheelbase length 3805 ± 710 mm

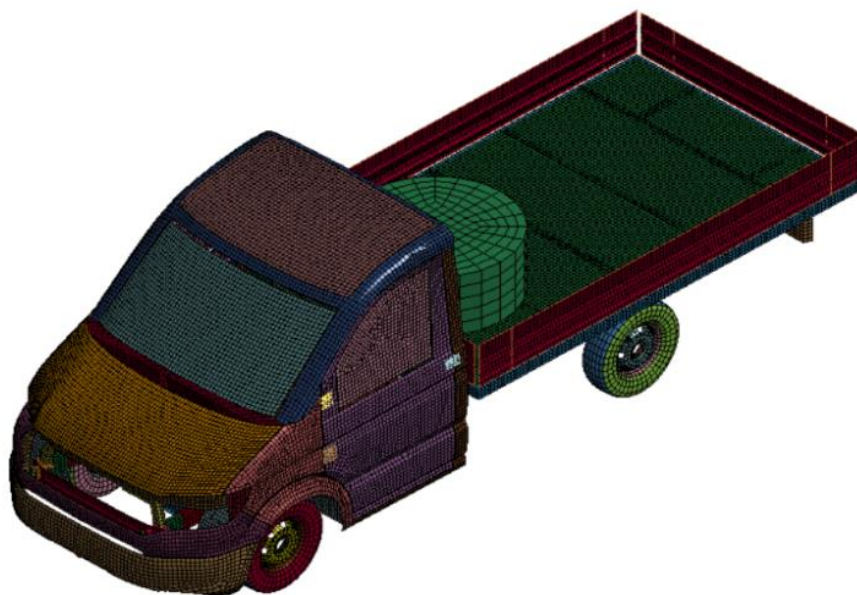


Figure 18 - NI vehicle model (preliminary version)

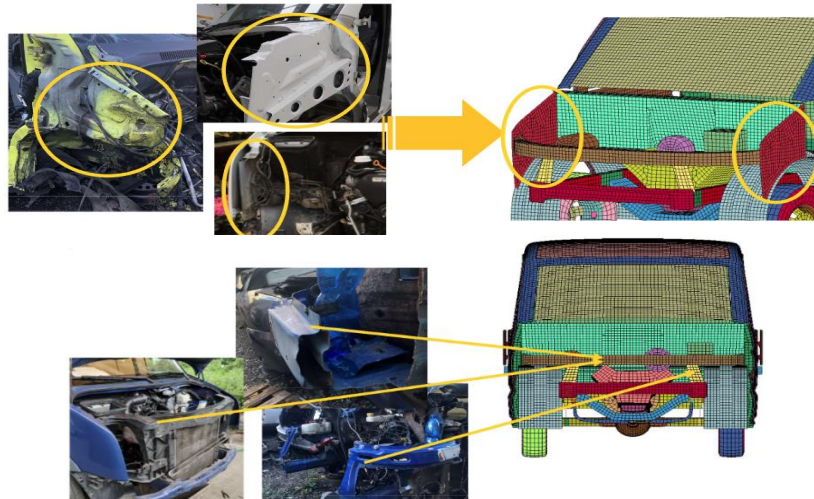


Figure 19 - Geometry simplifications [12]

Although the design of the model is based on the VW Crafter, Ford Transit tipper and Fiat Ducato, by eliminating brand depending features, design details (figure 19) and model uncertainties (age of vehicle, vehicle condition, etc.) the model runtime shortens. Concurrently, by maintaining the parameters necessary to describe a vehicle of this category (mass, length, wheelbase, etc.), the results of any modifications made to the desired parameters can be assessed in a short amount of time. The CAD version of the model was developed with the software Ansys SpaceClaim. The vehicle model has been split into sub-parts (figure 20) and each part to a different ".k" file, for meshing and more control on the design of each part.

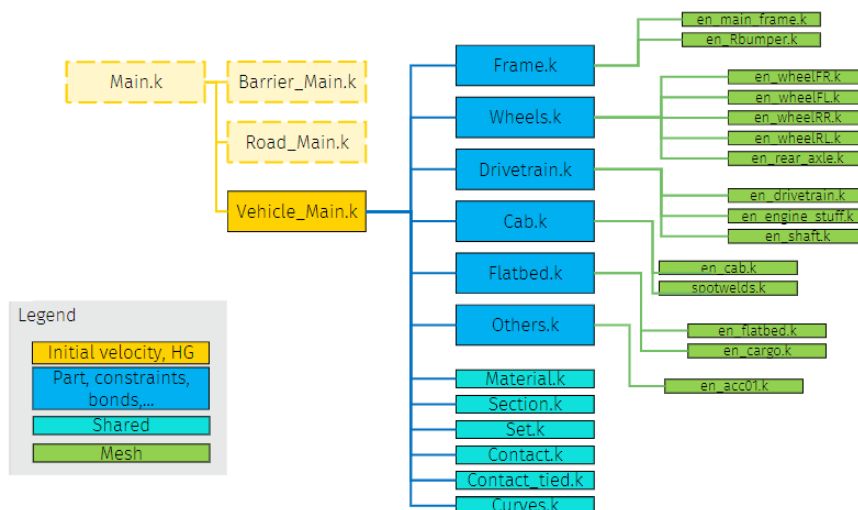


Figure 20 - Model design tree [12]

To simulate all the vehicles in the NI category, as close as possible, the model is parametrised to be able to change the dimensions and characteristics. The adjustable parameters are:

- Mass of different parts (figure 21):
 - Cargo
 - Cab
 - Frame
 - Engine
 - Gearbox

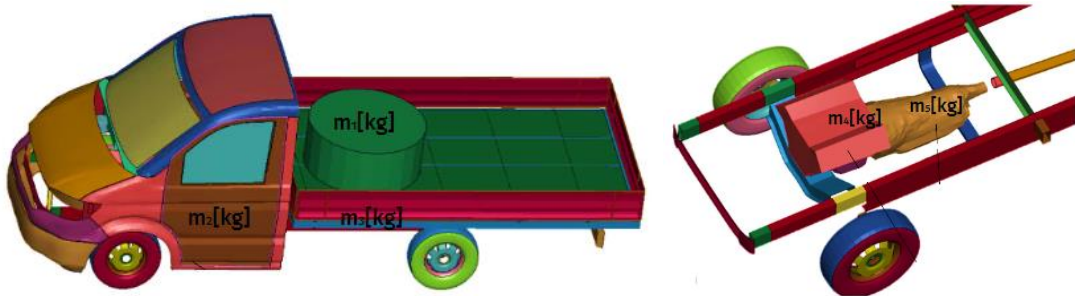


Figure 21 - Parametrizable masses

- Suspension properties:
 - Upper and lower bound
 - Suspension Stiffness
 - Damping properties
- Front crash stiffness of absorbing parts
- Dimensions of vehicle and position of cargo (figure 22):
 - Vehicle length
 - Wheelbase length
 - Ground clearance
 - Wheel track
 - Position of cargo (X axis)
 - Position of cargo (Y axis)

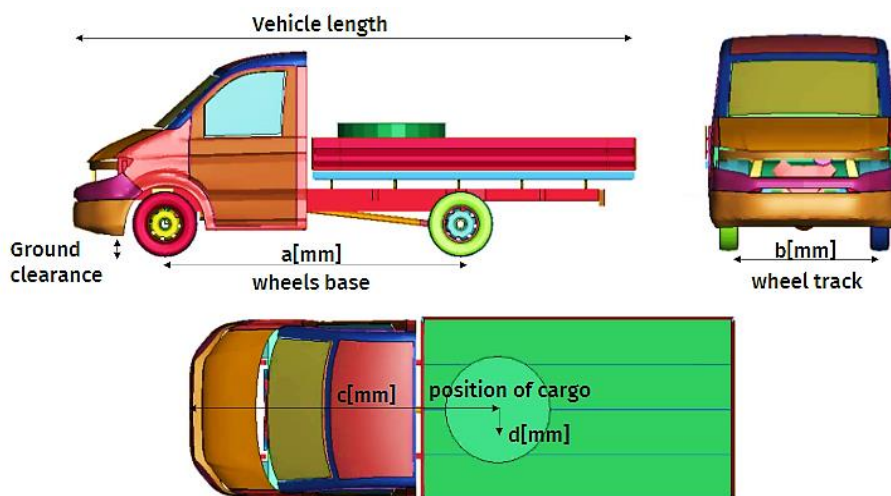


Figure 22 - Parametrizable dimensions

The vehicle model is developed with independent suspension at the front and a rigid axle in the back. The steering is considered an Ackerman system (figure 23).

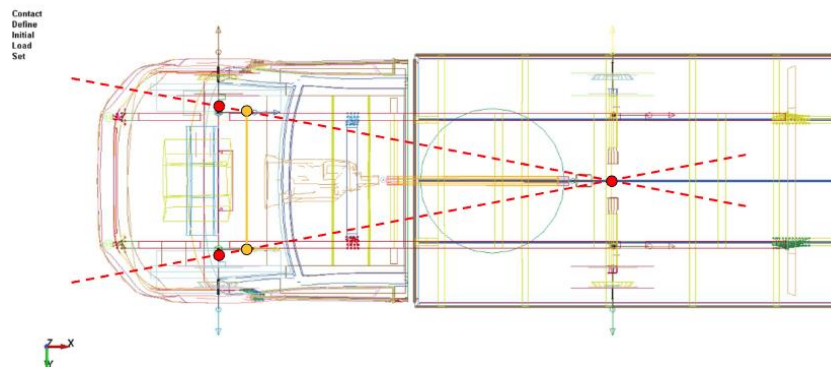


Figure 23 - N1 model Ackerman steering [12]

The degrees of freedom in the suspension are described with the help of kinematic joints in the following pictures:

- Front axle (figure 24). Part 1 is the mounting point of the suspension on the frame. Part 2 and 3 are parts that describe the independent suspension of the front axle. Part 4 is the wheel. The relations between these parts are:
 - Between 1 and 2: Translation (without rotation) in Z direction. Suspension.
 - Between 2 and 3: Rotation in Z direction. Yaw.
 - Between 3 and 4: Rotation in Y direction. Roll (wheel rotation).

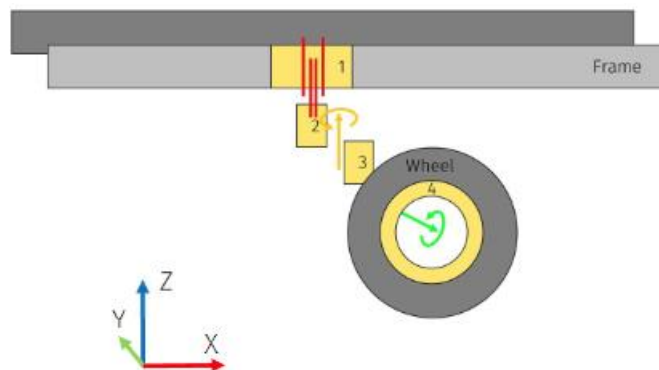


Figure 24 - Front axle degrees of freedom [12]

- Rear axle (figure 25). Part 1 is the mounting point of the suspension on the frame. Part 2 describe the dependent suspension of the rear axle, and it is comprised of rigid (because of the joints) and deformable parts. Part 3 is the wheel. The relations between these parts are:
 - Between 1 and 2: Translational joint in Z direction (without rotation). Suspension.

- Between 2 and 3: Rotation in Y direction. Roll (wheel rotation).

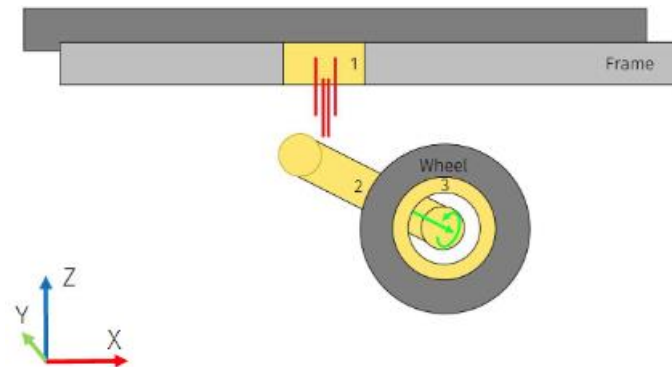


Figure 25 - Rear axle degrees of freedom [12]

4.3. Simulations

The contribution on the development of the vehicle model is to perform simulations on a preliminary version of the model on the following tasks assigned by SVS FEM:

1. Run the frontal impact of the model against the simple rigid wall that is present in the model, to verify that everything works fine. Evaluate data from accelerometers, energy balance, contact forces (vehicle - barrier).
2. Create a FE mesh of a bollard of 500 mm in diameter and use this mesh instead of the previous simulation wall mesh. Evaluate data from accelerometers, energy balance, contact forces (vehicle - barrier).
3. Run 3 variations of the crash to the bollard impact simulation. Change mass of the cargo in these cases (100kg, 500kg, 1000kg). Evaluate results of individual cases and summarize the effect of change in cargo mass on the results.

Computational resources were provided by HPC@POLITO, a project of Academic Computing within the Department of Control and Computer Engineering at the Politecnico di Torino (<http://hpc.polito.it>).

4.3.1. First task

The first simulation is performed to verify the correct operation of the model on an initial impact with a simple barrier (wall mesh), which is the model as received by SVS FEM (figure 26). The target is to identify any strange behaviour of the vehicle model on this simple impact. The simulations are performed with the R12.1 double precision MPP (Message Passing Parallel) version of the LS-Dyna, and the simulation successfully ran.

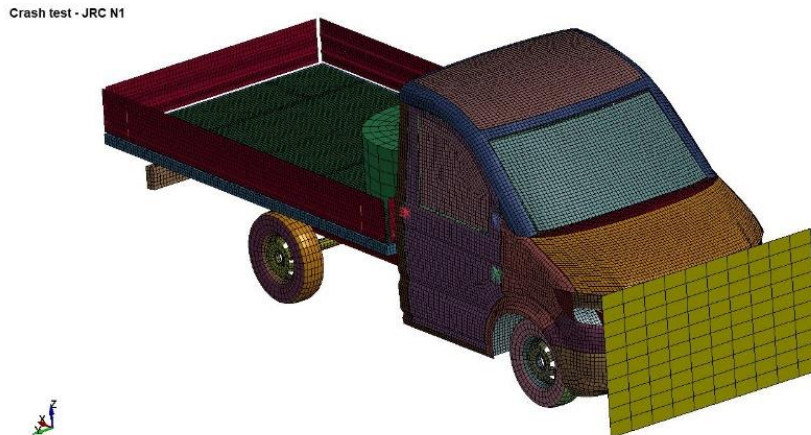


Figure 26 - Vehicle impact on simple barrier

An initial velocity of 48 km/h and cargo mass of 1000kg is used for this simulation. The animation of the simulation, as well as the output results, do not display any strange behaviour upon impact. From the energy balance

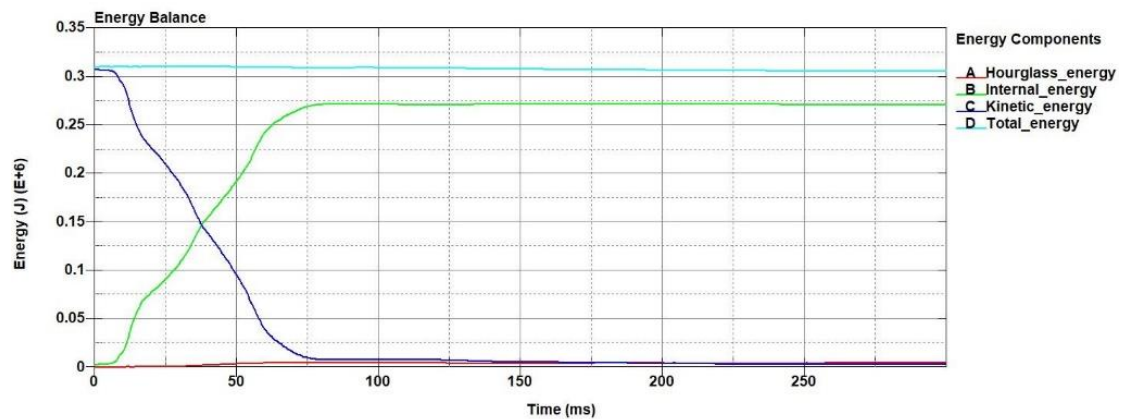


Figure 27 - Wall barrier impact energy balance

(figure 27), the total energy displays an insignificant change, and the hourglass energy increases slightly. The resultant acceleration (figure 28) of the vehicle and resultant contact force (figure 29) of the barrier-vehicle was obtained and filtered using the SAE filter with C/s of 60 Hz, which is a common filter used in the automotive sector for this application. By observing the

results, it is verified that the operation of the model upon an initial impact with a simple wall barrier is acceptable.

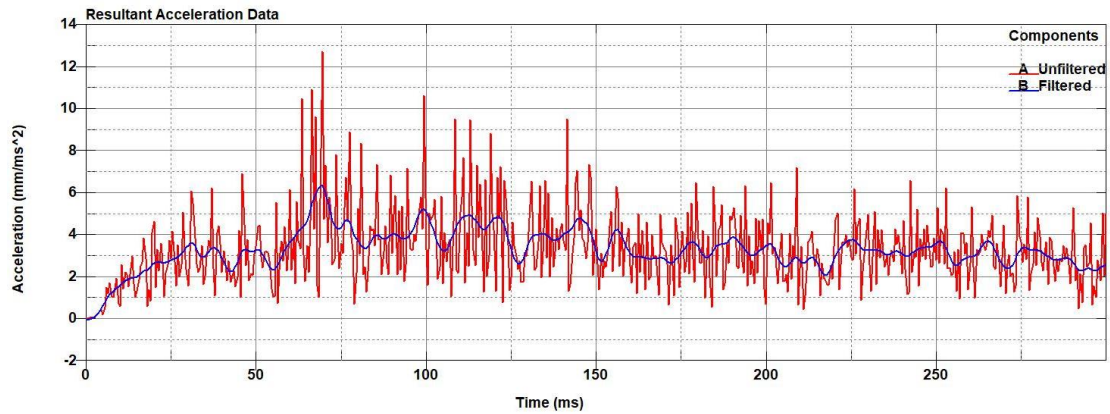


Figure 28 - Wall barrier impact resultant acceleration

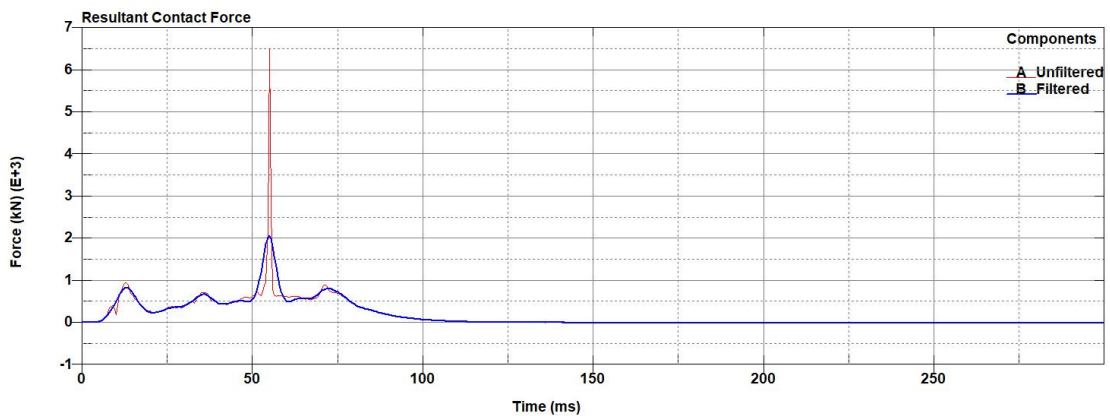


Figure 29 - Wall barrier impact resultant contact force

4.3.2. Second task

For the next task, a modification is performed to the simple wall barrier. A bollard of 500 mm diameter replaces the wall barrier (figure 30). An initial velocity of 48 km/h, as well as the same cargo mass of 1000 kg is

Crash test - JRC N1



Figure 30 - Vehicle impact on bollard

used. From the energy data (figure 31) an irregular behaviour of the energies is observed, more specifically, an increase of the internal and kinetic and a pronounced hourglass effect. The parts that affect the hourglass energy, are

displayed on figure 32. The parts that must be taken into consideration are the “Frame front bumper”, “Floor partition” and “Windshield” (figure 33). Upon closer examination on the part “Floor partition”, a penetration of the engine through it is observed from the animation. A part to be noted is the “Floor

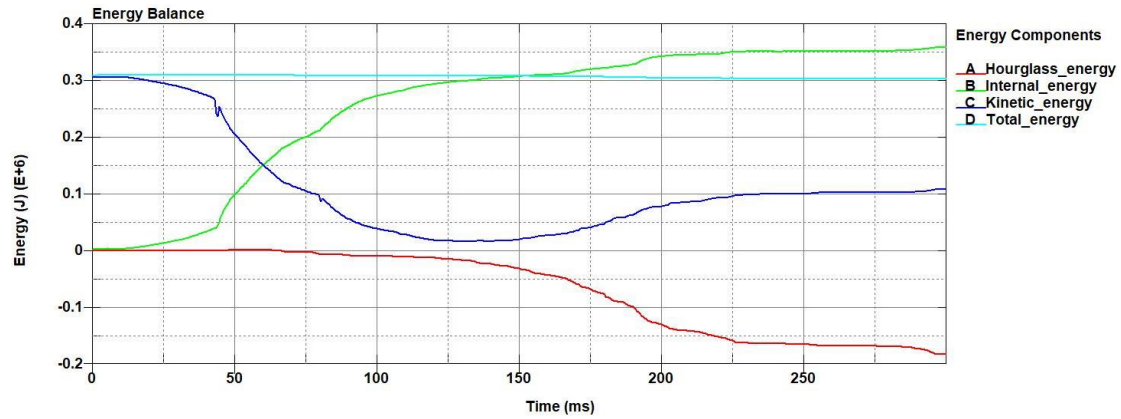


Figure 31 - Bollard impact (1000 kg cargo mass) energy balance

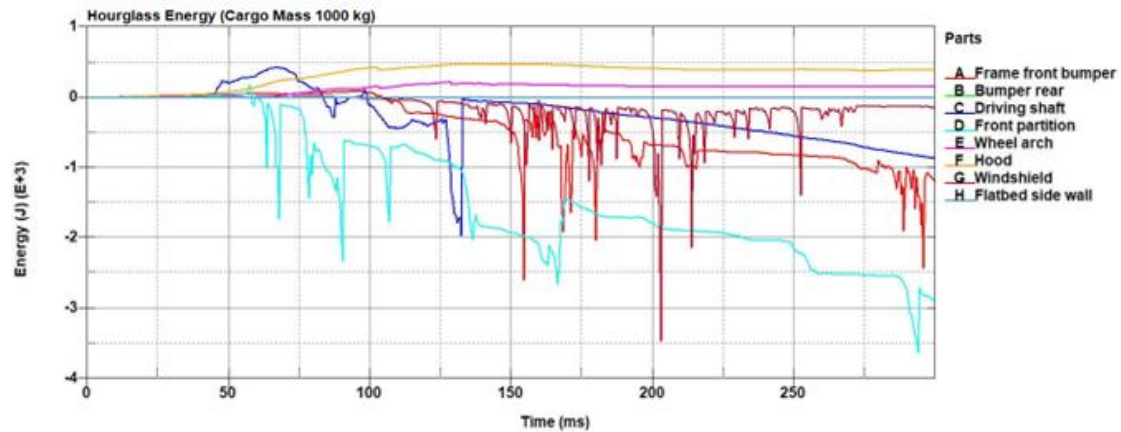


Figure 32 - Bollard impact (1000 kg cargo mass) parts with significant hourglass energy

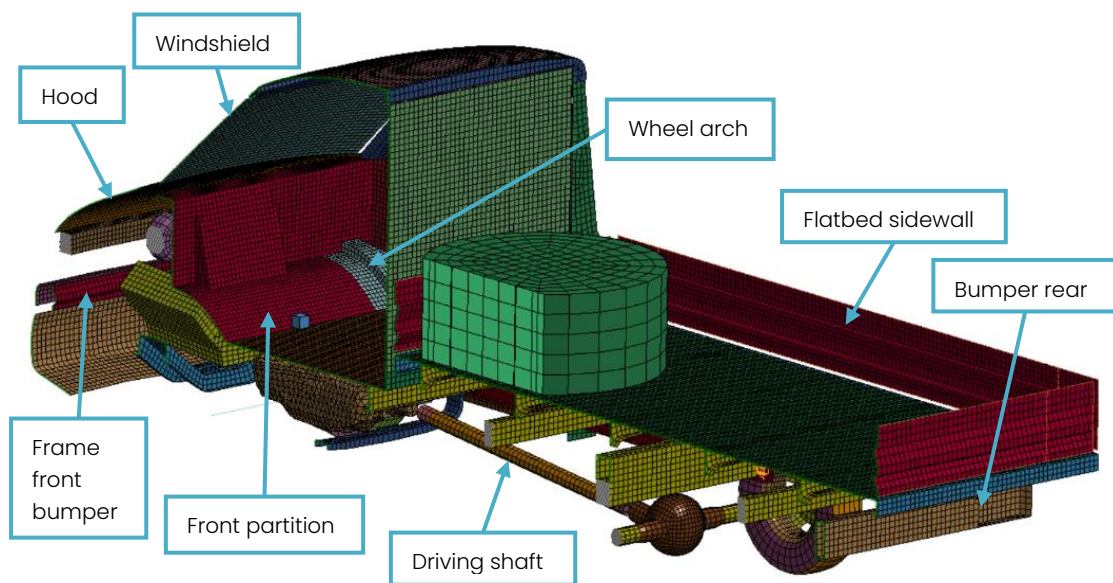


Figure 33- Parts with significant hourglass energy

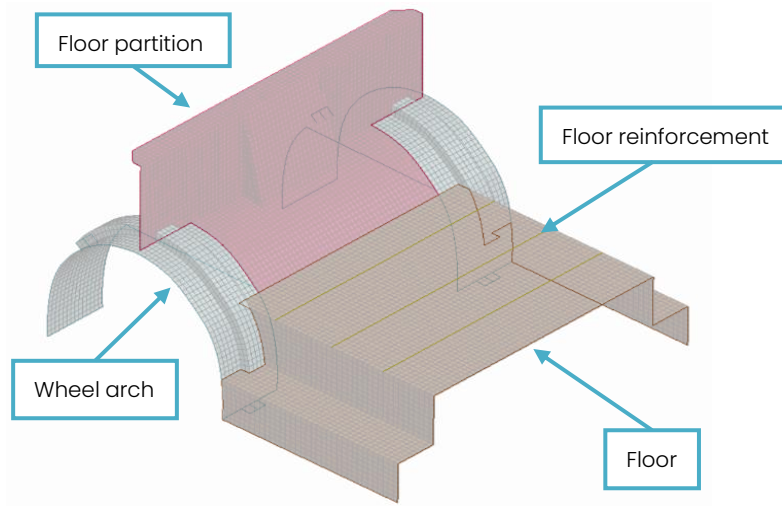


Figure 34 – Parts linked to "Floor partition"

reinforcement", which is an 1D element linked to the parts "Floor", "Front partition" and "Wheel arch" (figure 34). From the animation, comparing the case of the bollard (left) with the case of the simple wall (right), the penetration of the engine (figure 35) and the "explosion" of the part "Floor reinforcement" (figure 36) is not apparent on the simple wall barrier case. From the acceleration (figure 37) and contact force graphs (figure 38), the

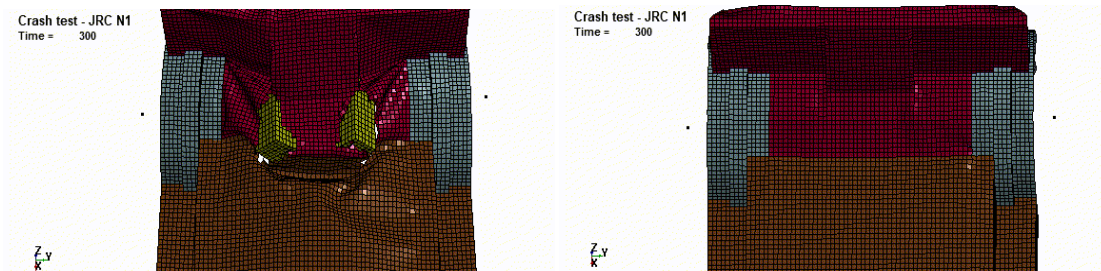


Figure 35 – Animation comparison of bollard impact (left) versus simple wall impact (right) on 1000 kg cargo mass

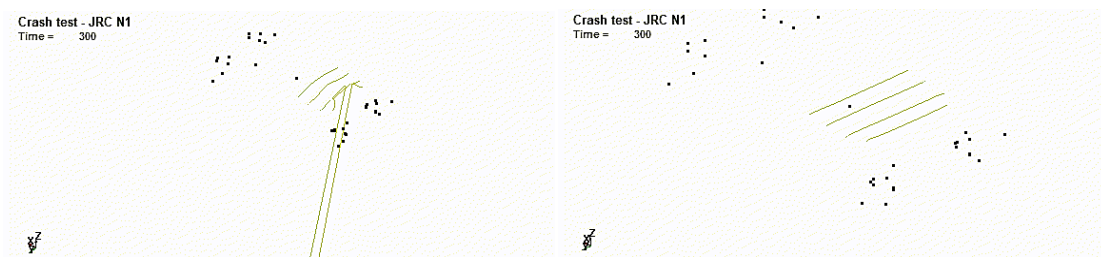


Figure 36 – Part "Floor reinforcement" behaviour on bollard impact (left) and simple wall impact (right) on 1000 kg cargo mass

results of the contact force are different compared to the simple wall case, where there is an initial force peak followed by some decreasing force peaks.

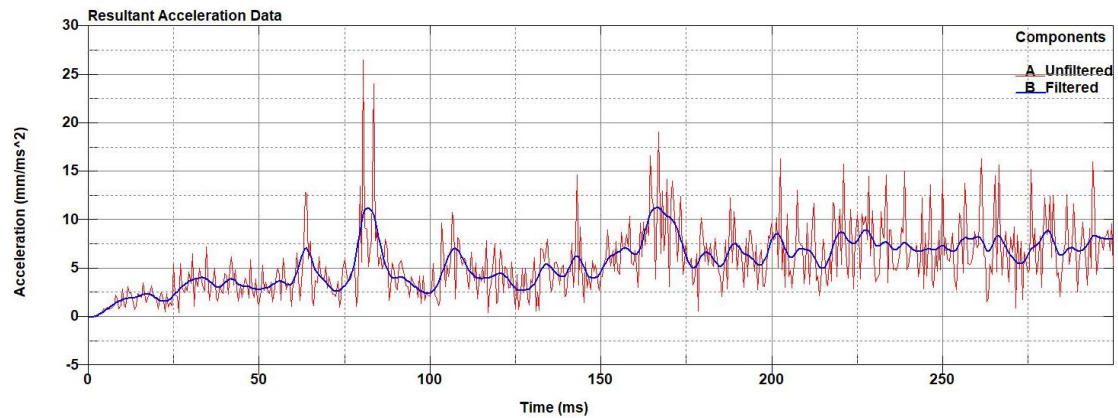


Figure 37 – Bollard impact (1000 kg cargo mass) resultant acceleration

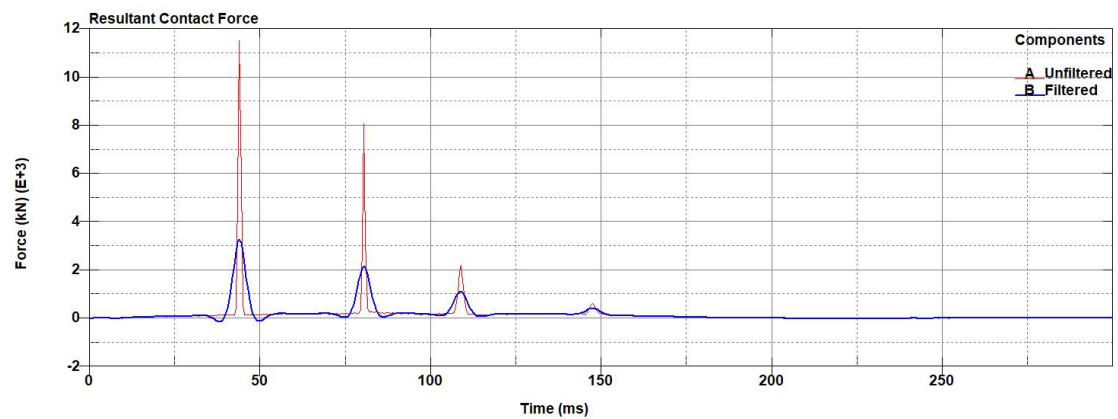


Figure 38 – Bollard impact (1000 kg cargo mass) resultant contact force

4.3.3. Third task

For the third task, the bollard barrier is maintained, and the cargo mass is changed via the file "PARAMETERS.k". An initial velocity of 48 km/h is used. The simulations in this case were performed only for the 100 kg and 500 kg case and are compared to the results from the previous case, since

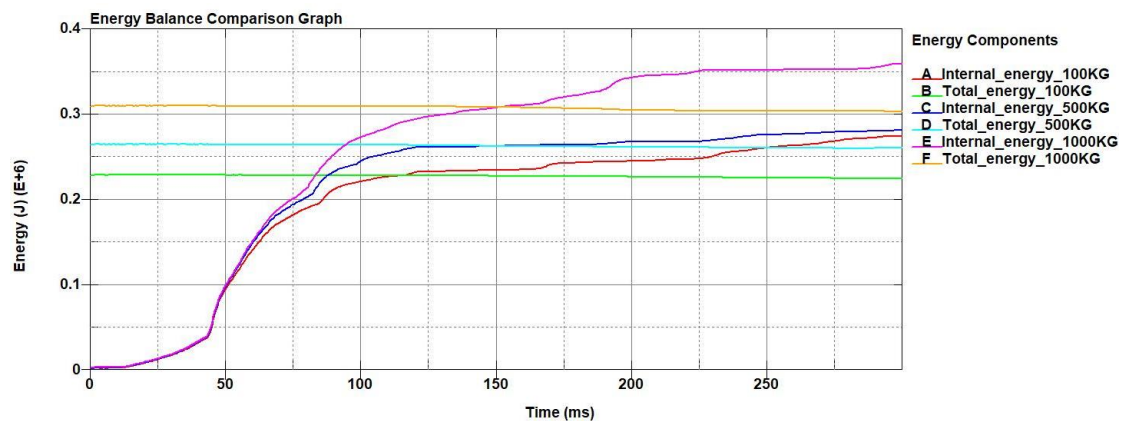


Figure 39 – Bollard impact (500 kg vs 100 kg) total and internal energy comparison

the cargo mass was 1000 kg. Comparing the energy results (figure 39) the total energy decreases as the cargo mass decreases. For higher cargo mass more energy is absorbed from the model. After a certain timeframe, the

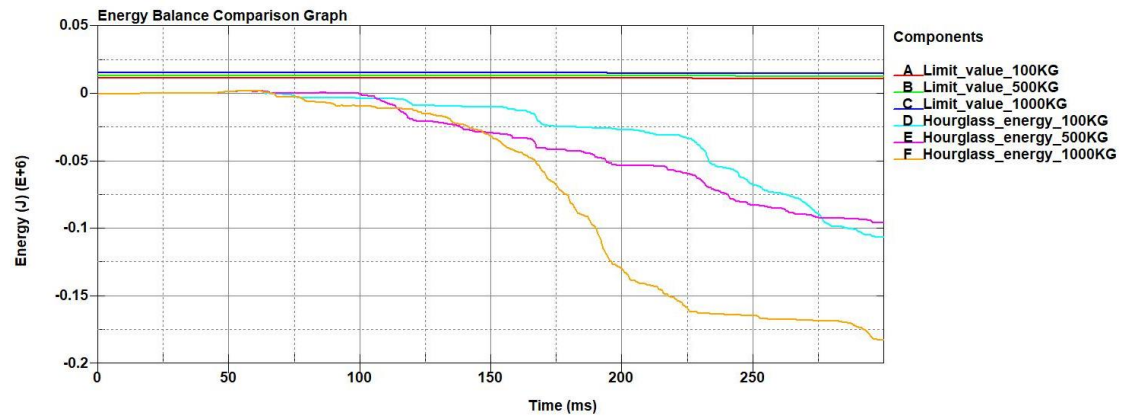


Figure 40 - Bollard impact (500 kg vs 100 kg) hourglass energy comparison with limit value of total energy of each cargo mass (5% of total energy)

internal energy surpasses the total energy. This is due to the hourglass phenomenon, which is more pronounced at the 1000 kg cargo mass and differs significantly compared to the other two cases (figure 40). Reducing the cargo mass ten times (100 kg), the hourglass energy has similar behaviour to the 500 kg case, even though the total vehicle mass has been

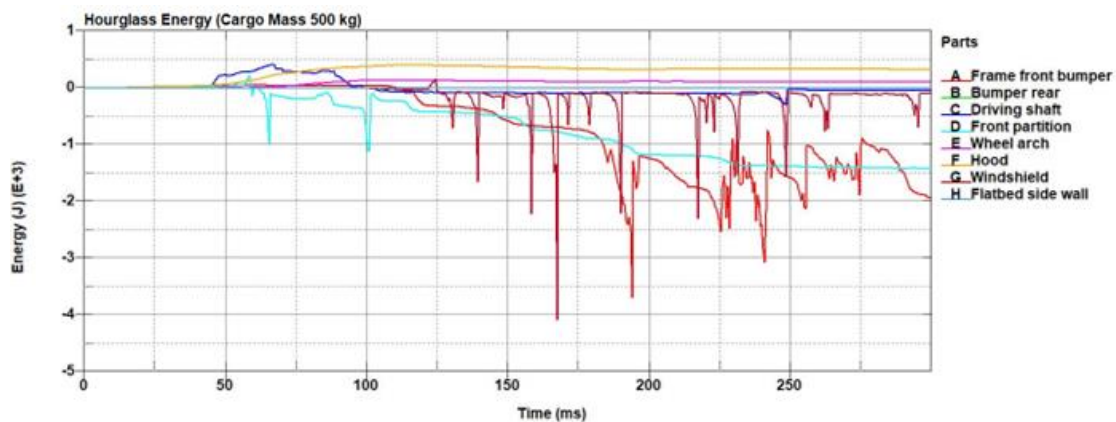


Figure 41 - Bollard impact (500 kg cargo mass) parts with significant hourglass energy

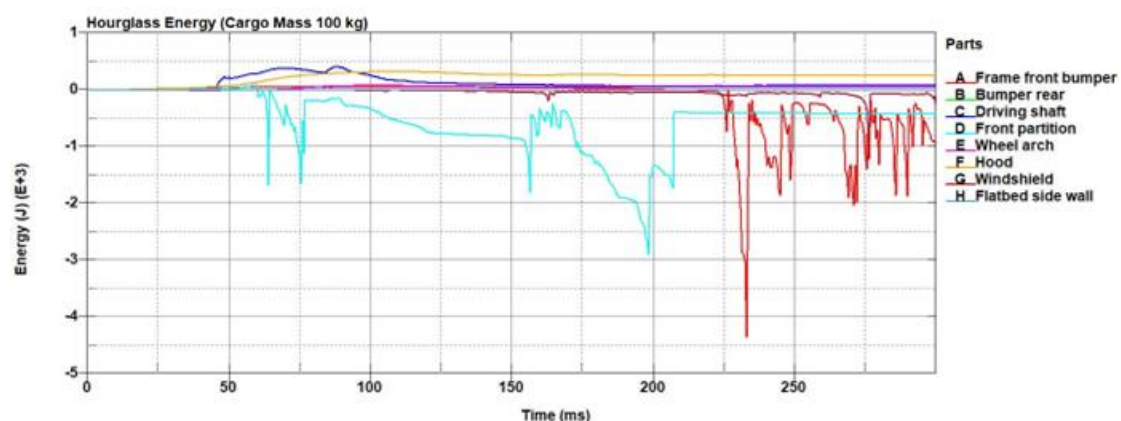


Figure 42 - Bollard impact (100 kg cargo mass) parts with significant hourglass energy

reduced. Comparing the figures of the hourglass energy by parts (figures 32,41,42) the hourglass energy of “Frame front bumper”, “Floor partition” and “Windshield” reduces as cargo mass decreases. However, there are some energy peaks which may affect the hourglass energy of the 500 kg and 100 kg case, hence why the hourglass energy of those two cases differ a little. Regarding the penetration of the engine to the “Front partition” (figure 43), it is observed that as the mass decreases, the penetration becomes less

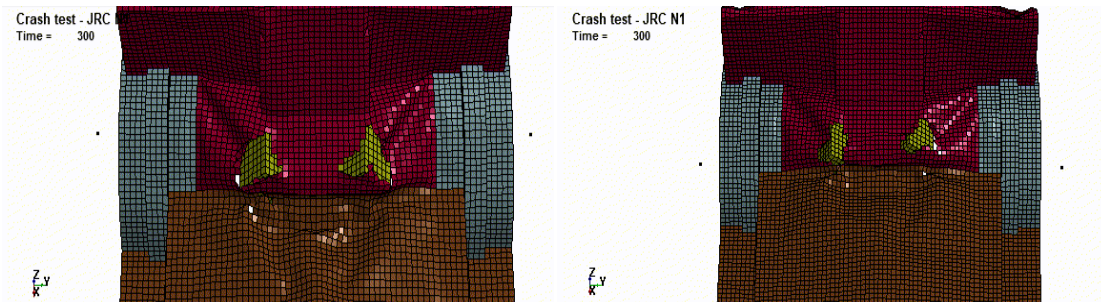


Figure 43 – Animation comparison on bollard impact of 500 kg (left) vs 100 kg (right) cargo mass

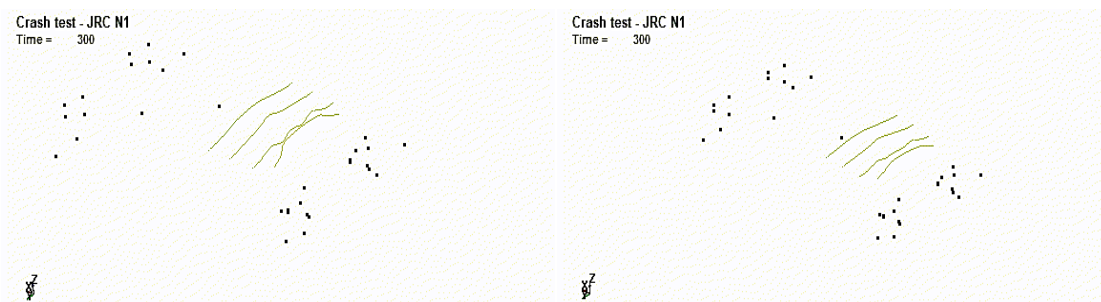


Figure 44 – Part “Floor reinforcement” behaviour on bollard impact of 500 kg (left) vs 100 kg (right) cargo mass

severe. Also, the “Floor reinforcement” part does not display the “explosive” behaviour of the 1000 kg case (figure 44). The resultant contact forces are compared for all three cases. The comparison is performed for the filtered and the unfiltered results (figure 45). As mass decreases, the first peak decreases and the following peaks are smaller. However, the filter applied to all the cases (SAE with C/s of 60 Hz) has made the initial peak almost identical for all three cases.

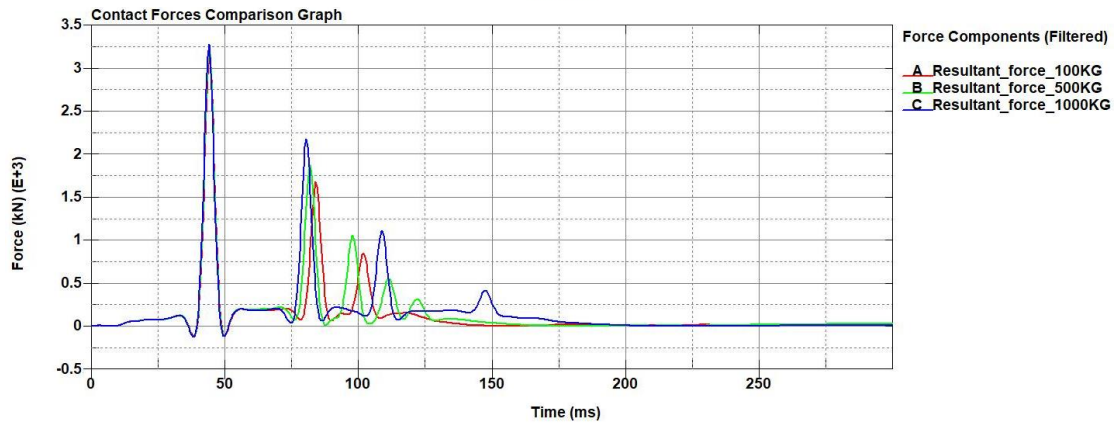
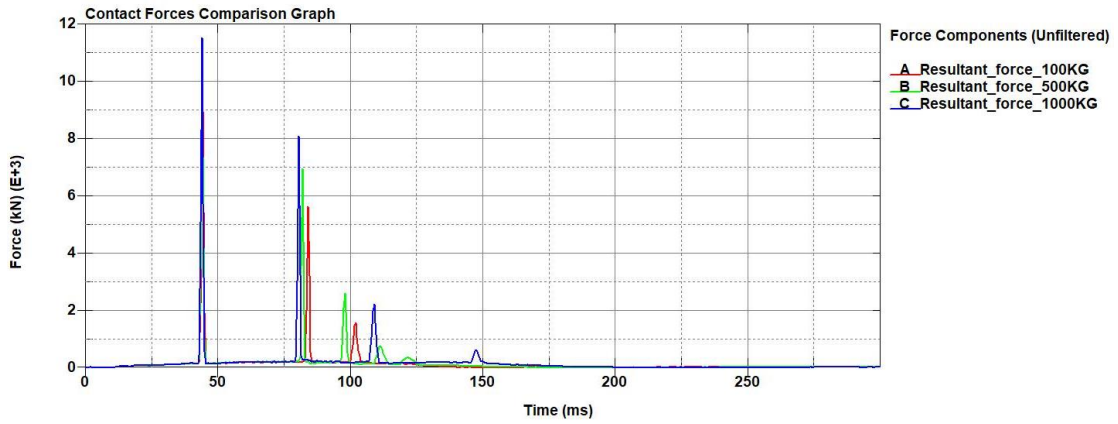


Figure 45 - Bollard impact resultant contact force for all cargo mass cases unfiltered (top) and filtered (bottom)

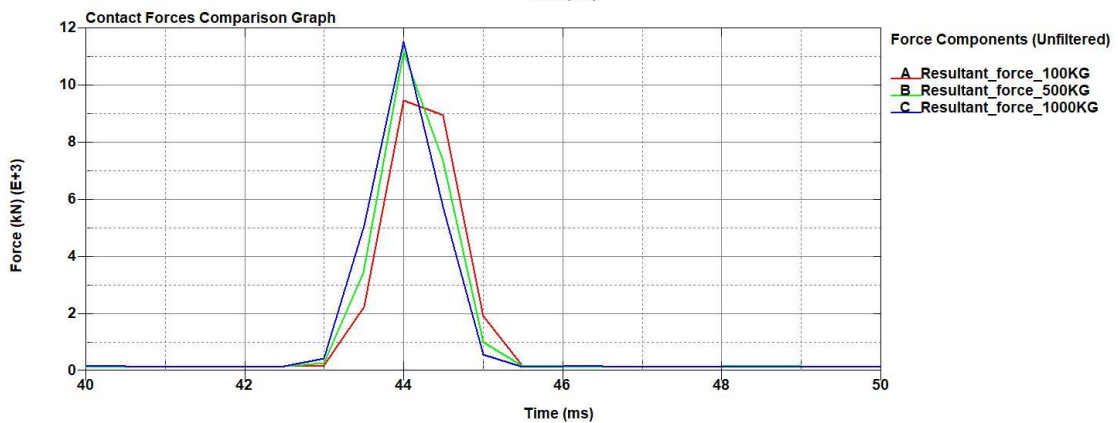
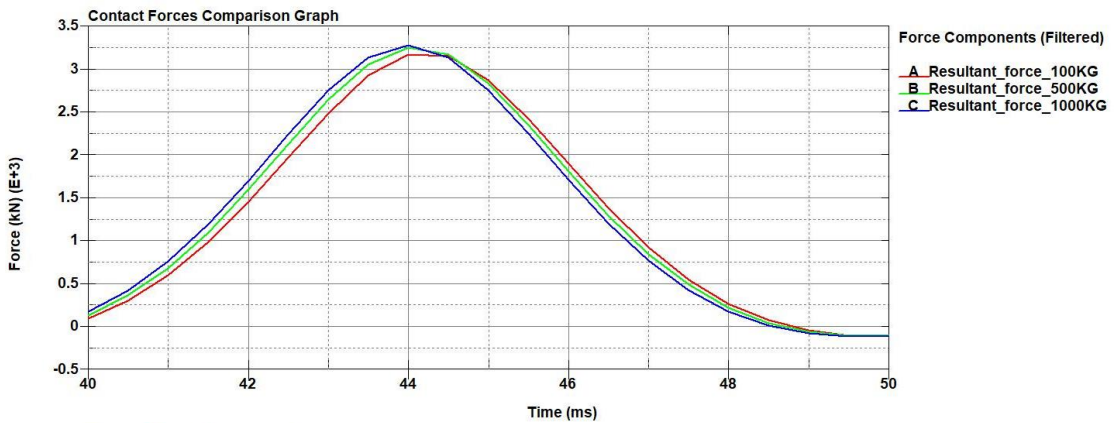


Figure 46 - Bollard impact resultant contact force for all cargo mass cases unfiltered (top) and filtered (bottom) detailed initial peak

Thus, the selected filter may not be suited for the proper extraction of the results of the contact forces (figure 46). Finally, for the resultant accelerations (figure 47), the behaviour is very similar for all cases. Only the filtered resultant acceleration is compared here since the acceleration is a signal with much noise. The 1000 kg case displays the highest peak of acceleration. The 500 kg case displays lower peaks than the 1000 kg cargo mass and for 100 kg cargo mass, the behaviour is similar to the 500 kg case. As it is clear so far, finding the proper filtering method to deduce the acceleration and contact force signal, imposes a challenge for the proper extraction of the results.

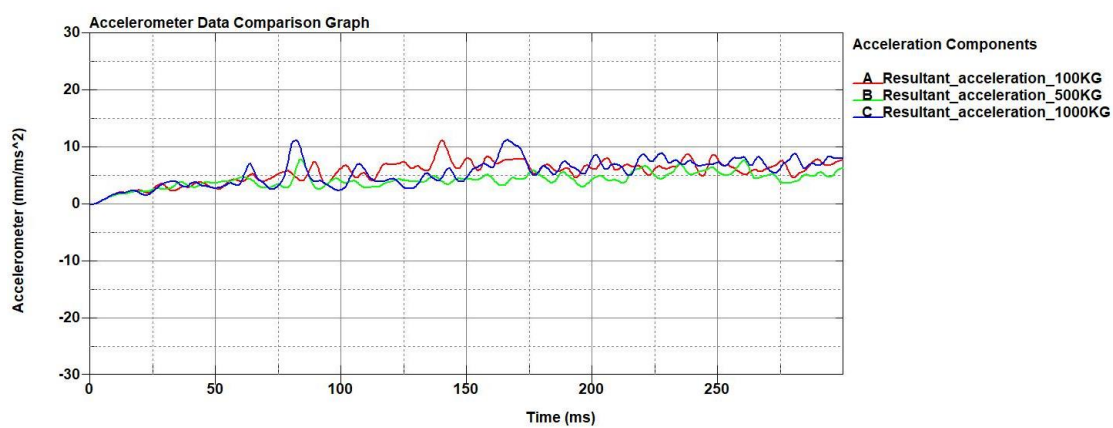


Figure 47 - Bollard impact for all cargo mass cases resultant acceleration

5. EPX Simulations

5.1. Scope of the simulations

The next part of the contribution of the Politecnico di Torino is to perform a comparison of the codes between two solvers:

- LS-Dyna, which is a well-established software for vehicle crash analyses (and is the solver used by SVS FEM to develop the NI vehicle model).
- Europlexus, which is a solver co-developed and used by the JRC.

The comparison will provide an insight into the physics of the model, distinguishing what is important or not during the impact of the model and estimate the “software effect”, in order to develop a model that its results are not affected by the software on which it is used. As in the preliminary model vehicle simulations, computational resources are provided by HPC@POLITO (<http://hpc.polito.it>).

5.2. Stages of code comparison

The simulations to be performed are frontal impacts of models on a rigid wall. The first step of the code comparison is to begin with a simple geometry and changing different parameters to check their influence. The given parts (or parts) and the barrier will be extracted from the NI Generic Vehicle Model. The examined parameters are split into the following categories:

- Sensitivity to different vehicle parameters:
 1. Geometry (complexity of the model geometry)
 2. Material
 3. Initial velocity
 4. Added mass
- Discretization:
 1. Reduced/fully integrated element formulations
 2. Quadrilateral (Q4) vs Triangular (T3) element type
 3. Mesh size

5.3. Cross Beam Part

For the first code comparisons, frontal impact simulations are performed on a part of the NI vehicle model, which is called “Front cross member” (figure 48). This part, which is part of the front structure of the vehicle, is a bended shaped rectangular tube with a thickness of 1 mm. The first step of any extraction of a part (or parts) from the complete NI model is to perform a cleanup of the unwanted keywords that are located in the file. After the cleanup is performed, the simulation is set up according to the

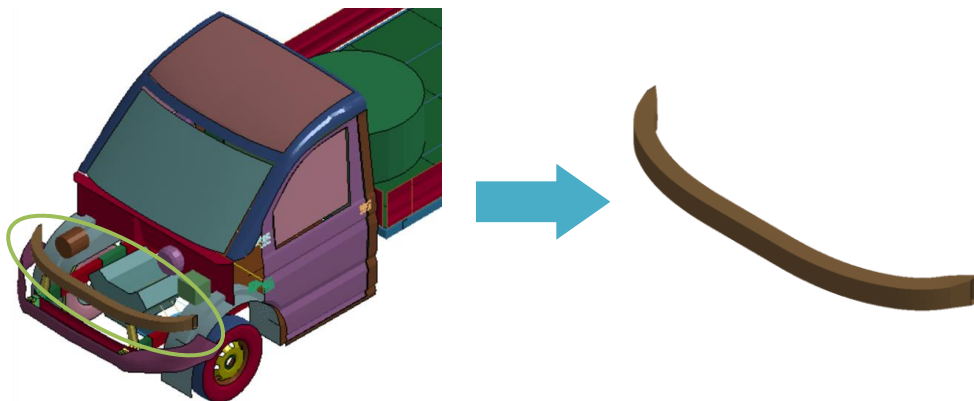


Figure 48 - Cross beam part extraction

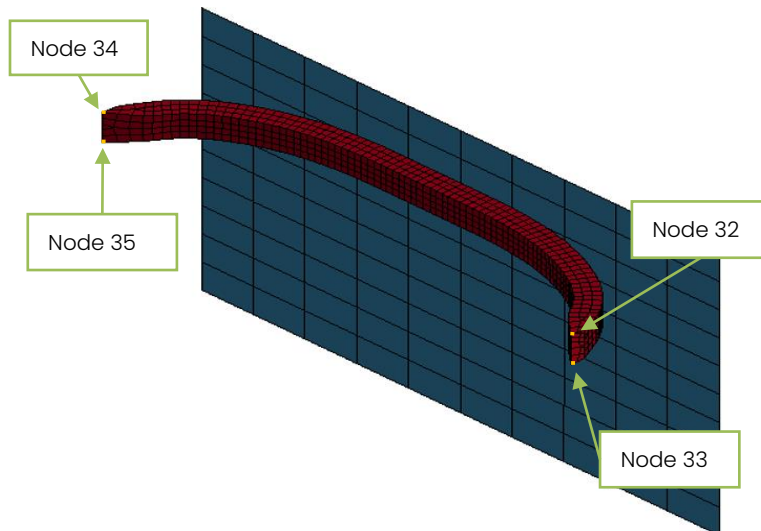


Figure 49 - Cross beam part with indicated nodes for measurements

required needs. Indicated nodes that are used for measuring acceleration, velocity and displacement is displayed on the figure 49. The solver used for these simulations is the R12 double precision SMP (Symmetric Multi-Processing) version of LS-Dyna.

5.3.1. Code comparison with elastic material

The first comparison is performed between the two solvers, assigning an elastic material to the “Front cross member” part. The keyword used in LS-Dyna for this material is 001-ELASTIC. The material parameters are:

- Density: 7800 kg/m³
- Young modulus: 210 GPa
- Poisson coefficient: 0.28

The contact model used for this simulation is the AUTOMATIC_SURFACE_TO_SURFACE, with no friction assigned to it, following the computations with the Europlexus solver. The shell element formulation is preserved from the NI model, which is the EL. FORM 2 (Belytschko-Tsay). Since EL. FORM 2 is a type of reduced integration element, in order to control the rise of hourglass energy, the keyword HOURGLASS is used as in the NI vehicle model, with the same parameters as in the model, and the Flanagan-Belytschko stiffness form (EQ.4) hourglass control type selected. The element types are going to be analyzed in a next chapter, where a comparison between different element types is performed. Initial velocity is 10 m/s. From the energy balance graph (figure 50), it is observed that the behaviour of the internal

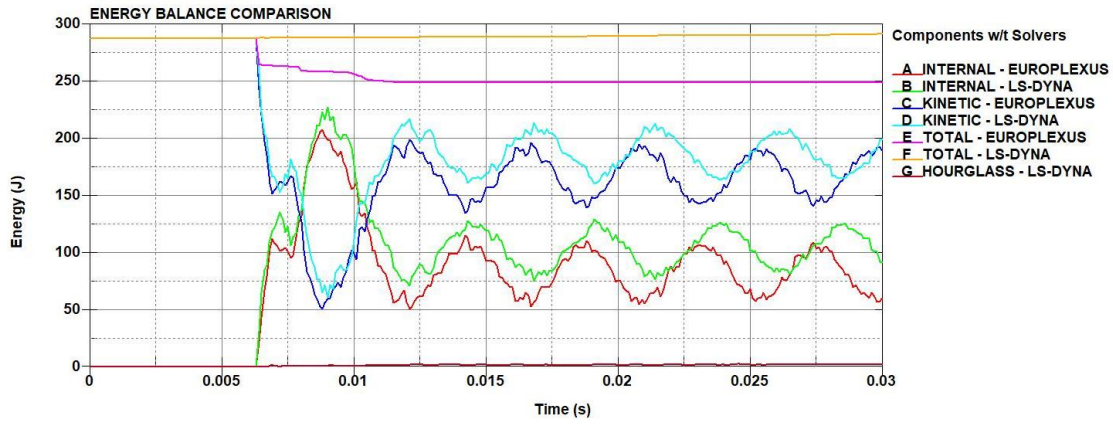


Figure 50 - Cross beam elastic material energy balance

and kinetic energies is similar. However, there is a dissipation of energy on the Europlexus solver due to its contact model, while LS-Dyna preserves that energy upon impact. Europlexus uses a Lagrange multiplier method model, while LS-Dyna uses a penalty method model [5, 7, 9]. Additionally, the main response frequency of the oscillation of the model upon impact, in the Europlexus solver is a little higher than the LS-Dyna solver, indicating a slightly “stiffer” model. This is due to the fully integrated elements used by

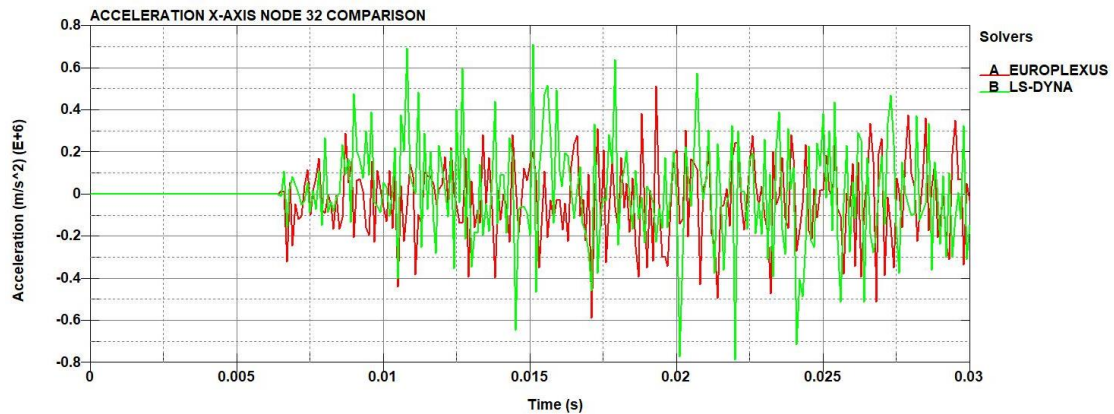


Figure 51 - Cross beam elastic material node 32 x-axis acceleration

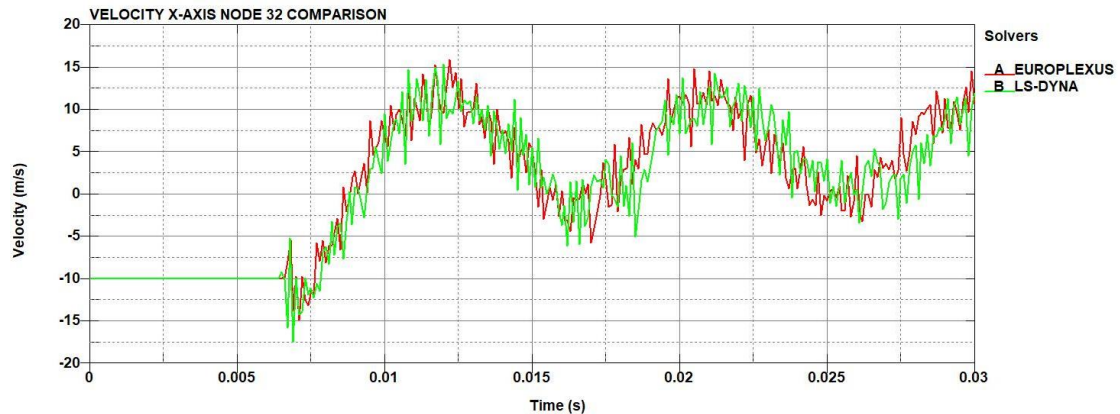


Figure 52 - Cross beam elastic material node 32 x-axis velocity

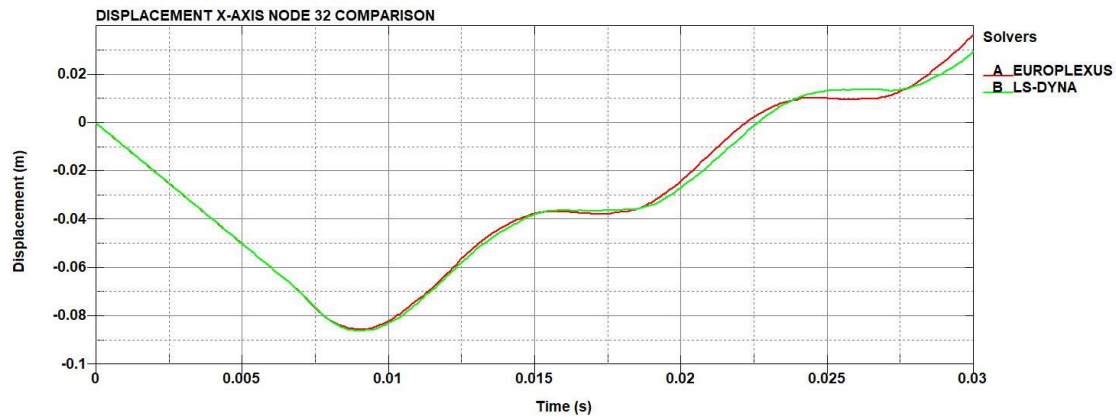


Figure 53 - Cross beam elastic material node 32 x-axis displacement

the Europlexus solver, while elements with reduced integration are used in the LS-Dyna simulation. The acceleration (figure 51) and velocity (figure 52) signals contain a large amount of frequency noise. However, the trend of the velocity signal can be easily distinguished. Regarding the displacement of node 32 (figure 53), the behaviour is very similar between the two solvers, thus the overall behaviour of the part is similar in this comparison between both solvers.

5.3.2. Code comparison with different element formulations on elastic material

Maintaining the elastic material, parameters and solver of the previous simulation, the next objective is to compare different element formulations for the shell element. The types of element formulations to be tested are:

- EL. FORM 2: Belytschko-Tsay
- EL. FORM 8: Belytschko-Leviathan
- EL. FORM 10: Belytschko-Wong Chang
- EL. FORM 16: Fully integrated shell element

The element formulations 2, 8 and 10 are element types of reduced integration. These element formulations are based on the Reissner-Mindlin shell theory. EL. FORM 2 is a simplified implementation of the Reissner-Mindlin theory and one of the fastest options. Reissner-Mindlin finite elements are subjected to “shear locking”, so Belytschko-Tsay uses a penalty approach to go around the shear locking effect. Contrary to the element formulations used in Europlexus (Q4 γ and T3 γ) which are more consistent by having no dependence on penalty parameters but have slower computational time.

Belytschko-Wong-Chang and Belytschko-Leviathan are the improvements of the initial Belytschko-Tsay element formulation. Finally, the EL FORM 16 is a fully integrated shell element, which is the one used for this simulation of Europlexus. Hourglass control is used for the reduced integrated elements as in the previous simulation. From the total energy (figure 54) a small rise of the total energy after 15 ms is observed, due to the increase of hourglass energy (figure 55) from the elements with reduced integration. From the

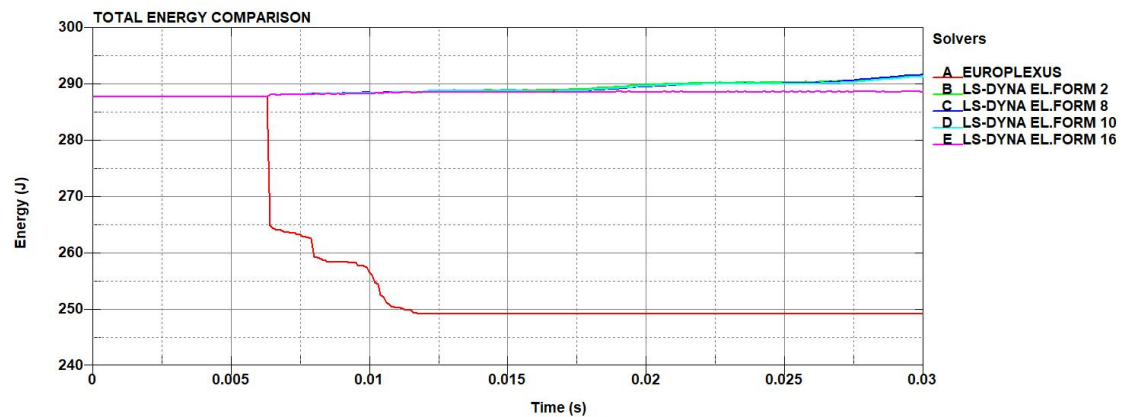


Figure 54 - Cross beam element formulation comparison total energy

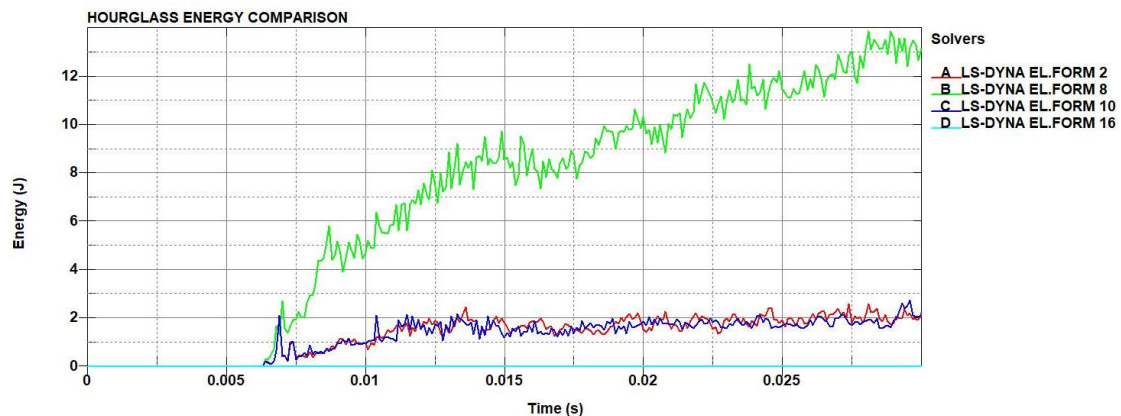


Figure 55 - Cross beam element formulation comparison hourglass energy

internal energy (figure 56), a difference in the dominant oscillation period of about 5 ms between the reduced integrated element formulations (2,8,10) and the fully integrated element formulations (16 and EPX). Thus, the reduced integration decreases the stiffness of the structure so that the oscillation frequencies are lower, corresponding to higher oscillation periods. However, this effect is small and becomes important only after several oscillation periods, without having a difference at the time of the main peak where the part interacts with the barrier. From the displacement graph of the node 32 (figure 57) the fully integrated element approaches very close the results from Europlexus. From this comparison it can be concluded that the main

difference (which is not significant) of the results between LS-Dyna and Europlexus comes from the contact model.

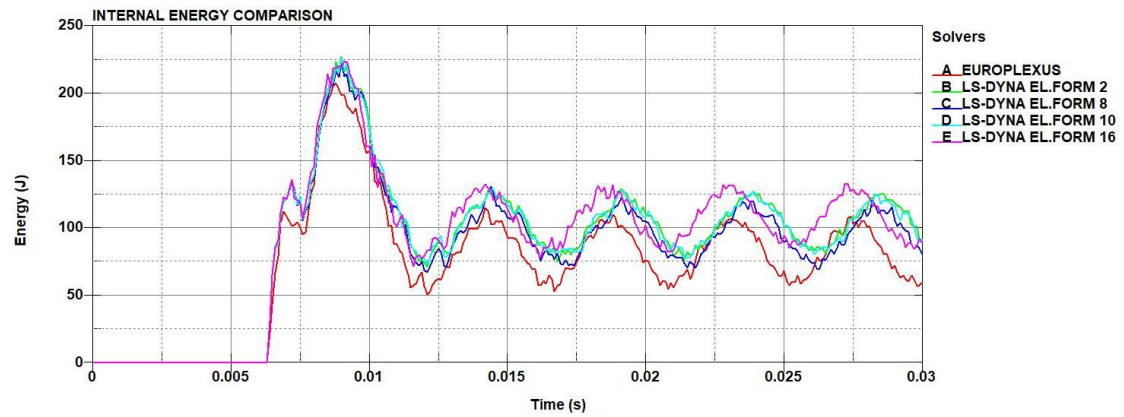


Figure 56 - Cross beam element formulation comparison internal energy

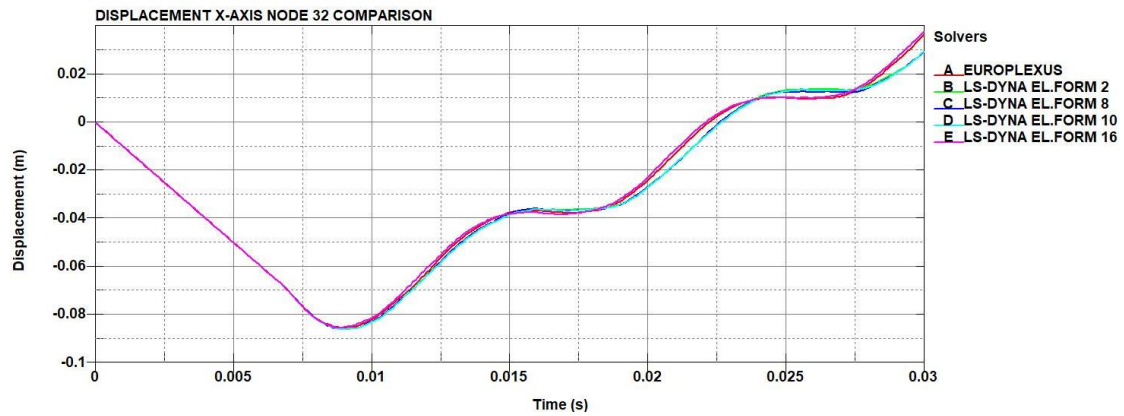


Figure 57 - Cross beam element formulation comparison node 32 displacement

5.3.3. Code comparison with elastoplastic material (perfect plasticity law)

For the next comparison, the pure elastic material is replaced with an elastoplastic material. In this case, the plastic behaviour after the elastic region is assumed as perfect plasticity (constant stress after the yield stress value) (figure 58). In the LS-Dyna software the material card used is 003-PLASTIC_KINEMATIC. The material parameters are:

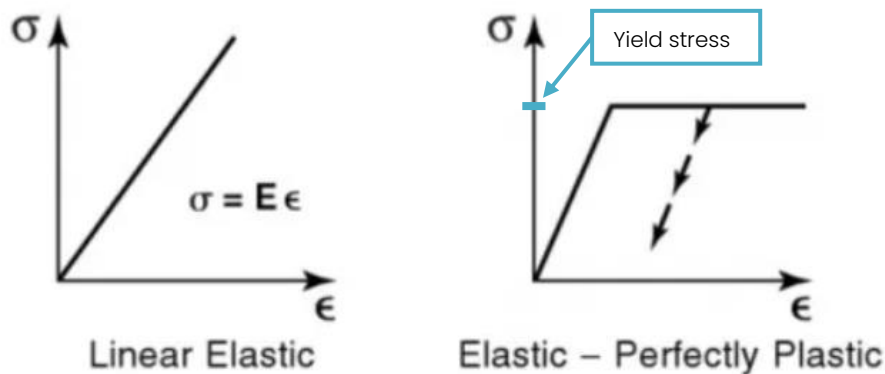


Figure 58 – Stress-strain curves of elastic material (left) and elastoplastic with perfect plasticity (right) [26]

- Density: 7800 kg/m³
- Young modulus: 210 GPa
- Poisson coefficient: 0.28
- Yield Stress: 350 MPa

For this comparison, two initial velocities are compared (10 and 20 m/s), as well as two different element types (EL. FORM 2 with the same hourglass control as in previous cases and EL. FORM 16 without hourglass control). For the contact model in LS-Dyna, the AUTOMATIC_SINGLE_SURFACE keyword is added to simulate the self-contact of the part. As previously, zero friction is

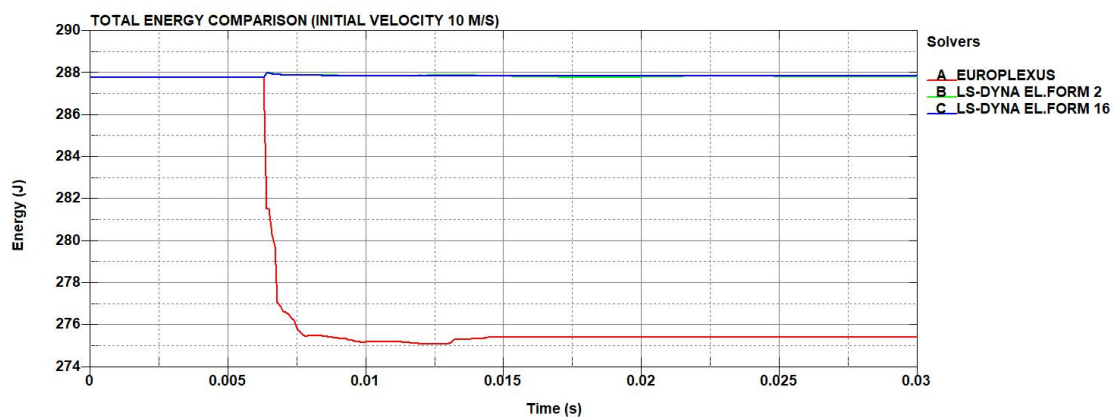


Figure 59 – Cross beam with elastoplastic material (perfect plasticity) (@10 m/s) total energy

assigned to the contact models as for the Europlexus simulations. On the 10 m/s case, there is a dissipation of energy from the Europlexus solver (figure 59), as well as a difference in the dominant oscillation period between the two element formulations, with the fully integrated element being similar to the Europlexus results (figure 60). The hourglass energy (figure 61) for the reduced integrated element formulation remains below the limit value (which is 5% of the total energy). Comparing the results of the displacement of the node 32 (figure 62) there is a visible difference in the displacement

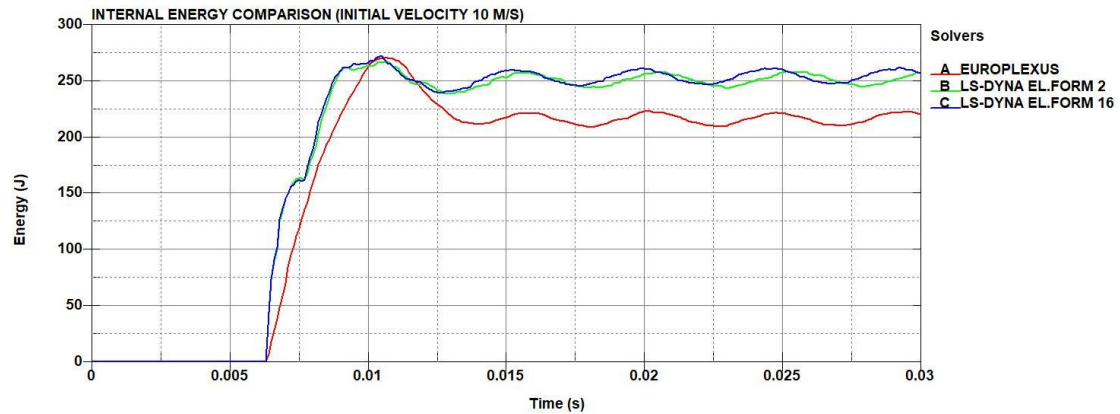


Figure 60 - Cross beam with elastoplastic material (perfect plasticity) (@10 m/s) internal energy

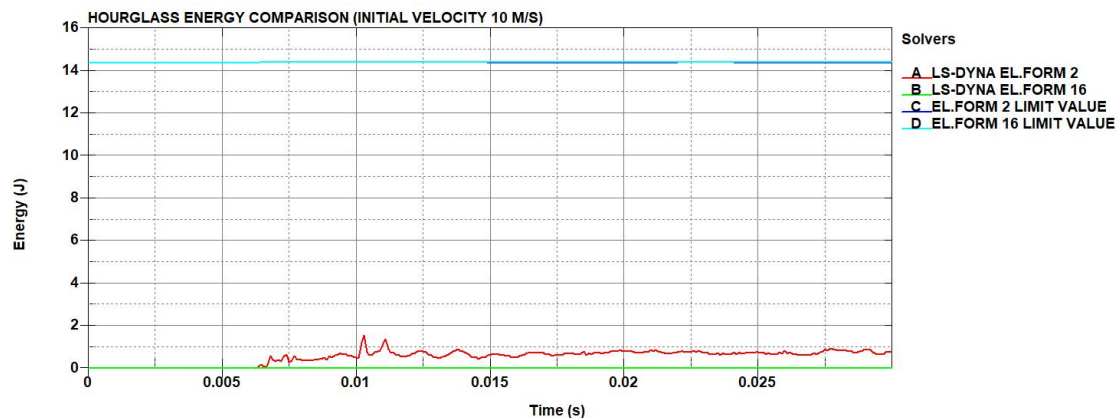


Figure 61 - Cross beam with elastoplastic material (perfect plasticity) (@10 m/s) hourglass energy with the corresponding limit values (5% of total energy)

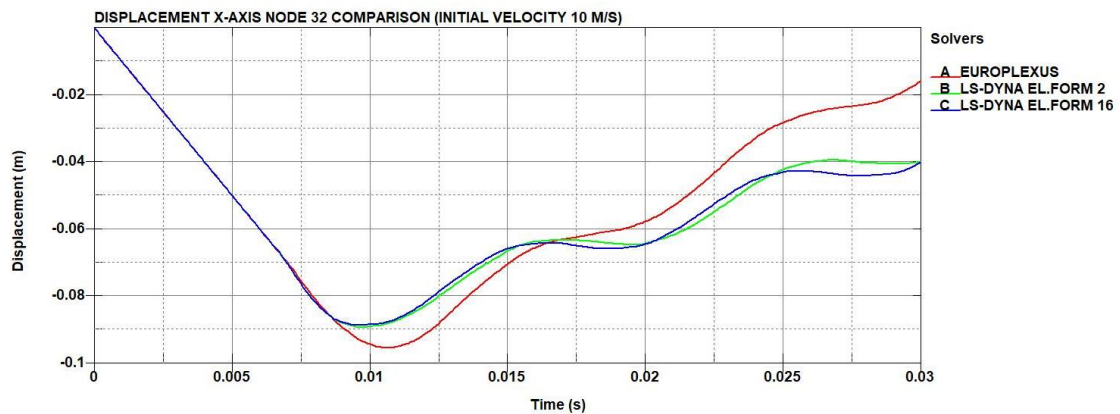


Figure 62 - Cross beam with elastoplastic material (perfect plasticity) (@10 m/s) node 32 x-axis displacement

between EPX and LS-Dyna. For the 20 m/s case the dissipation of energy from the Europlexus solver (figure 63) and the difference in the dominant oscillation period between the two element formulations (figure 64) also exist. However, the results from LS-Dyna are closer to the Europlexus results, compared to the 10 m/s case. The hourglass energy (figure 65) is also well below the limit value for both element formulations.

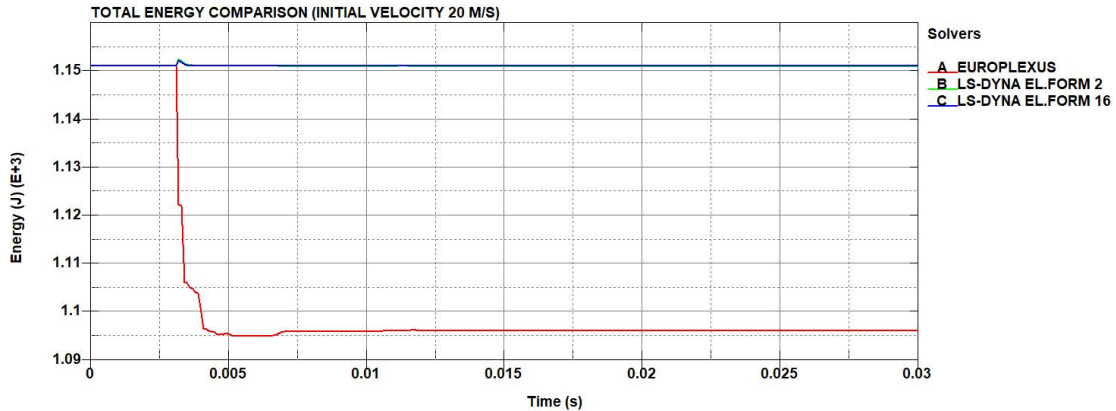


Figure 63 - Cross beam with elastoplastic material (perfect plasticity) (@20 m/s) total energy

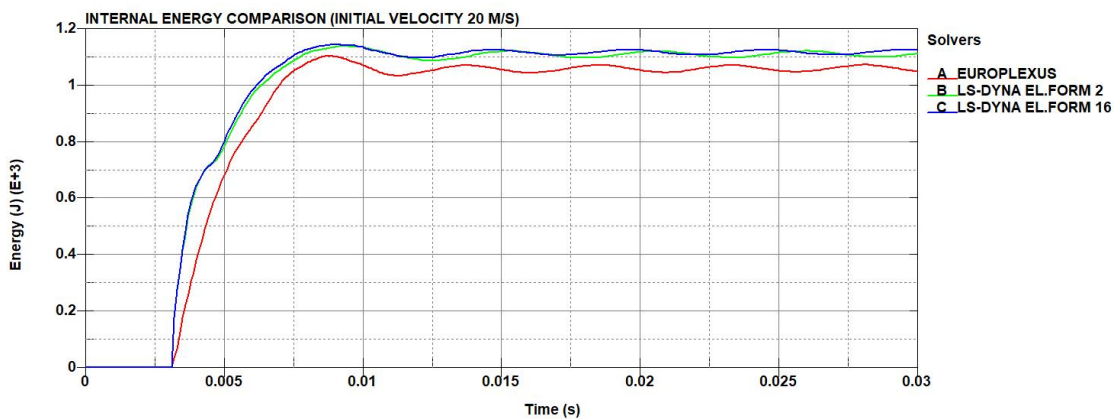


Figure 64 - Cross beam with elastoplastic material (perfect plasticity) (@20 m/s) internal energy

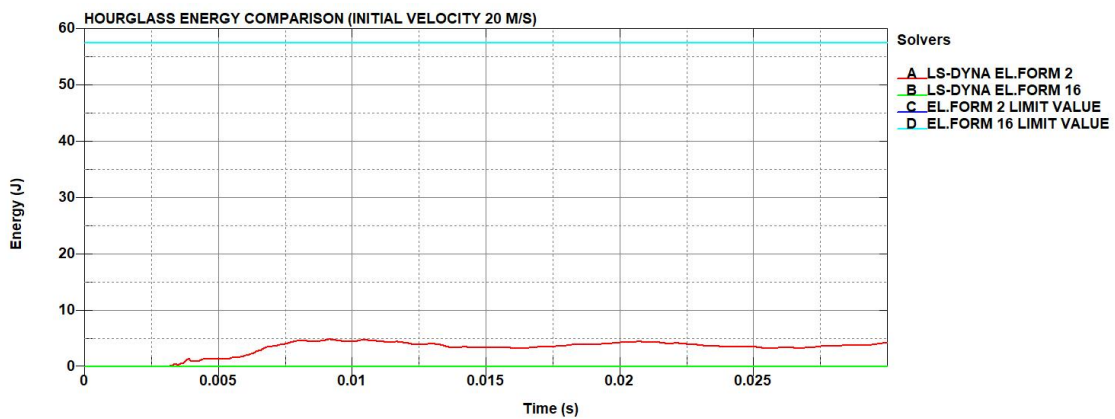


Figure 65 - Cross beam with elastoplastic material (perfect plasticity) (@20 m/s) hourglass energy with the corresponding limit values (5% of total energy)

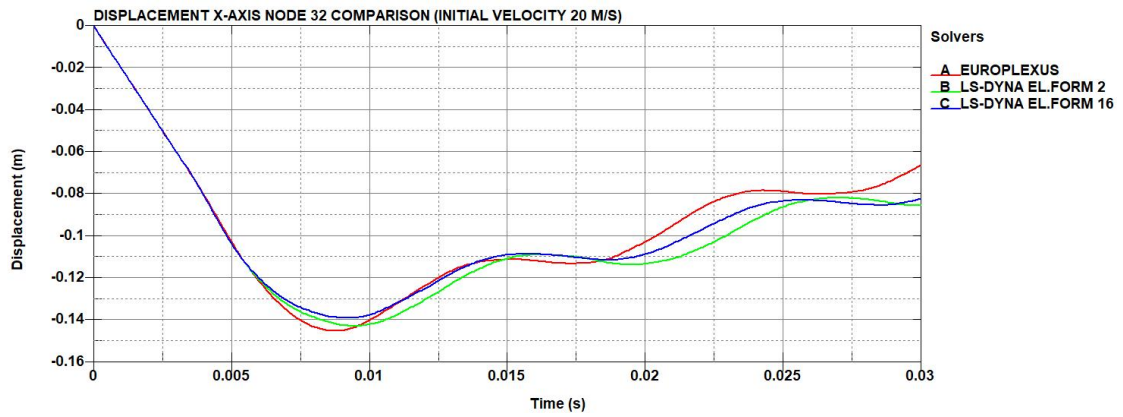


Figure 66 - Cross beam with elastoplastic material (perfect plasticity) (@20 m/s) node 32 x-axis displacement

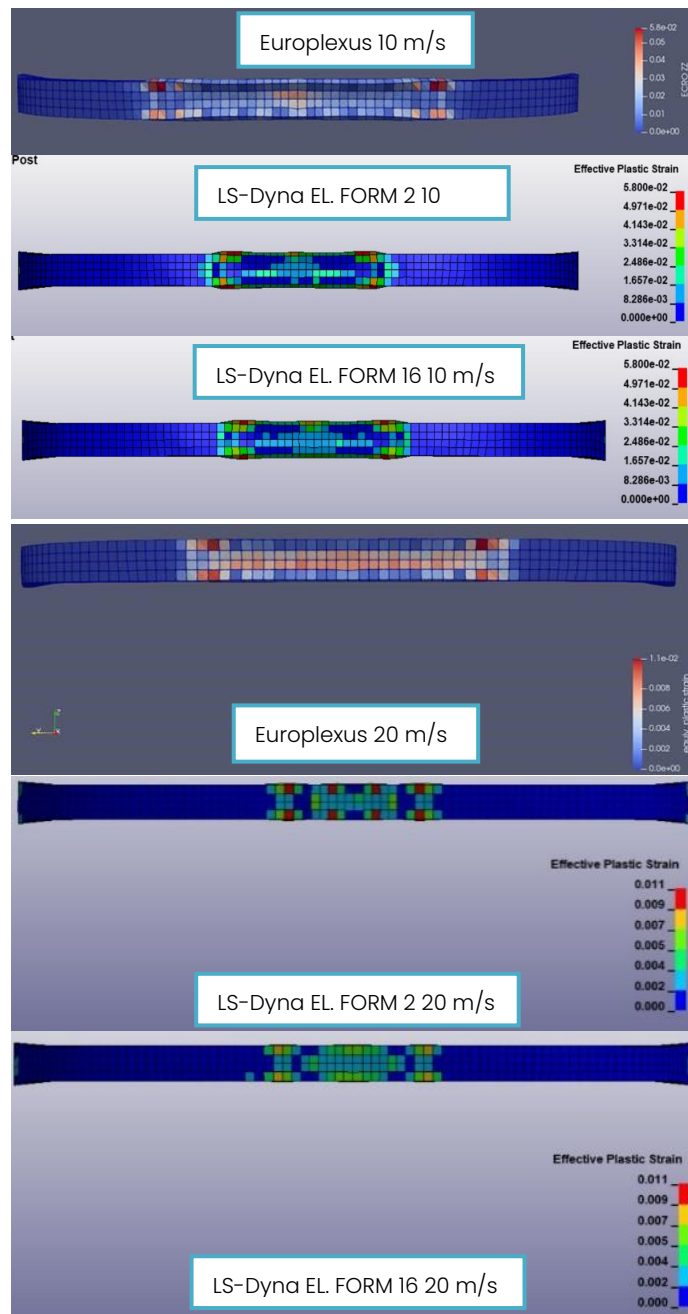


Figure 67 - Cross beam with elastoplastic material (perfect plasticity) effective plastic strain at 10 m/s and 20 m/s

The displacement of node 32 (figure 66) results from LS-Dyna are also closer to the results from Europlexus at 20 m/s. Comparing the effective plastic strain between the two solvers for both initial velocities (figure 67), it is clear that Europlexus gives a much larger plastified zone than LS-Dyna. It is also worth mentioning that comparing the residual kinetic energy (figure 68) and velocity (figure 69) from both solvers, the maximum elastic energy does not depend on the initial velocity, for this range of impact velocities. Concluding this comparison, the major differences between the two solvers in terms of energy balance and plastification is due to the different contact algorithms. These differences are not significant for the highest initial velocity (20 m/s) than in the less severe impact (10m/s), so they can be considered acceptable. Thus, for the cases of impact with high deformation, which is of main interest, the two solvers give equivalent results.

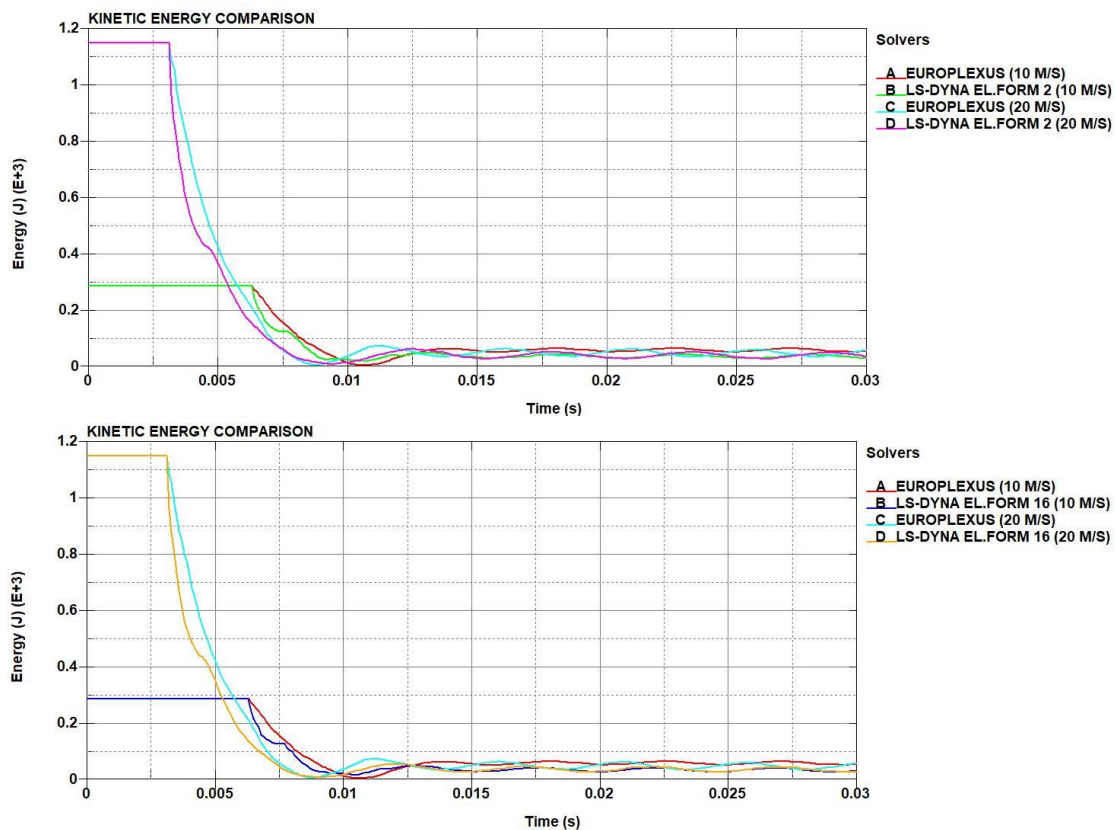


Figure 68 - Cross beam with elastoplastic material (perfect plasticity) residual kinetic energy of EL.FORM 2 (top) and EL.FORM 16 (bottom)

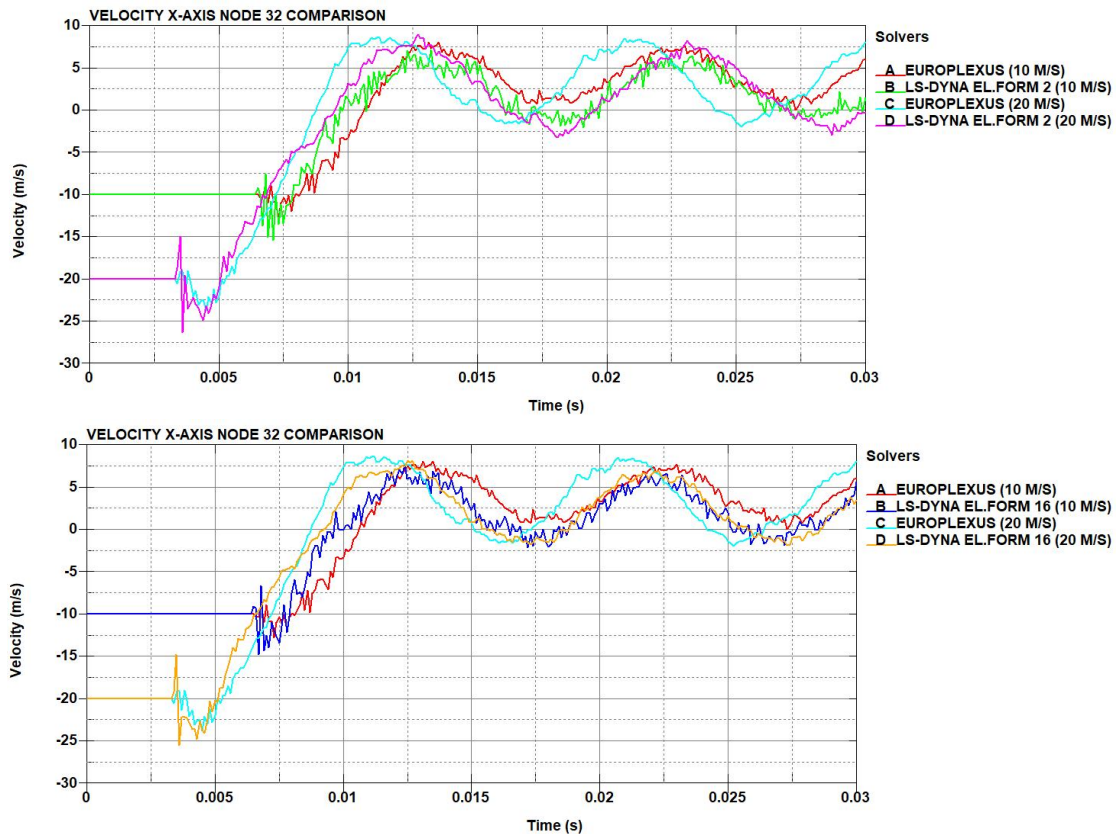


Figure 69 - Cross beam with elastoplastic material (perfect plasticity) node 32 x-axis velocity of EL. FORM 2 (top) and EL. FORM 16 (bottom)

5.3.4. Code comparison with elastoplastic material (perfect plasticity law) with added mass

Additional simulations are performed for the elastoplastic material, but with the addition of punctual masses at each end of the cross beam to check differences between the two element formulations when mass is added on the model. The masses are applied in the center of a constrained nodal rigid body (CNRB) assigned at each end of the part (figure 70). Two mass values will be tested at two different velocities:

- 10 kg mass at each end at 10 m/s
- 20 kg mass at each end at 20 m/s

For each case a comparison between EL. FORM 2 and EL. FORM 16 is performed. For this task, only the results from the LS-Dyna are presented. In

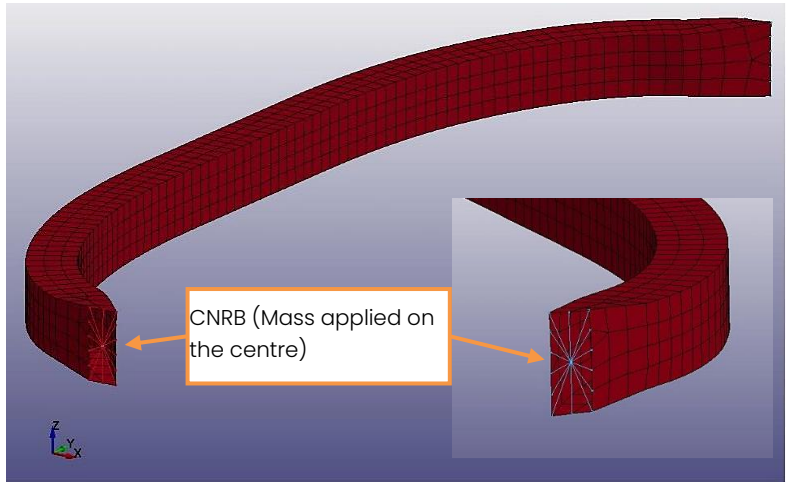


Figure 70 - Punctual mass position

the energy balance of the first case (10 kg, 10 m/s) (figure 71), the EL. FORM 16 absorbs more energy than the EL. FORM 2. The displacement of node 32 (figure 72), displays no significant difference between the two formulations. The effective plastic strain (figure 73) displays a higher maximum value for the fully integrated element formulation (0.07 for the reduced intergration

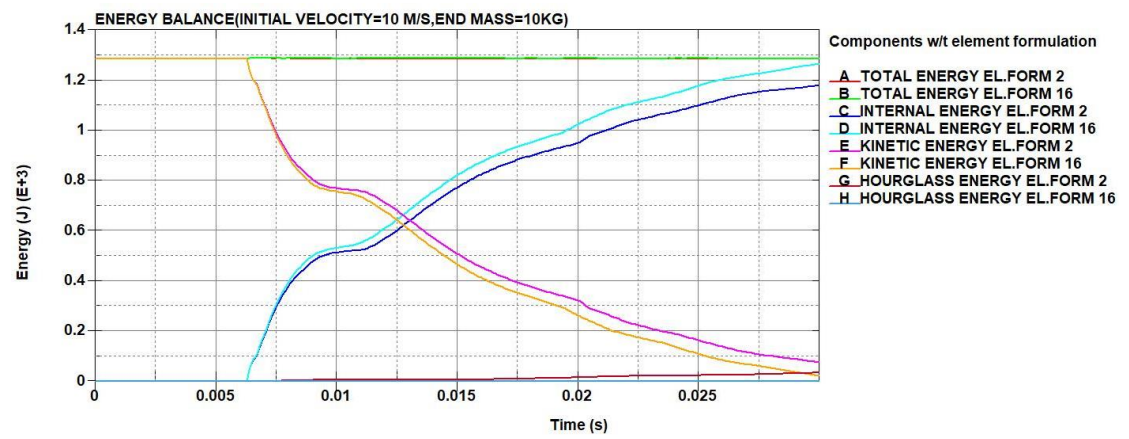


Figure 71 - Cross beam with elastoplastic material (perfect plasticity) with punctual masses (10 kg, 10 m/s) energy balance

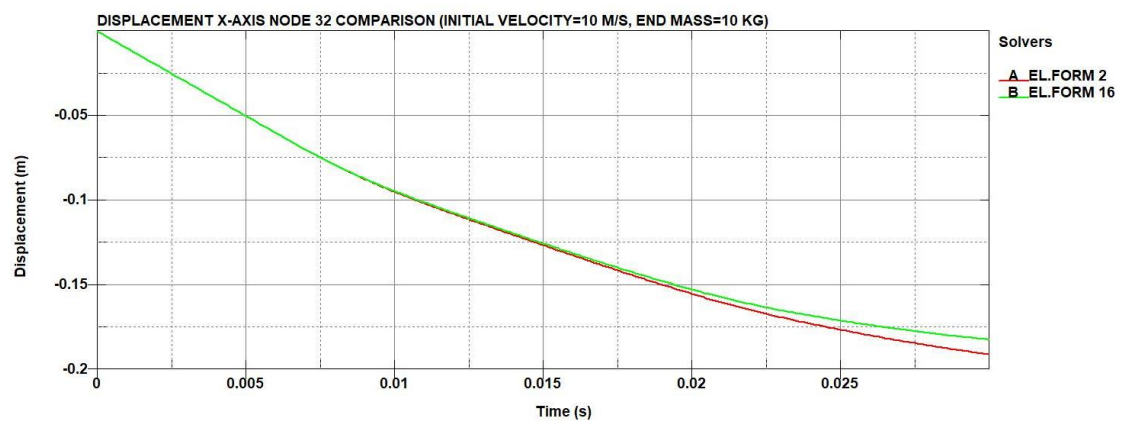


Figure 72 - Cross beam with elastoplastic material (perfect plasticity) with punctual masses (10 kg, 10 m/s) node 32 x-axis displacement

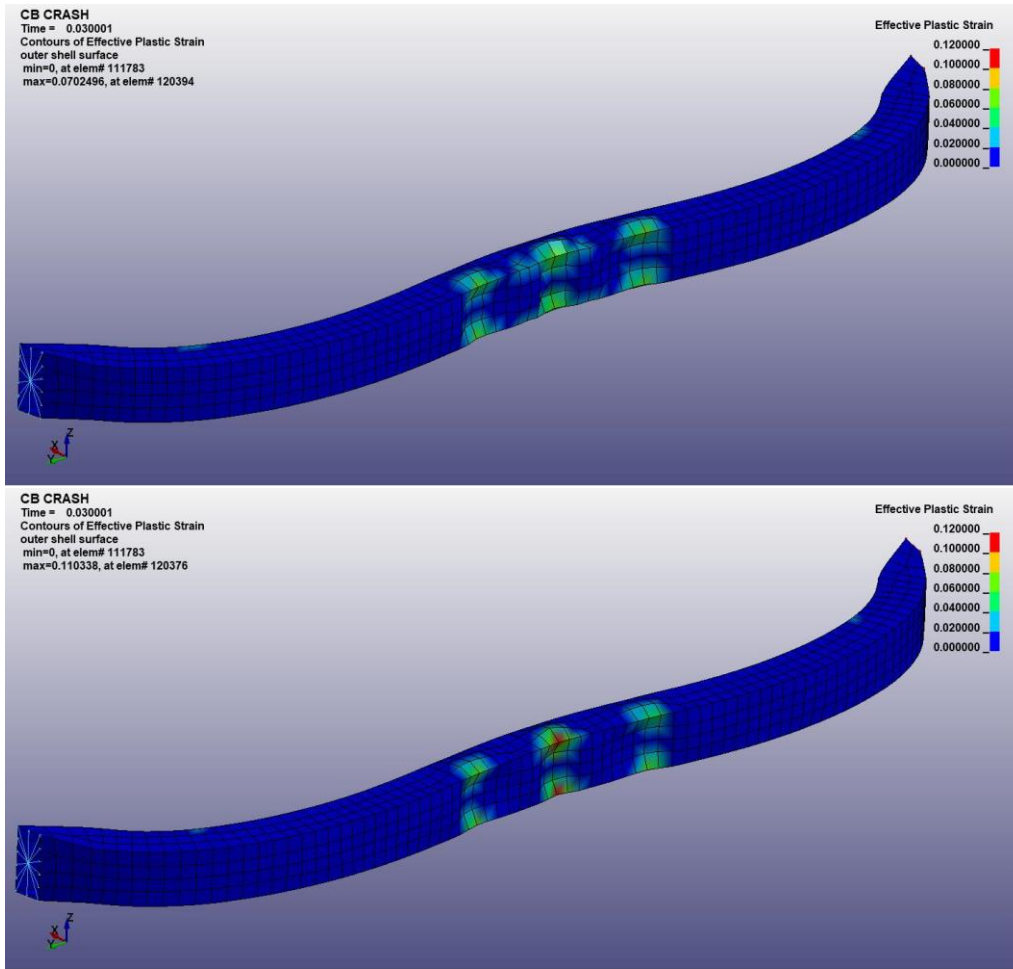


Figure 73 - Cross beam with elastoplastic material (perfect plasticity) with punctual masses (10 kg, 10 m/s) effective plastic strain of EL FORM 2 (top) and EL FORM 16 (bottom)

and 0.11 for the full integration). In the second case (20 kg, 20 m/s), the energy absorption of the fully integrated element formulation is still higher compared to the reduced integration formulation (figure 74). The displacement of node 32 (figure 75) also displays a similar trend to the previous case for both element formulations. The collapsing of both ends of

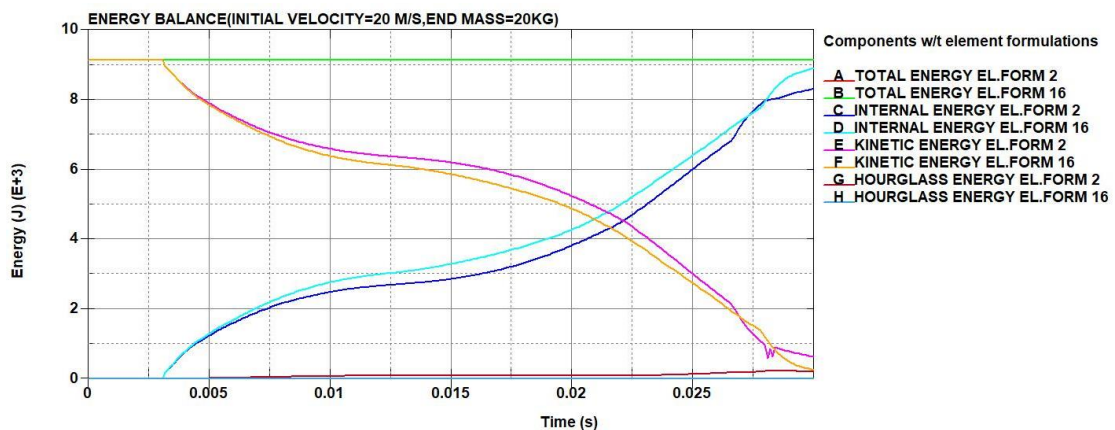


Figure 74 - Cross beam with elastoplastic material (perfect plasticity) with punctual masses (20 kg, 20 m/s) energy balance

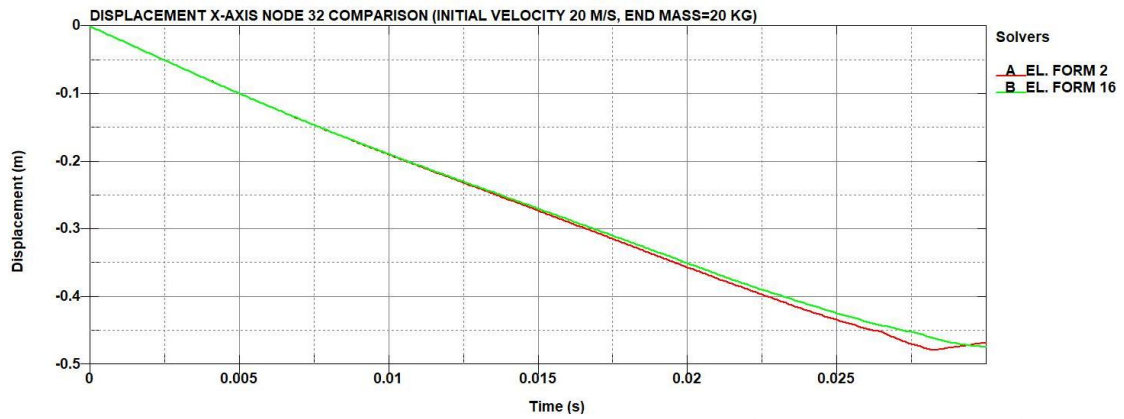


Figure 75 - Cross beam with elastoplastic material (perfect plasticity) with punctual masses (20 kg, 20 m/s) node 32 x-axis displacement

the part is also more significant in this case, as well as a higher maximum effective plastic strain on the fully integrated element formulation (figure 76) (0.276 for the reduced intergration and 0.288 for the full integration). From this comparison is concluded that, in LS-Dyna, by increasing the mass at each end of the cross beam, the results between the reduced integrated and fully integrated element formulation have a small but acceptable difference.

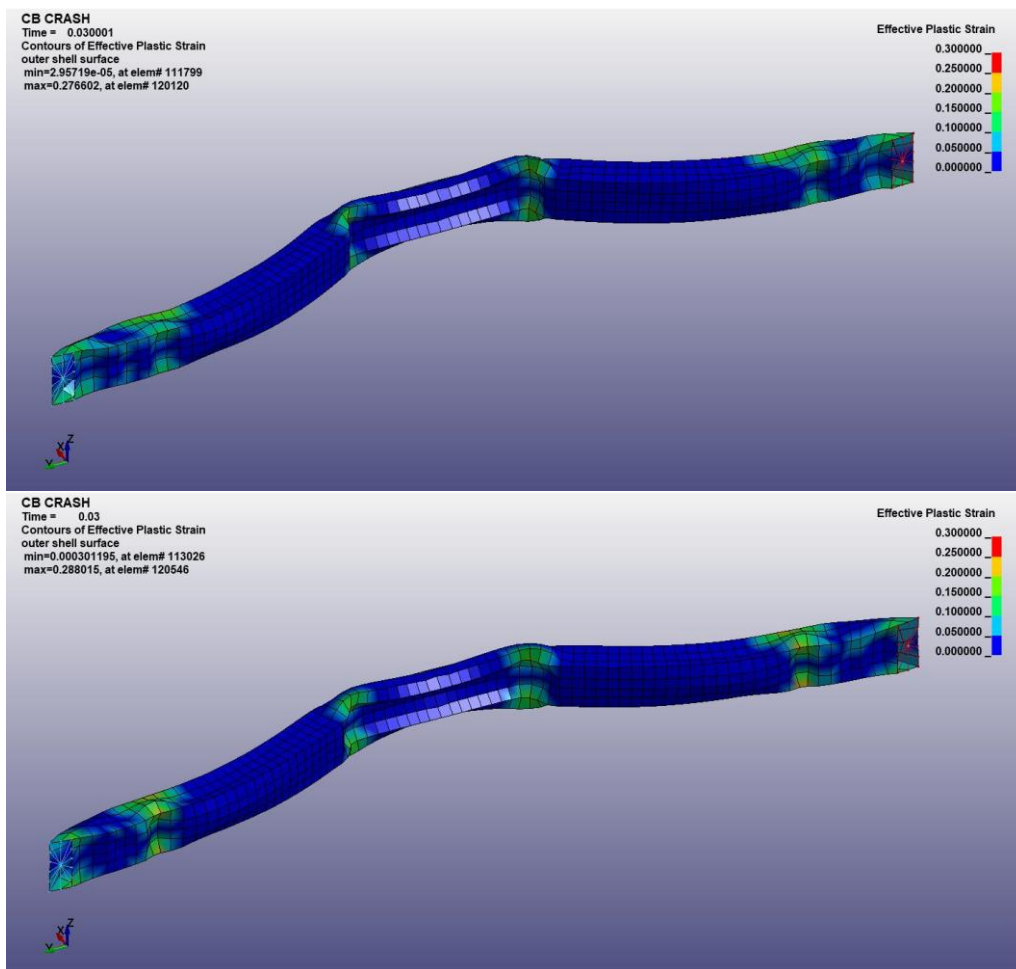


Figure 76 - Cross beam with elastoplastic material (perfect plasticity) with punctual masses (20 kg, 20 m/s) effective plastic strain of EL. FORM 2 (top) and EL. FORM 16 (bottom)

5.3.5. Code comparison with elastoplastic material with hardening curve

For this final task, simulations are performed on the part with an elastoplastic material assigned to the part with hardening curve (stress is not constant after the yield stress value). The material assigned is from the first release of the NI vehicle model. To simulate a hardening curve, the material card to be used in LS-Dyna is the 024-PIECEWISE_LINEAR_PLASTICITY. No additional masses are added to each end, thus no CNRBs are assigned. The part is tested at the same two initial velocities as in previous case, comparing the two different element formulations as before (EL. FORM 2 and EL. FORM 16, with hourglass control on EL. FORM 2 as in previous cases. Upon analysis of the energies (figure 77), it is obvious that there is a significant difference between the two solvers. This is due to the different density used for this part in the complete model, which is higher than the realistic value and the one used in Europlexus. In the current version of the model, SVS FEM has chosen to model only the most important components

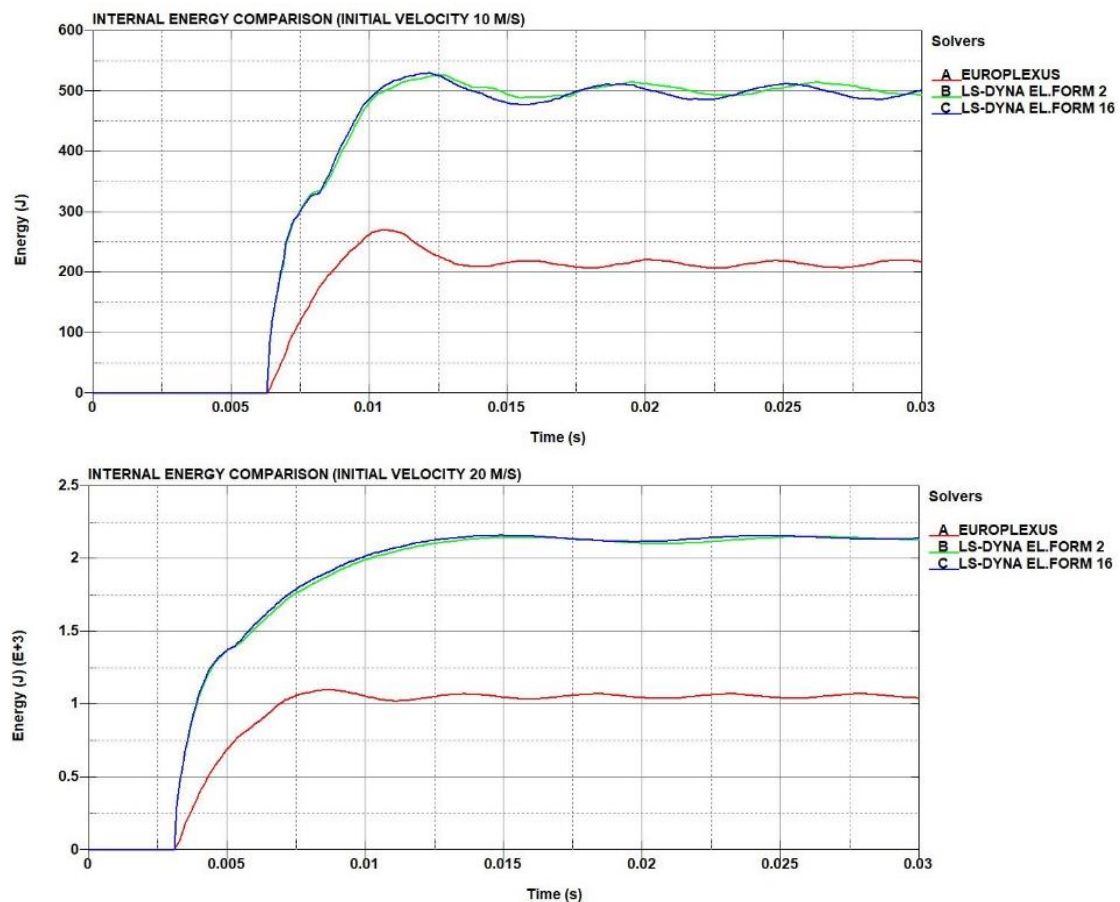


Figure 77 - Cross beam with material from NI vehicle model internal energy at 10 m/s (top) and 20 m/s (bottom)

and to distribute the mass of others, by increasing the value of the (realistic) density by a factor allowing to conserve the overall mass. Adjustment of the mass is necessary, because the total mass of the vehicle is the most important parameter regarding the behaviour of the barrier under impact. This applied methodology of spreading the “missing” mass uniformly has to be verified from two aspects:

- Spreading the mass uniformly, by increasing the density in the material model, could lead to a displacement of the centre of gravity, which can impair the model’s ability to be representative of real vehicles.
- Increasing the material density could influence the crashing behaviour of components. To avoid this effect, the density should be increased only for the components which are not deformed significantly during the impact. To verify how much a component is participating in the impact against the barrier, its maximum internal energy value is measured. If this value is relatively low, then it is acceptable to increase the density value without affecting the crash behaviour.

However, for the code comparison between EPX and LS-Dyna on this simple component, the mass has to be corrected to a realistic value of 7800 kg/m³. The rest of the material properties are preserved from the previous case, and the part is tested at the same initial velocities and element formulations. Regarding the 10 m/s initial velocity, the results of the energy output (figures 78 and 79) show that the behaviour of the part without perfect plasticity has very similar behaviour to the perfect plasticity material. This is also apparent

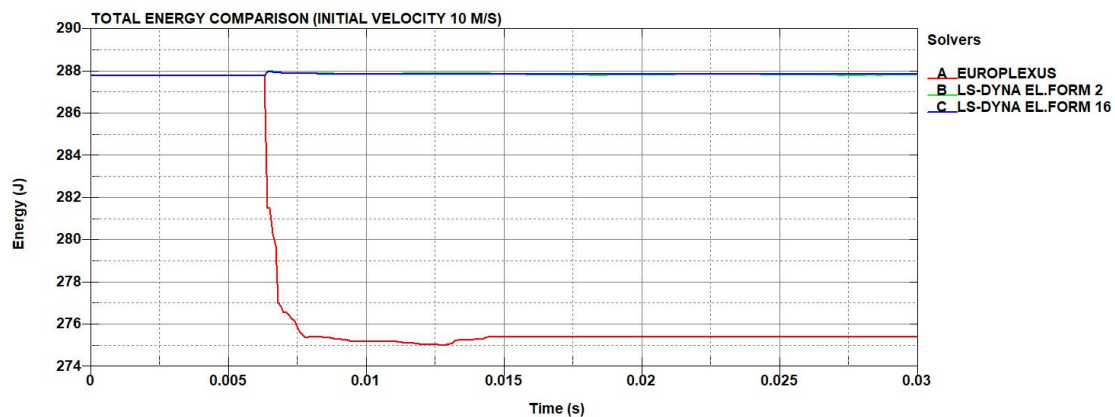


Figure 78 - Cross beam with material from NI vehicle model (with density correction) total energy (@ 10 m/s)

from the node 32 displacement (figure 80). From the contact force (which is zoomed to the area of interest) (figure 81) and momentum graphs (figure 82), there are differences between the two solvers, especially in the contact force graph. The momentum graphs are introduced in order to have an

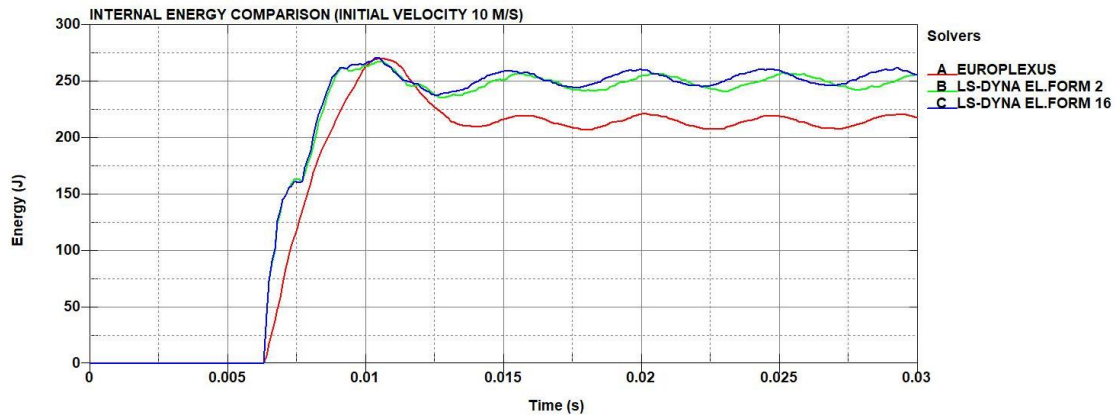


Figure 79 - Cross beam with material from NI vehicle model (with density correction) internal energy (@ 10 m/s)

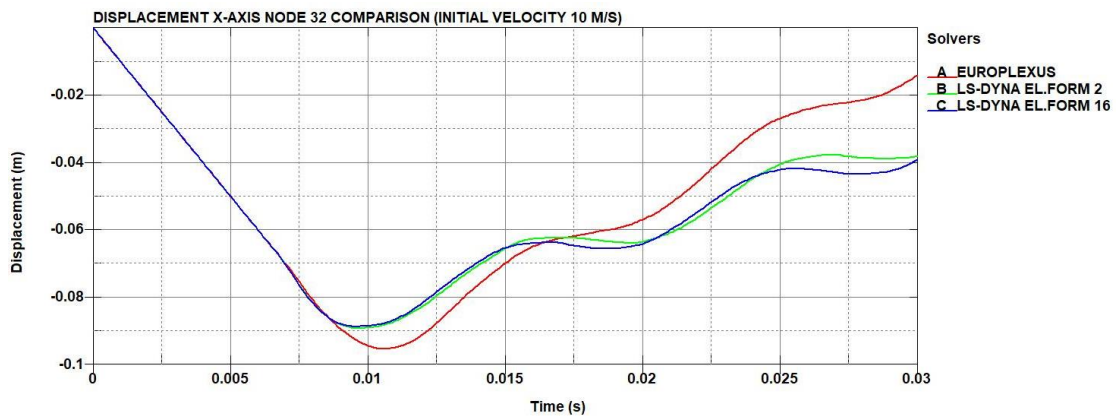


Figure 80 - Cross beam with material from NI vehicle model (with density correction) x-axis displacement of node 32 (@ 10 m/s)

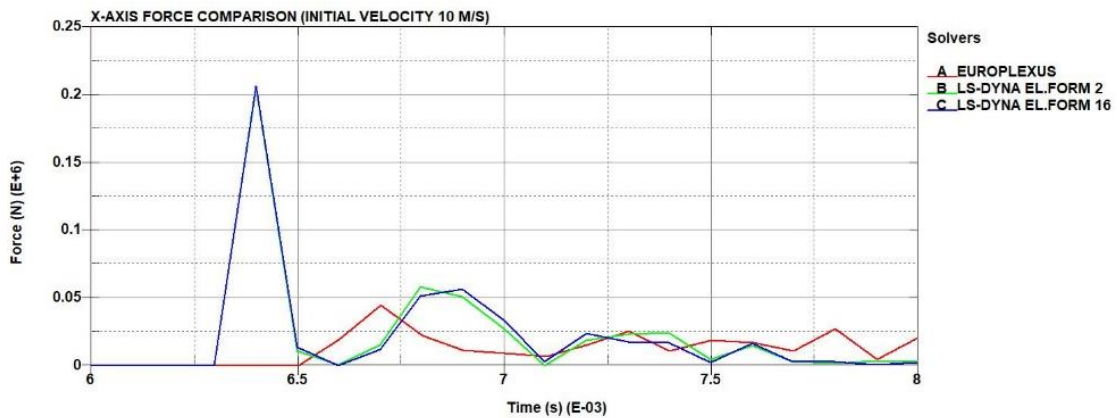


Figure 81 - Cross beam with material from NI vehicle model (with density correction) x-axis contact force (@ 10 m/s)

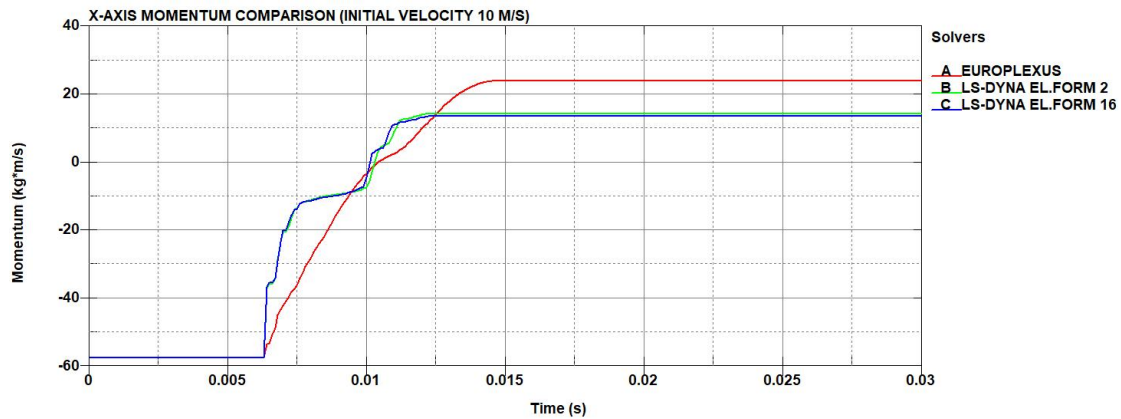


Figure 82 - Cross beam with material from NI vehicle model (with density correction) x-axis momentum (@ 10 m/s)

alternative method to estimate the contact force, when the force results between the two solvers are very different. The two element formulations in LS-Dyna display minimal difference. For the 20 m/s case, the total energy (figure 83), internal energy (figure 84) and displacement of node 32 (figure 85) results also present similar behaviour to the part with the perfect plasticity material. Regarding the force (figure 86), there is a difference between both solvers, where the peak may be more accurately captured in

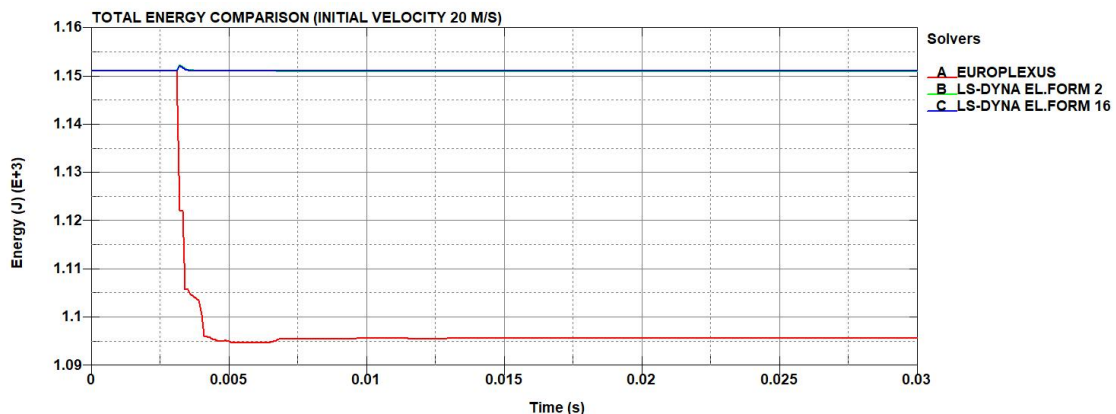


Figure 83 - Cross beam with material from NI vehicle model (with density correction) total energy (@20 m/s)

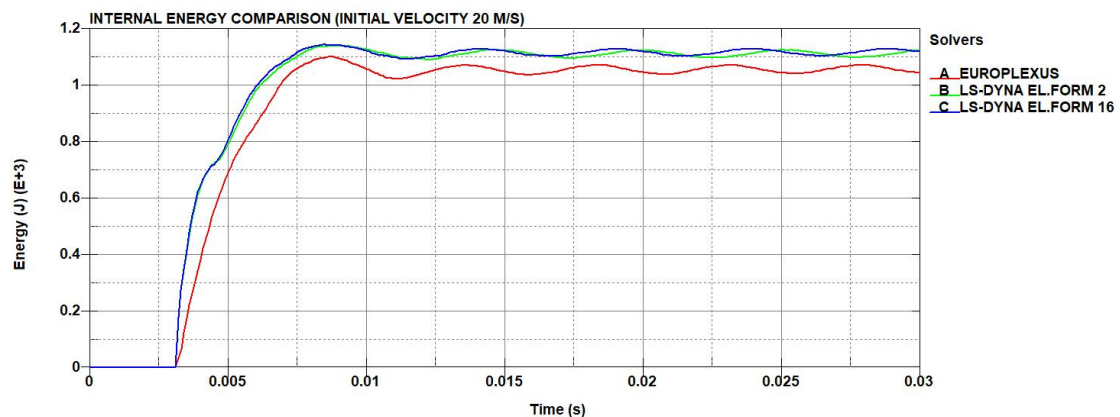


Figure 84 - Cross beam with material from NI vehicle model (with density correction) internal energy (@ 20 m/s)

the same timeframe, but the value from the LS-Dyna is very different to the one from Europlexus. The momentum results (figure 87) are also in this case closer together, as in the case of the material with perfect plasticity. In this case, the momentum is the preferred method of calculating the contact force, compared to the contact force output signal because there are differences on this output between the two solvers. Finally, from a

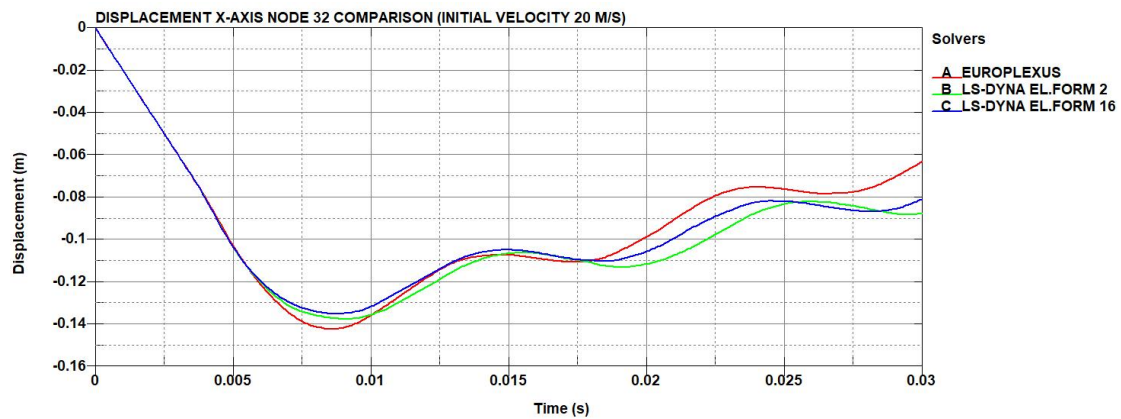


Figure 85 - Cross beam with material from NI vehicle model (with density correction) node 32 x-axis displacement (@20 m/s)

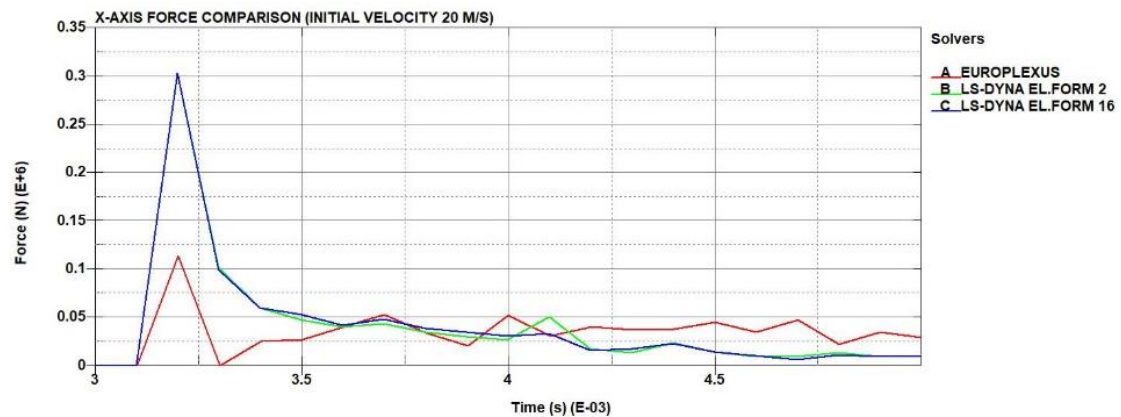


Figure 86 - Cross beam with material from NI vehicle model (with density correction) x-axis contact force (@ 20 m/s)

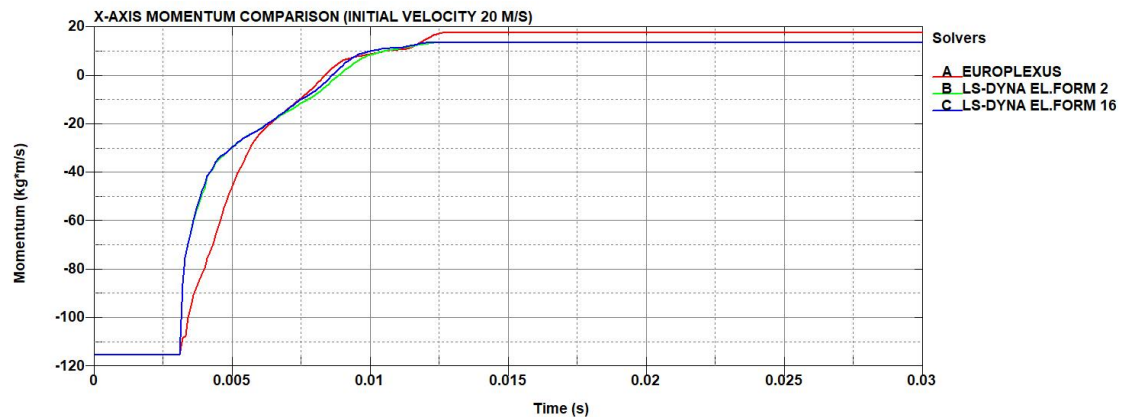


Figure 87 - Cross beam with material from NI vehicle model (with density correction) x-axis momentum (@ 20 m/s)

comparison of the effective plastic strain maps (figure 88) it is observed that Europlexus gives a much larger plasticized zone than LS-Dyna, which was also apparent in the case of the perfect plasticity material. In conclusion, for the material with hardening curve, the results are closer between the two solvers for higher velocity. In the LS-Dyna results, there are very small differences between the two element formulations. This difference between the two solvers, which is acceptable, is due to the energy dissipation in Europlexus because of the different contact models used by each solver.

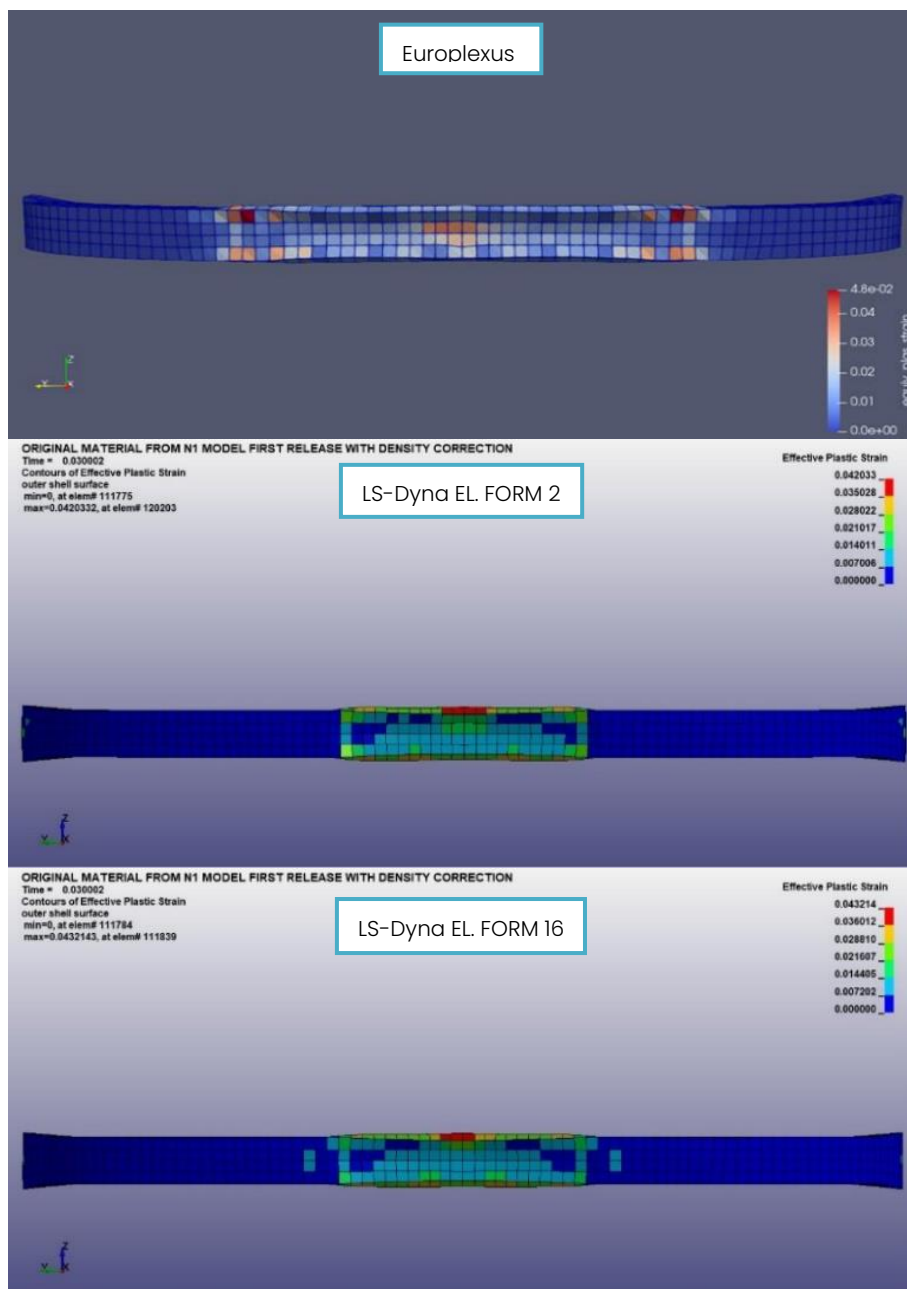


Figure 88 - Cross beam with material from N1 vehicle model (with density correction) effective plastic strain maps (@20 m/s)

5.4. Submodel 1

The next step in the code comparison is to introduce a new model to perform the comparison between the two solvers. This new model has

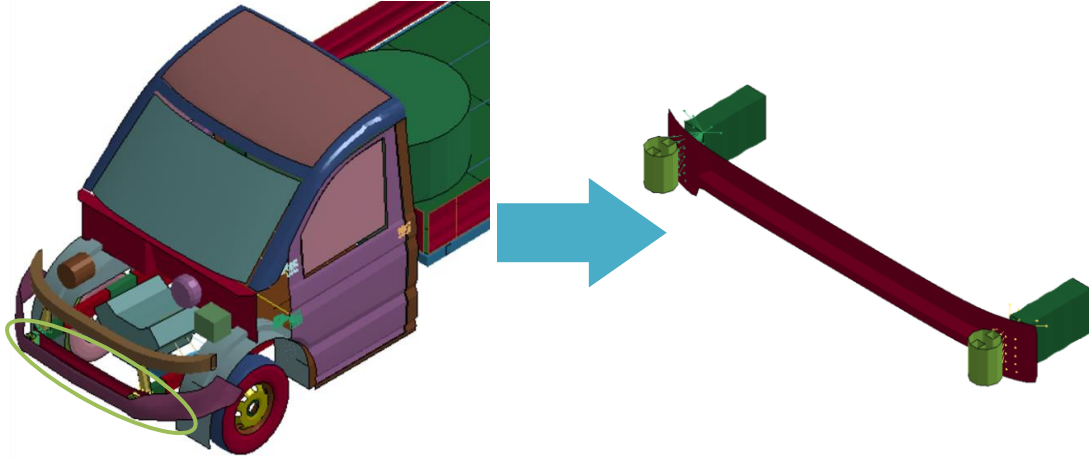


Figure 89 – Submodel 1 model extraction

increased complexity than the previous one, and it is also extracted from the NI Generic Vehicle Model (figure 89). This model is comprised of three parts (figure 90), where those parts together are named “submodel 1” (or “subassembly 1”):

- PART 3 – Frame Crush Zone
- PART 6 – Frame Front Bumper
- PART 142 – Front Bumper Absorbing Member

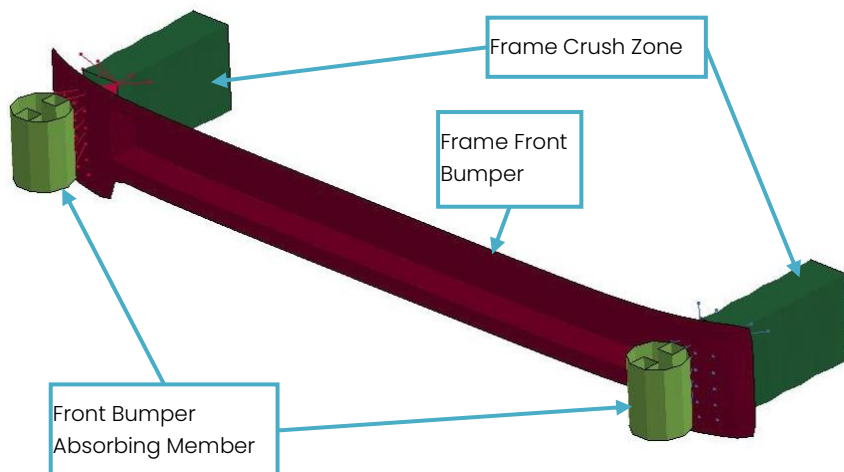


Figure 90 – Submodel 1 parts

The parts of the model are connected together with CNRBs (Constraint Nodal Rigid Bodies). For this model, the impact is going to be performed for one initial velocity of 20 m/s. All parts are comprised of shell elements and their

formulation is set to EL. FORM 16, which is the fully integrated element (as in the Europlexus solver). Thus the HOURGLASS keyword can be eliminated. The thicknesses of the parts are assigned as:

- Part 3: 2 mm
- Part 6: 2.5 mm
- Part 142: 1.5 mm

The LS-Dyna solver used in this case, is the R11.2 SMP double precision.

5.4.1. Code comparison with elastic material

The first comparison is going to be performed on a purely elastic material. The material in LS-Dyna is simulated using the keyword 001_ ELASTIC. The same material is applied to all parts. Its properties are:

- Density: 7800 kg/m³
- Young modulus: 210 GPa
- Poisson ratio: 0.28

The contact model used for this simulation is the AUTOMATIC_SURFACE_TO_SURFACE, with no friction assigned to it, following the computations with the Europlexus solver. From the energy balance comparison (figure 91), the results obtained are very close between the two solvers and as in the case of the cross beam simulations, with a dissipation of energy in the Europlexus results due to the different contact model. The results from LS-Dyna are slightly affected by a local vibration phenomenon from the “Frame front bumper”, after 0.02 ms (figure 92). A modal analysis has been performed for the first five modes of the bumper, free and constrained in the points

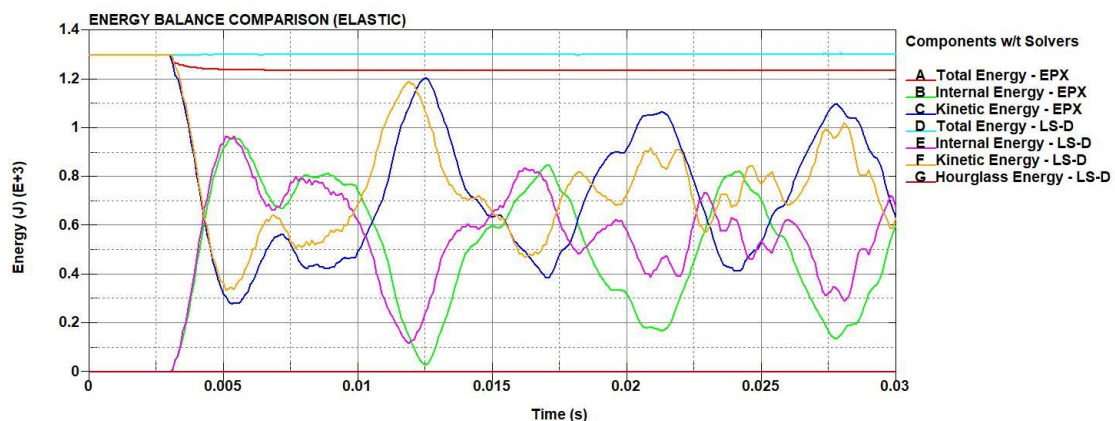


Figure 91 - Submodel 1 elastic material energy balance

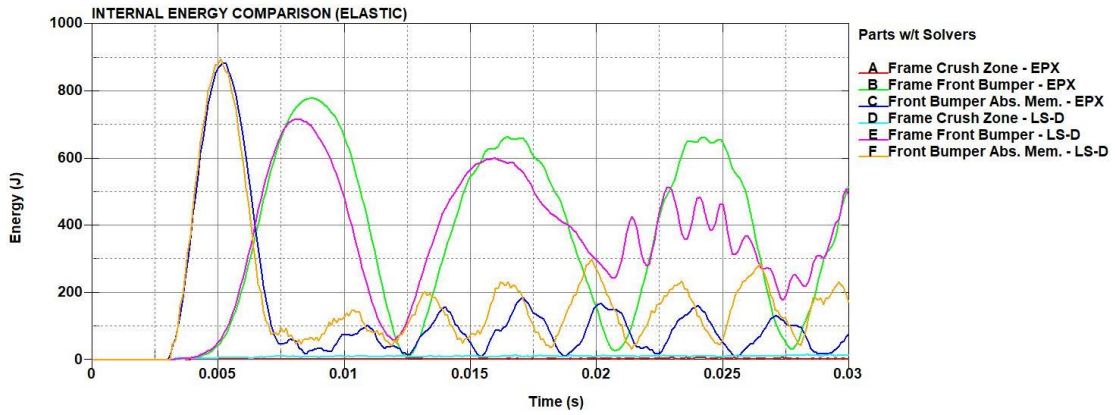


Figure 92 - Submodel 1 elastic material internal energy by part

connected with the CNRB, by also changing the element formulation from full to reduced integration. It has been verified that the local vibration phenomenon is affected from the element formulation used, with smaller differences in the first two modes regarding the shape and frequency, but more significant differences in the next modes. Here in the contact force output (figure 93), there are differences between the two solvers. Thus, the force should be calculated from the momentum (figure 94) since the results are closer together. The momentum output is a more reliable method to

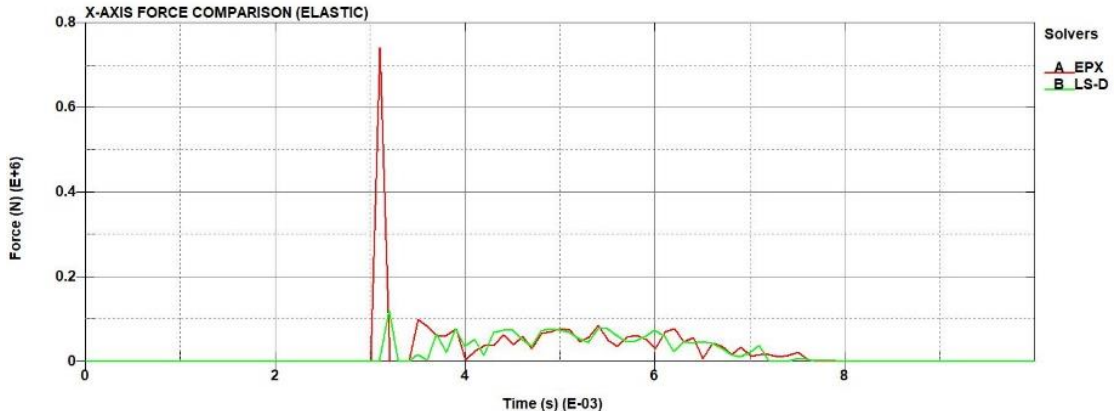


Figure 93 - Submodel 1 elastic material x-axis contact force

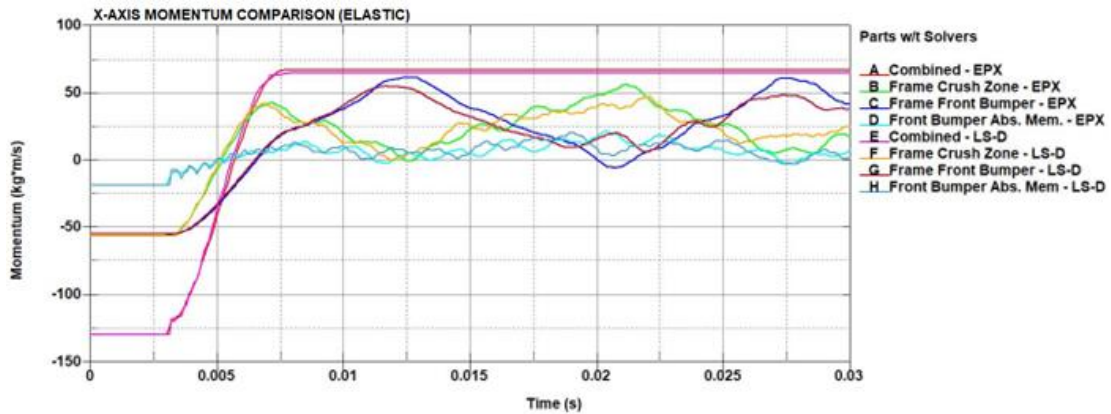


Figure 94 - Submodel 1 elastic material x-axis momentum

calculate the contact force because it cuts out discrepancies (e.g., high frequency components) that can affect the force output signal.

5.4.2. Code comparison with elastoplastic material

The next step in the simulations on the submodel 1, is to perform simulations with an elastoplastic material. The material is proposed by JRC,

1	MID	RO	E	PR	SIGY	ETAN	FAIL	TDEL
	201	7800.0000	2.100e+11	0.2800000	3.500e+08	0.0	0.3016667	0.0
2	C	P	LCSS	LCSR	VP			
	0.0	0.0	0	0	0.0			
3	EPS1	EPS2	EPS3	EPS4	EPS5	EPS6	EPS7	EPS8
	0.0016667	0.0266667	0.0516670	0.1016667	0.1516670	0.2016667	0.2516667	0.3016667
4	ES1	ES2	ES3	ES4	ES5	ES6	ES7	ES8
	3.500e+08	4.000e+08	4.300e+08	4.700e+08	4.920e+08	5.050e+08	5.170e+08	5.220e+08

Figure 95 – Elastoplastic material proposed by JRC

and is an elastoplastic material with hardening line. The material card to be used is the 024-PIECEWISE_LINEAR_PLASTICITY, with the parameters as shown in the figure 95 (units are in kg, m, Pa). The same material is applied to all parts. For the contact model in LS-Dyna, the AUTOMATIC_SINGLE_SURFACE keyword is added to simulate the self-contact of the parts. Again,

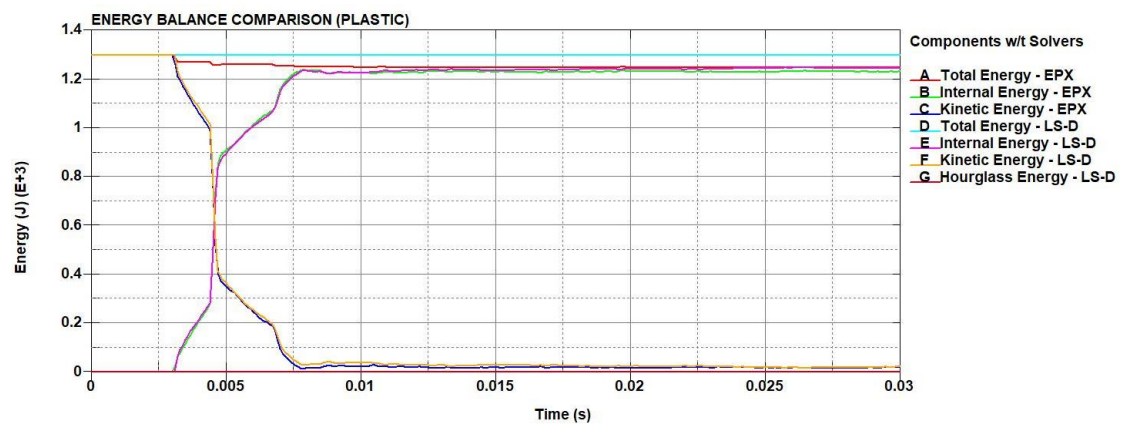


Figure 96 – Submodel 1 elastoplastic material energy balance

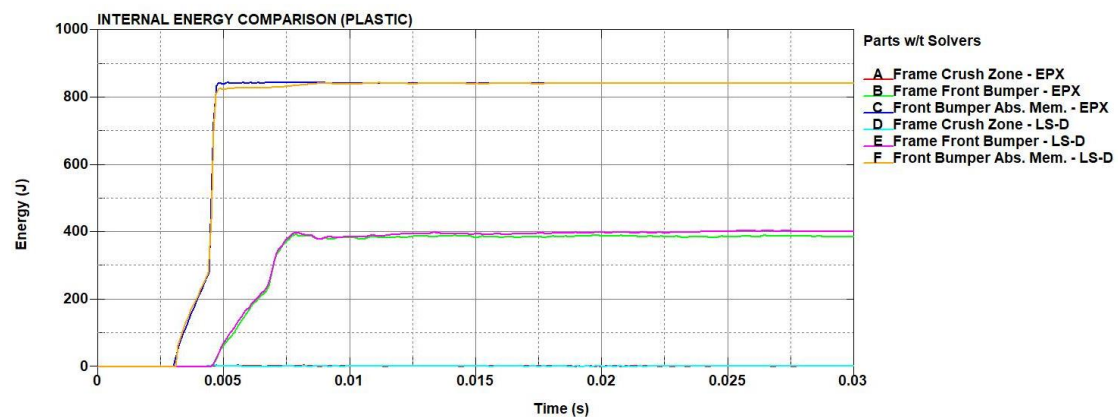


Figure 97 – Submodel 1 elastoplastic material internal energy by part

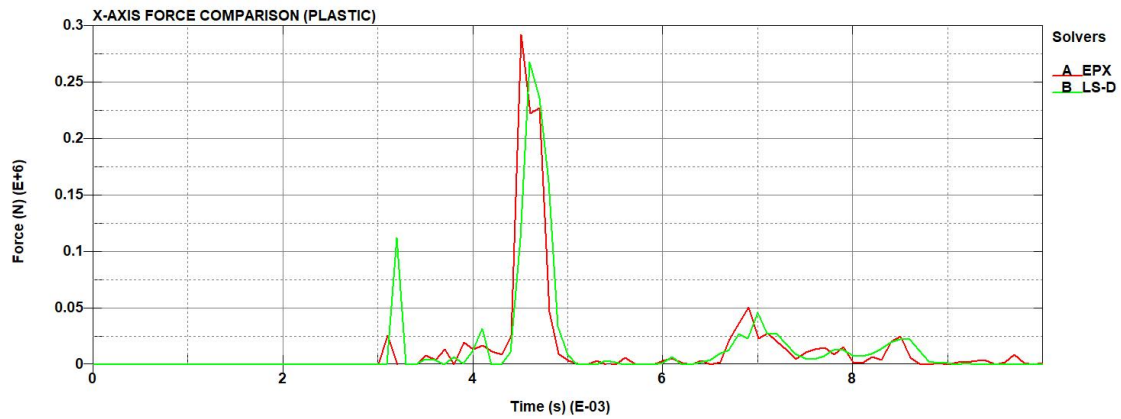


Figure 98 - Submodel 1 elastoplastic material x-axis contact force

all the elements have the fully integrated formulation, and the initial velocity is 20 m/s. In the case of the elastoplastic material, from the energy results (figures 96 and 97) it is observed that LS-Dyna results are closer to the Europlexus results compared to the elastic material case, with a dissipation of energy in the Europlexus, due to the different contact model. From the contact force graph (figure 98), LS-Dyna gives more accurate results than the elastic material case, by better capturing the timeframe of the largest peak and its size. There are some discrepancies between the two solvers, but overall, the force output gives satisfying results. The momentum graph also

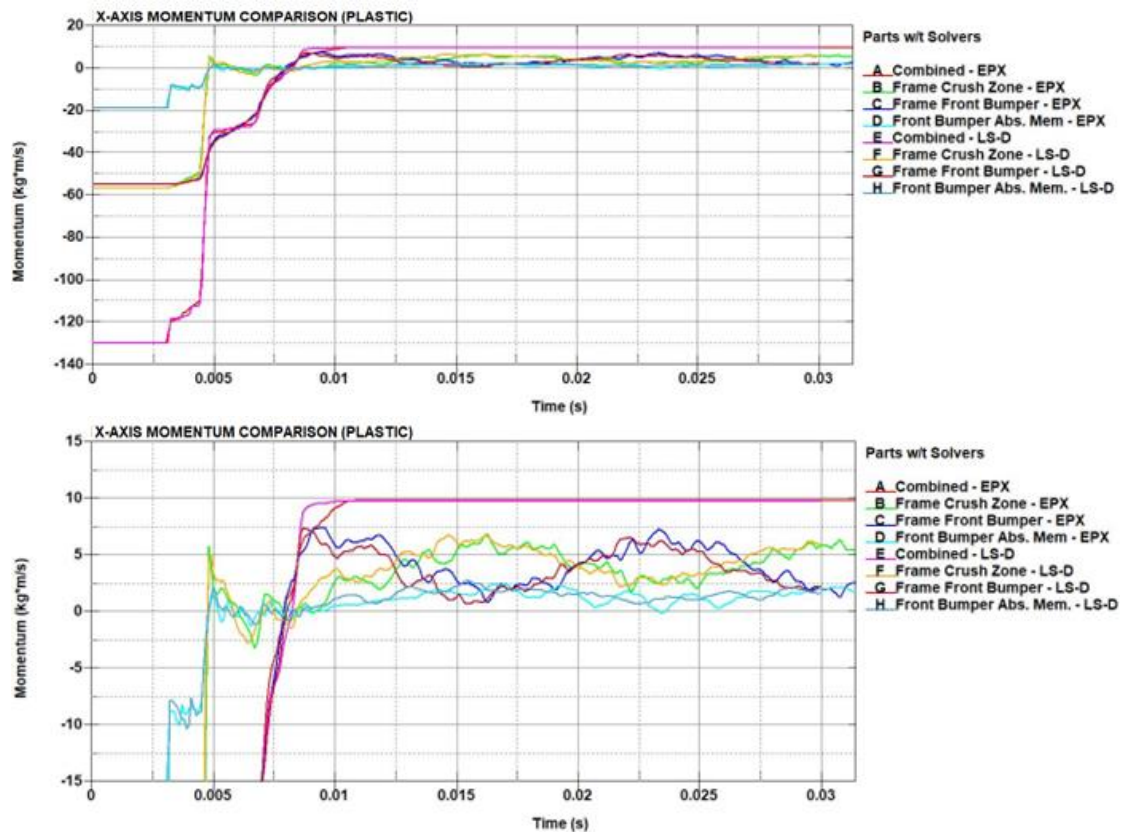


Figure 99 - Submodel 1 elastoplastic material x-axis momentum complete graph (top) and zoomed section (bottom)

indicates very accurate results from LS-Dyna (figure 99). Finally, comparing the effective plastic strain maps (figure 100), LS-Dyna represents more accurately the map of Europlexus, in contradiction with the cross beam simulations where the plasticized zone of Europlexus was not accurately captured by LS-Dyna.

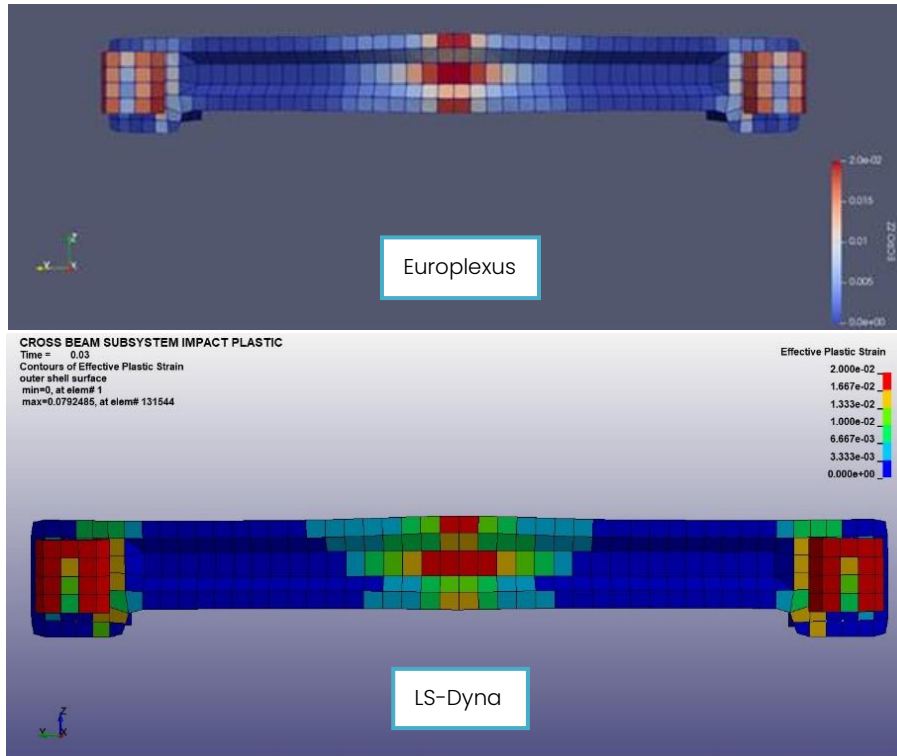


Figure 100 – Submodel 1 elastoplastic material effective plastic strain maps

5.4.3. Code comparison with elastoplastic material on a refined mesh

The final comparison to be performed in the submodel 1 is a mesh refinement for the elastoplastic material. The refined mesh simulations are proposed to verify how sensitive the results are to the mesh density. The element length was divided by two, thus there are 4 times more shell elements in this case (figure 101) because the parts are comprised only with

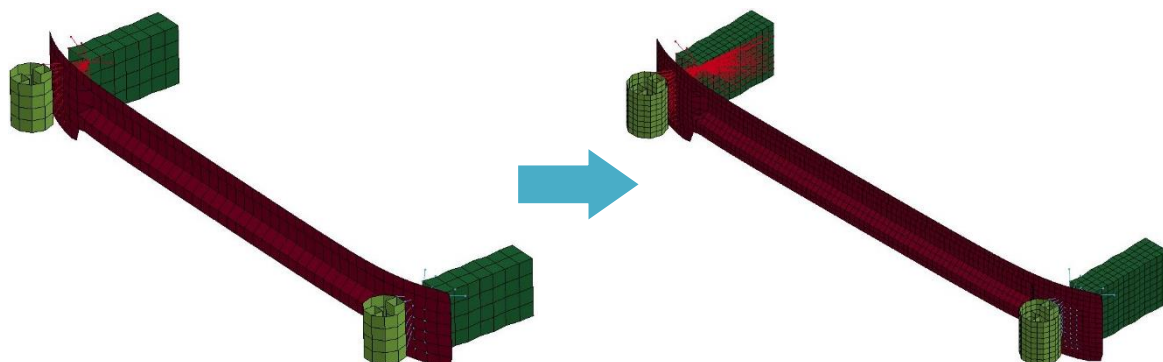


Figure 101 – Submodel 1 original model (left) and fine mesh model (right)

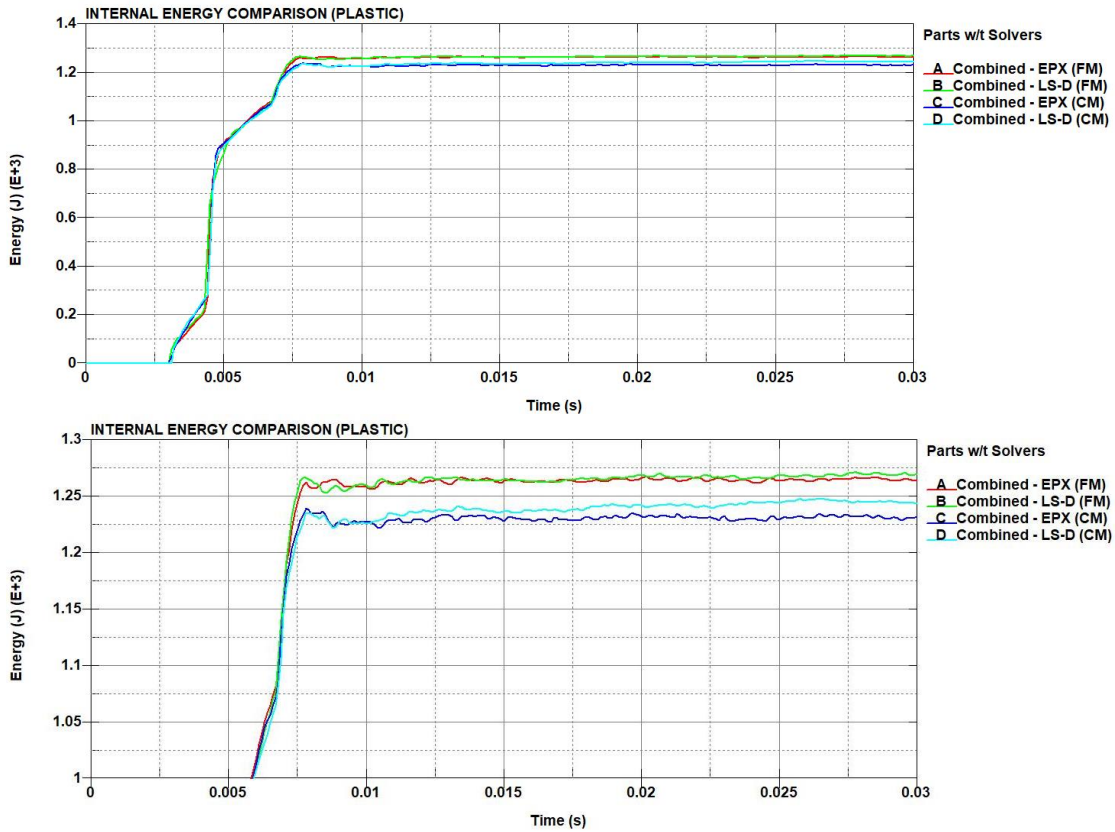


Figure 102 - Submodel 1 elastoplastic material fine mesh (FM) and coarse mesh (CM) internal energy complete graph (top) and zoomed section (bottom)

4 node elements. From the result comparison, it is visible that the coarser mesh tends to slightly underestimate the internal energy (figure 102). However, the results from LS-Dyna are close to both cases. For the finer mesh, the internal energy (mainly plastic dissipation) is quite concentrated in the part “Front bumper absorbing member” (figure 103). The difference in the internal energy between the two meshes for this component is about 5%, which is not negligible, but is acceptable with respect to the overall accuracy that is targeted for this model. Regarding the contact force (figure 104) LS-

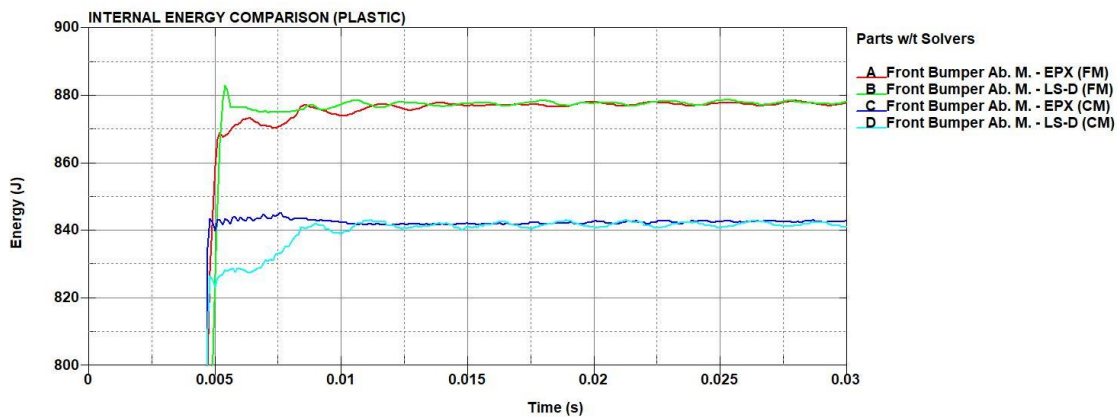


Figure 103 - Submodel 1 elastoplastic material fine mesh (FM) and coarse mesh (CM) “Front bumper absorbing member” internal energy

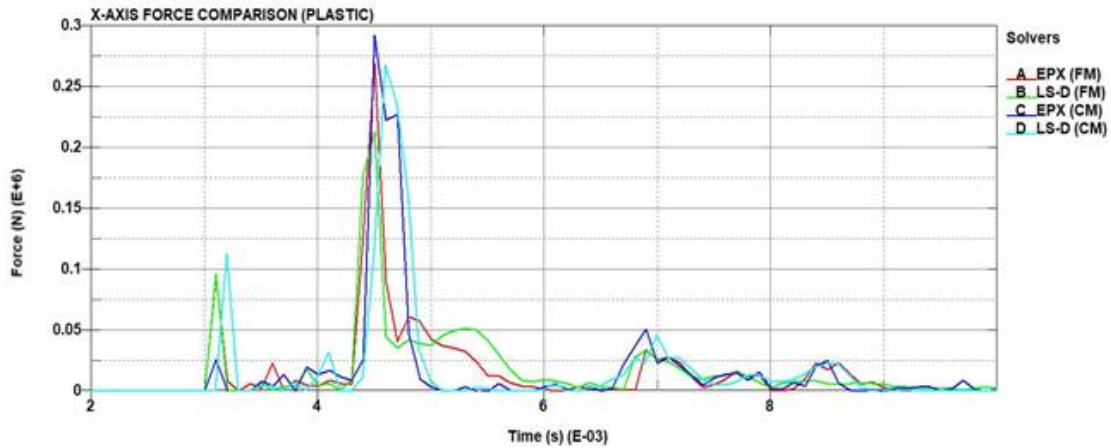


Figure 104 - Submodel 1 elastoplastic material fine mesh (FM) and coarse mesh (CM) x-axis contact force

Dyna follows more accurately the force results from Europlexus in the finer mesh submodel than the coarse mesh, however there is a difference between the results of the original and refined mesh. The momentum (figure 105) has a smoother curve with the refined mesh in both solvers. From the comparisons performed so far, the momentum has proven to be a more reliable method of calculating the force with respect to the contact force output, due to the fact that the contact force output is affected by the mesh size, high frequency components that require filtering, and very little from the

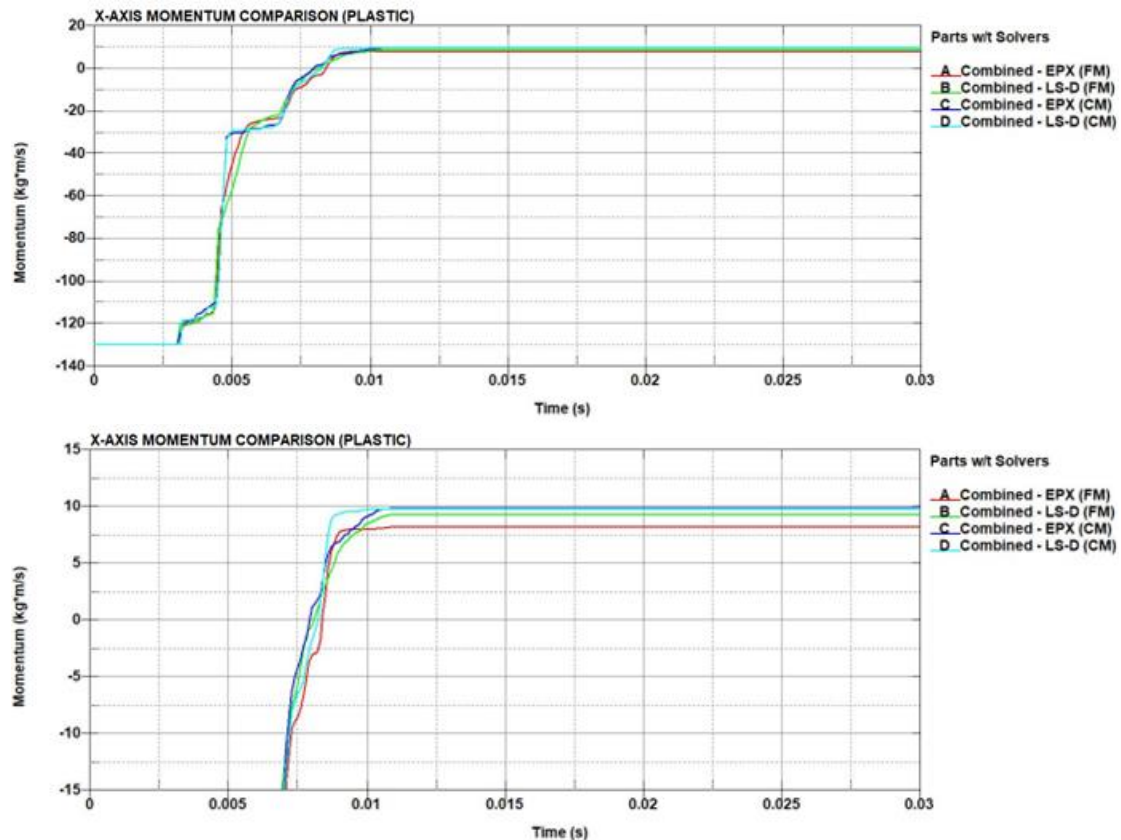


Figure 105 - Submodel 1 elastoplastic material fine mesh (FM) and coarse mesh (CM) x-axis momentum complete graph (top) and zoomed section (bottom)

element formulation. In terms of the global distribution of the plastic strain, the original version (figure 100) and refined mesh version (figure 106) give consistent results. From the Europlexus results, an important increase of about 50% in the maximum effective plastic strain is noted. The LS-Dyna results also present some increase in the maximum effective plastic strain. This is due to that value being localised in a single element. Therefore the maximum effective plastic strain is very sensitive to the element size.

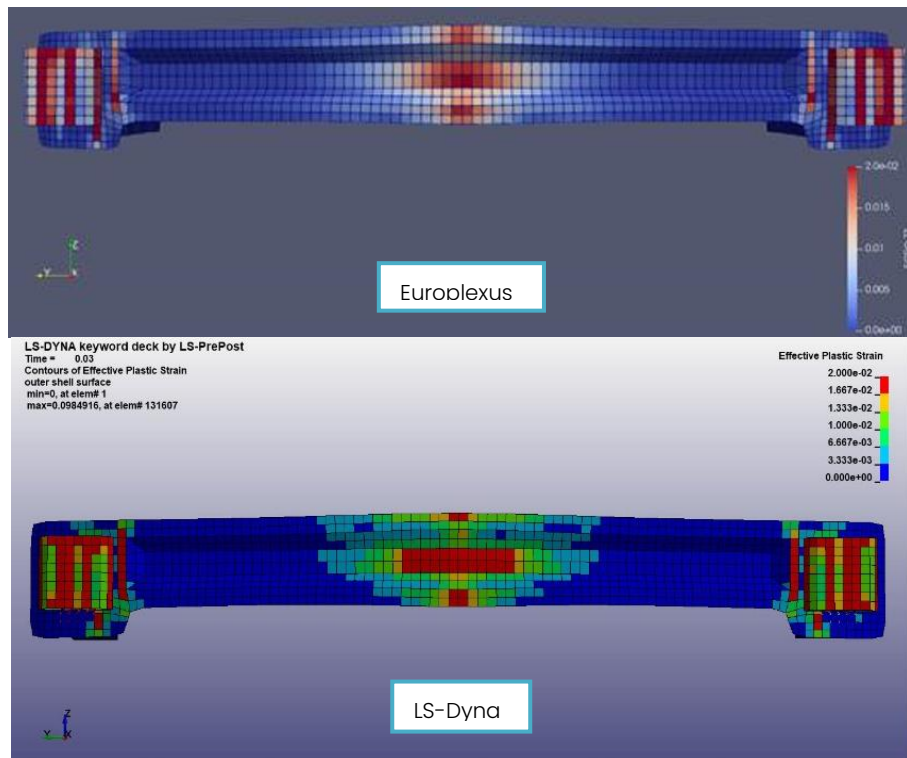


Figure 106 – Submodel 1 elastoplastic material fine mesh effective plastic strain maps

5.5. Submodel 2

Following up the code comparison between Europlexus and LS-Dyna is to introduce a new model to perform comparisons. As previously

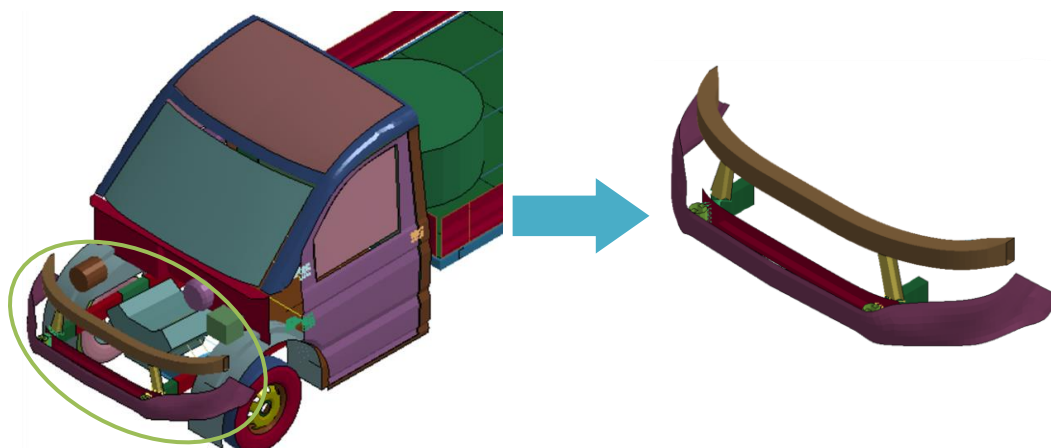


Figure 107 – Submodel 2 extraction

mentioned, the goal of the comparison is to add models with increasing complexity, making the model more realistic, and examining the differences between the two codes as complexity increases. This model, referred to as "submode 2" (or "subassembly 2") (figure 107). The submodel 2 is also extracted from the first release of the NI Generic Vehicle Model, and it is made up of six parts (figure 108):

- PART 3 – Frame Crush Zone
- PART 6 – Frame Front Bumper
- PART 125 – Front Vertical Member
- PART 126 – Front Cross Member
- PART 132 – Front Fascia Bottom
- PART 142 – Front Bumper Absorbing Member

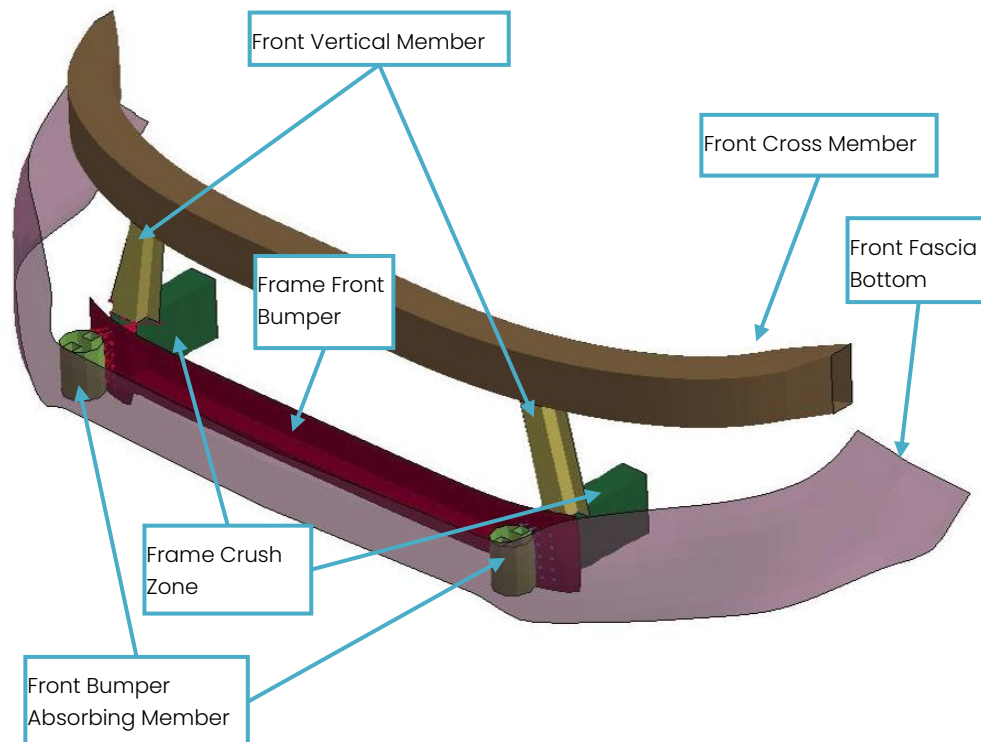


Figure 108 – Submodel 2 parts

Connections of the parts in the model are as such:

- Parts 3,6,125,142 are connected with CNRB (Constraint Nodal Rigid Bodies)
- Parts 3,125,126 are connected with common nodes
- Part 132 is not connected to any part

For this model, the impact is going to be performed for one initial velocity of 20 m/s. The thicknesses of the parts are assigned as:

- Frame Crush Zone: 2 mm
- Frame Front Bumper: 2.5 mm
- Front Vertical Member: 1.5 mm
- Front Cross Member: 1 mm
- Front Fascia Bottom: 3 mm
- Front Bumper Absorbing Member: 1.5 mm

The LS-Dyna solver used in this case, is R11.2 double precision SMP.

5.5.1. Code comparison with elastic material

First comparison is going to be performed on a purely elastic material, with the same material applied to all the parts. In this simulation, the element formulation is preserved from the NI model, where all the parts have fully integrated elements (EL. FORM 16) except from the parts “Front cross member” and “Front fascia bottom”, which are in reduced integrated element formulation (EL. FORM 2), with the same hourglass control used in the cross beam simulations. The material is simulated using the keyword 001_ELASTIC. Its properties are

- Density: 7800 kg/m³
- Young modulus: 210 GPa
- Poisson ratio: 0.28

The contact model used for this simulation is the AUTOMATIC_SURFACE_TO_SURFACE, with no friction assigned to it, following the computations with

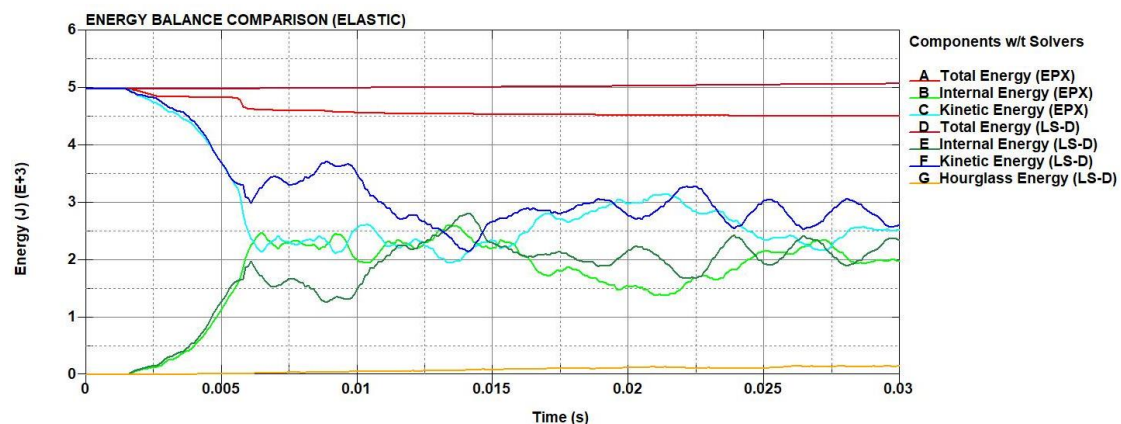


Figure 109 - Submodel 2 with elastic material energy balance

the Europlexus solver. The impact velocity is 20 m/s. From the energy balance (figure 109) it is clear that Europlexus loses a non-negligible amount of total energy, which is due to the contact model used by that solver. The dissipated energy is higher than the previous cases. The difference in the results between the two solvers is also visible from the parts “Front vertical member” (figure 110) and “Front bumper absorbing member” (figure 111). Comparing the contact force (figure 112) and momentum (figure 113) graphs, it is clear that there are some differences, especially in the force output. To

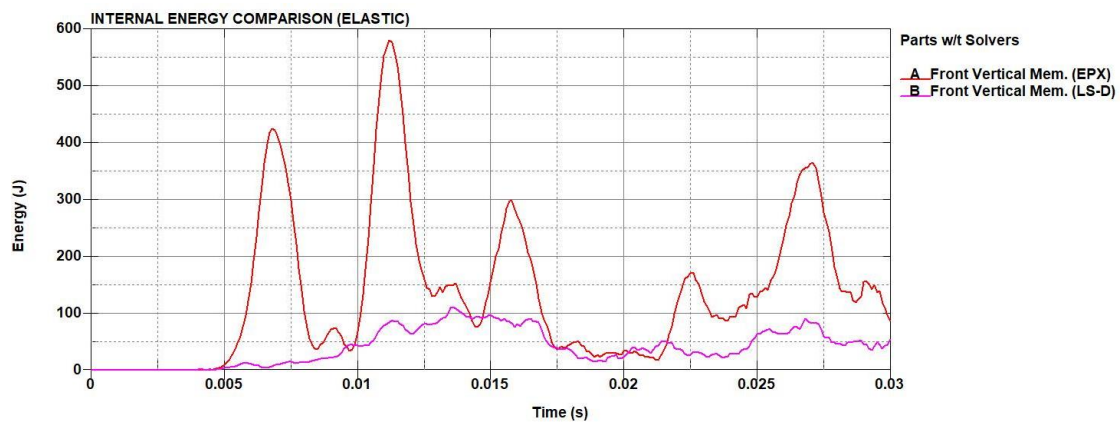


Figure 110 - Submodel 2 with elastic material “Front vertical member” internal energy

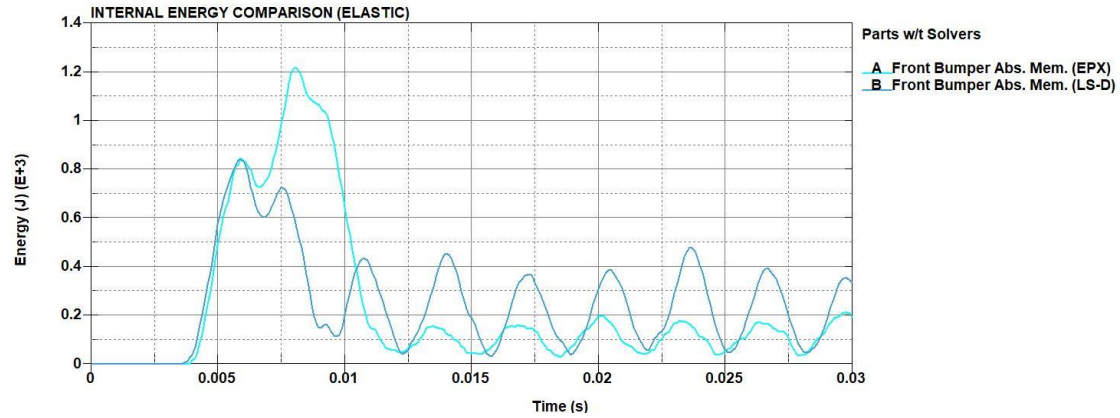


Figure 111 - Submodel 2 with elastic material “Front bumper absorbing member” internal energy

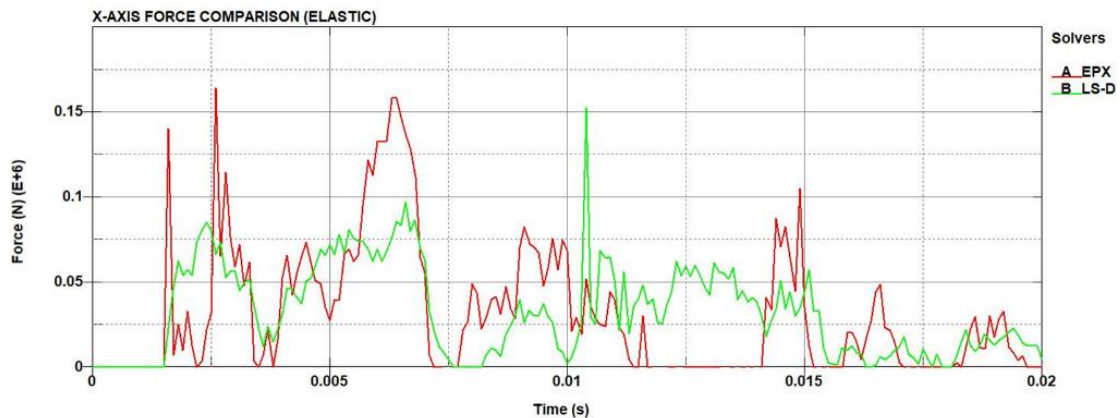


Figure 112 - Submodel 2 with elastic material x-axis contact force

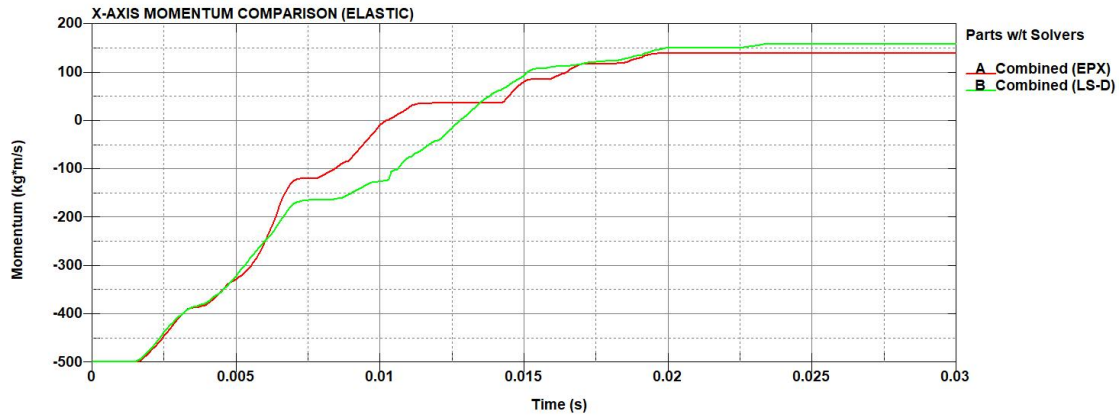


Figure 113 - Submodel 2 with elastic material x-axis momentum

verify the results, a simulation with all the parts of the model with fully integrated elements was performed, and the results had very similar behaviour with the model with mixed element formulation. As in previous cases, the main differences between the two solvers lie on the different contact model used by each solver, where in Europlexus there is a dissipation of energy upon impact.

5.5.2. Code comparison with elastoplastic material

To continue the code comparison for the submodel 2, for a more realistic application than the elastic case, an elastoplastic material with hardening curve is chosen for the next step. The material assigned is proposed by JRC and it has been used in the previous simulations of the submodel 1 impact. The material card to be used is the 024_PIECEWISE_LINEAR_PLASTICITY, with the parameters as shown in the figure 95. For the contact model in LS-Dyna, the AUTOMATIC_SINGLE_SURFACE keyword is added to simulate the self-contact of the parts. The impact velocity is 20 m/s. Observing the energy results (figure 114), there is a visible difference in the results between the two codes at around 4 ms of the internal energy. This

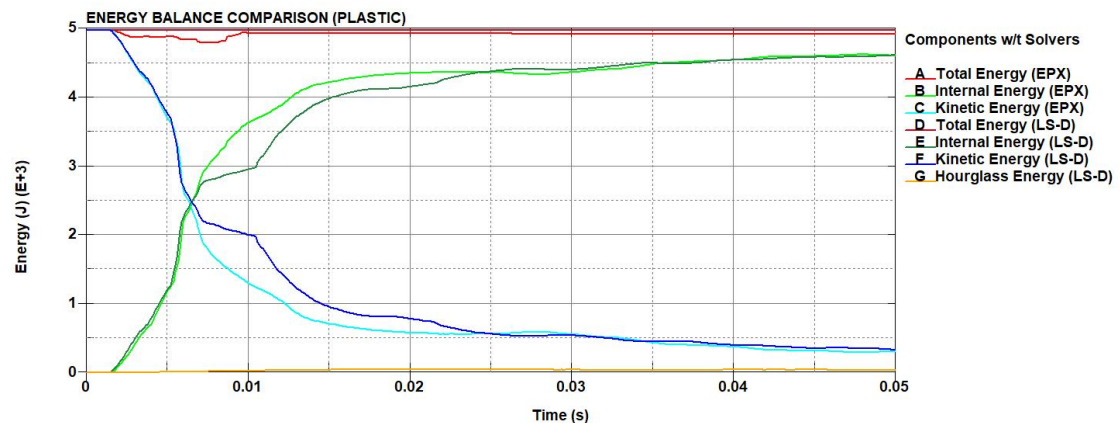


Figure 114 - Submodel 2 with elastoplastic material energy balance

timestamp is the point where all the contacts intervening at the point of impact, as confirmed from the Europlexus simulations. In the Europlexus simulations, a significant amount of the internal energy is captured by the “Front vertical member” and much less by the “Front cross member”, whereas with LS-Dyna the internal energy behaviour of both parts is inverted (figures 115 and 116). From the contact force graph (figure 117), the results provide more accurate contact force data by comparing the two solvers. However, the momentum graph (figure 118) is again providing reliable

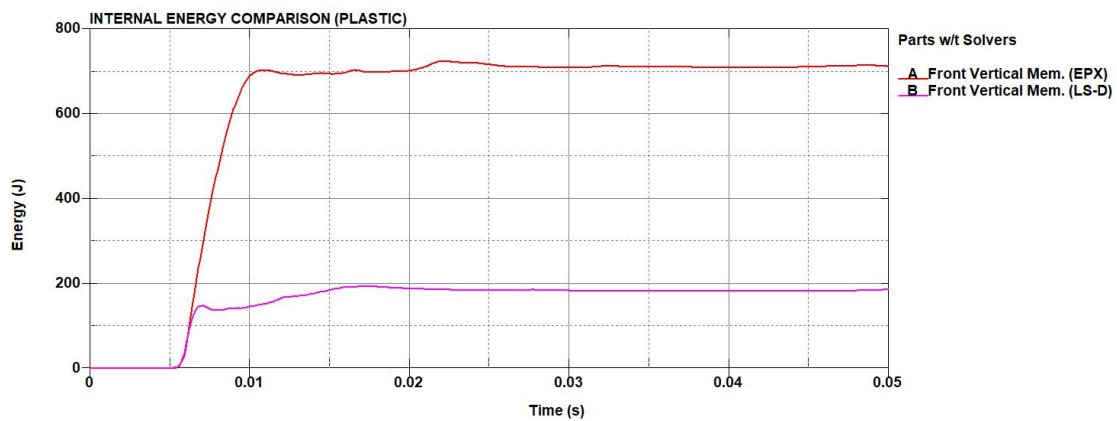


Figure 115 - Submodel 2 with elastoplastic material “Front vertical member” internal energy

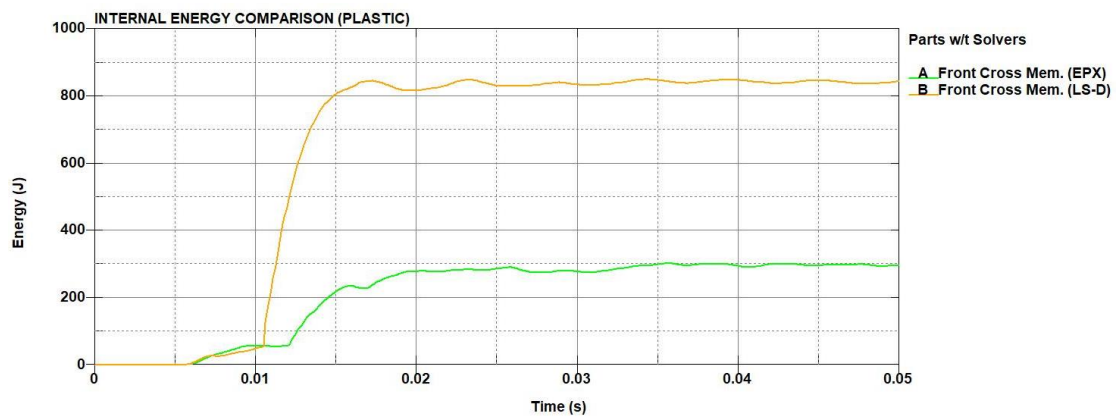


Figure 116 - Submodel 2 with elastoplastic material “Front cross member” internal energy

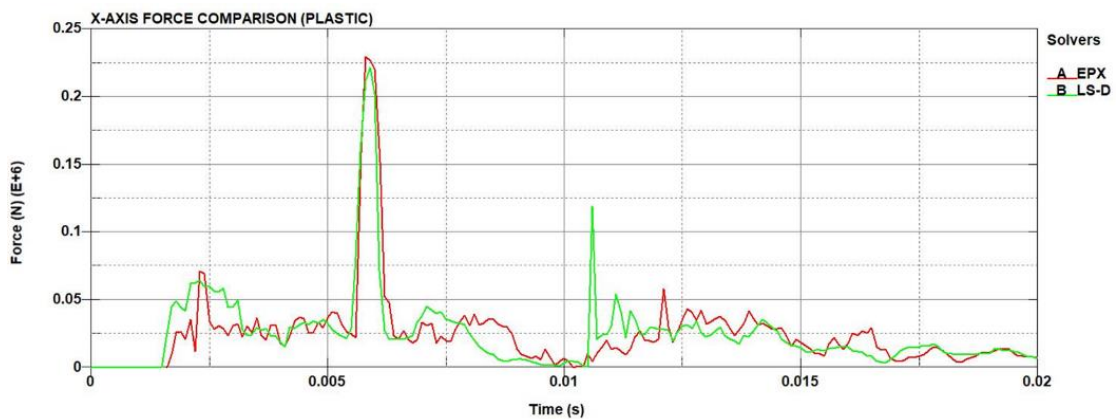


Figure 117 - Submodel 2 with elastoplastic material x-axis contact force

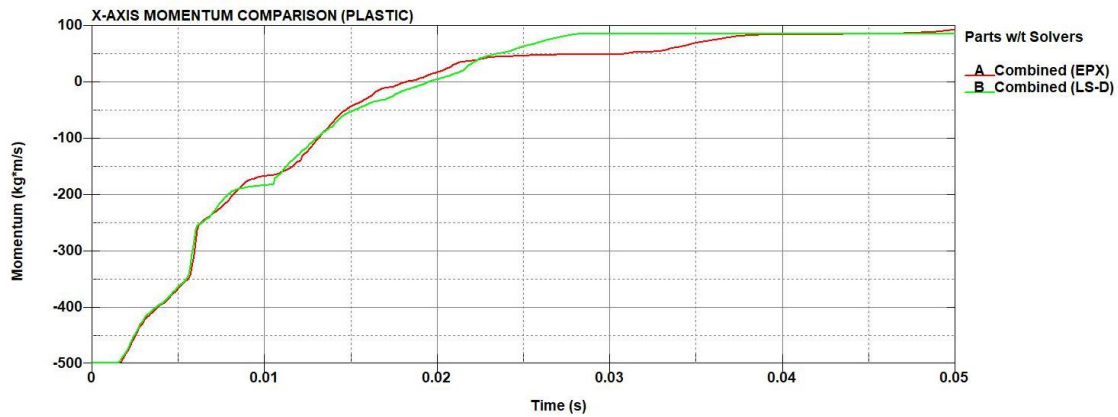


Figure 118 - Submodel 2 with elastoplastic material x-axis momentum

results, and the difference between the two solvers is small. From the effective plastic strain maps (figure 119), the results are close and the difference between the two solvers have not exceeded 10%. The main difference between them lies in a non-negligible rigid body rotation that occurs during the impact in the LS-Dyna simulations (figure 120). Apart from the rotation, the code is very close between the two solvers. In Europlexus there are relatively important limitations that are not practical to apply rigid

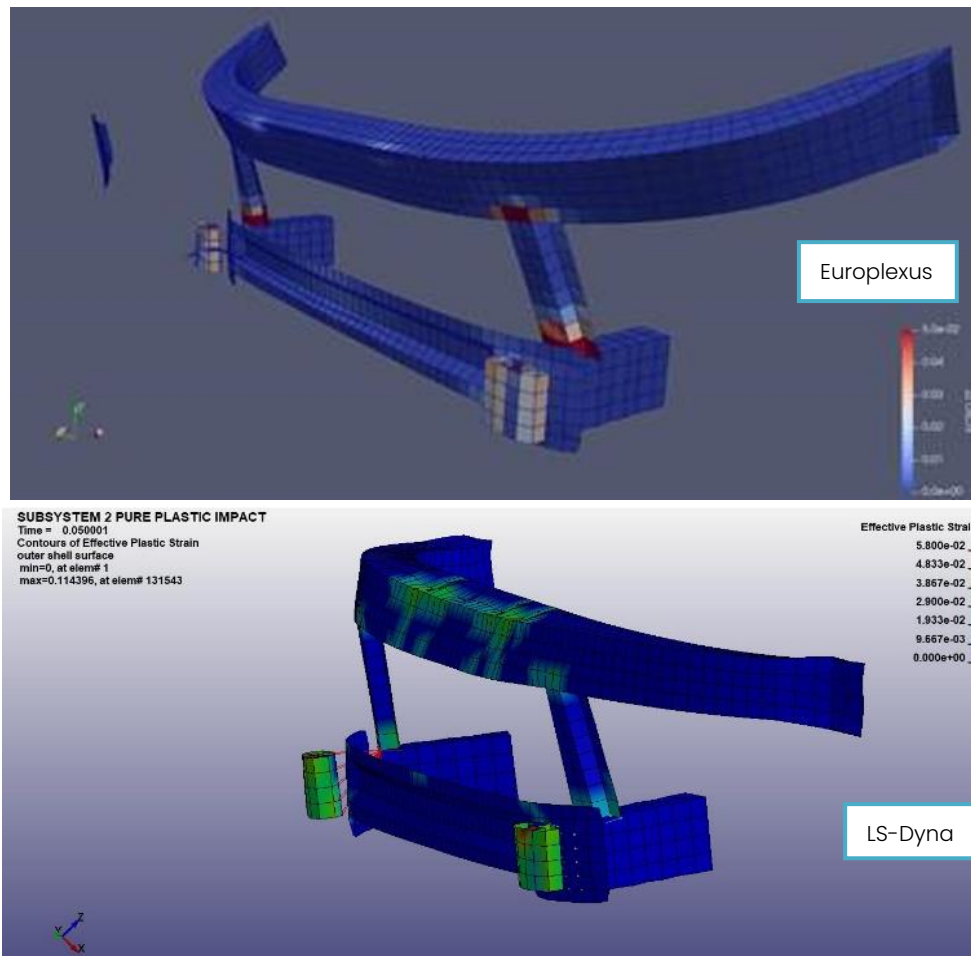


Figure 119 - Submodel 2 with elastoplastic material effective plastic strain maps

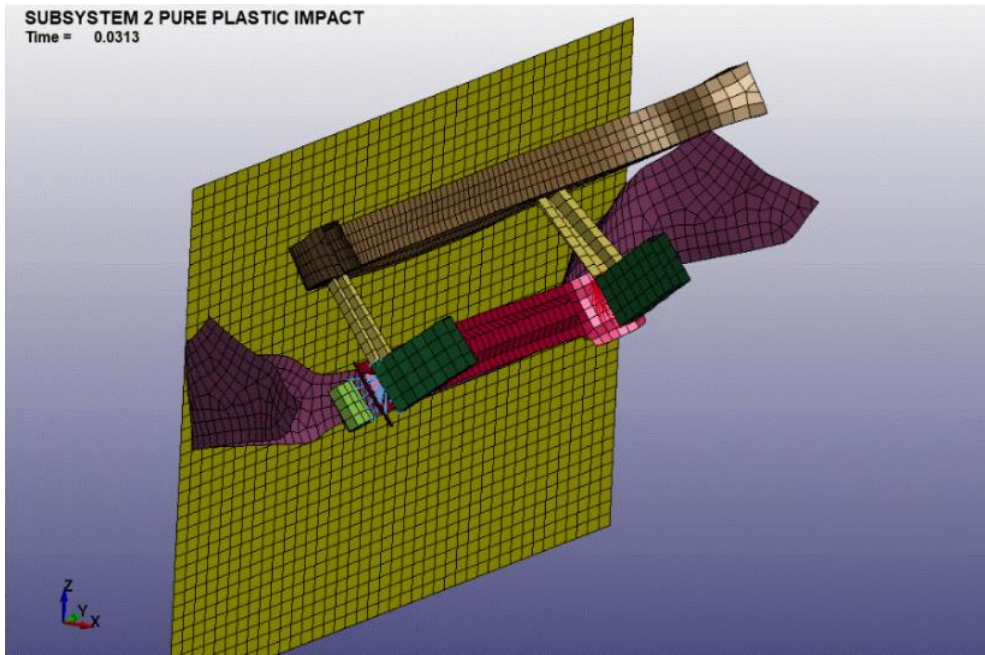


Figure 120 - Submodel 2 model with elastoplastic material rotation upon impact with the wall barrier

connections between nodes and/or parts without blocking rigid body rotations. For this reason, the deformation energy distribution obtained with Europlexus and LS-Dyna are not the same in the submodel 2 simulations, where the non-negligible rigid body rotation occurs during the impact. From this point of view the submodel 2 cannot be considered as representative of a more realistic configuration, e.g., of a vehicle hitting a rigid wall.

5.5.3. Code comparison with elastoplastic material from N1 vehicle model

For the final simulations regarding the submodel 2, the materials assigned to each part are the materials assigned in the N1 Vehicle model. All materials use the material card 024-PIECEWISE_LINEAR_PLASTICITY. The thickness of each part is the same as in the previous case of the elastoplastic

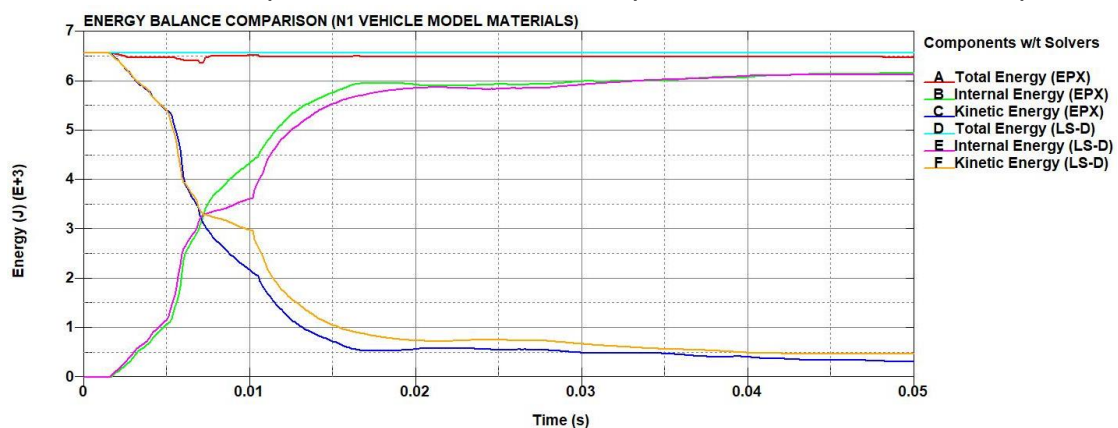


Figure 121 - Submodel 2 with materials from N1 vehicle model energy balance

comparison, but in this case all elements have a fully integrated element formulation (EL. FORM 16). The contact model is also the same as in the elastoplastic case. Impact velocity is 20 m/s. The results of the energy balance (figure 121) is very similar to the elastoplastic material. The results of the two parts noted in the elastoplastic simulation of their internal energy is also similar in this case (figures 122 and 123). Comparing the momentum of both cases (figure 124), the results of the total momentum are closer in this case, than the elastoplastic case. It is also worth mentioning that the rotation

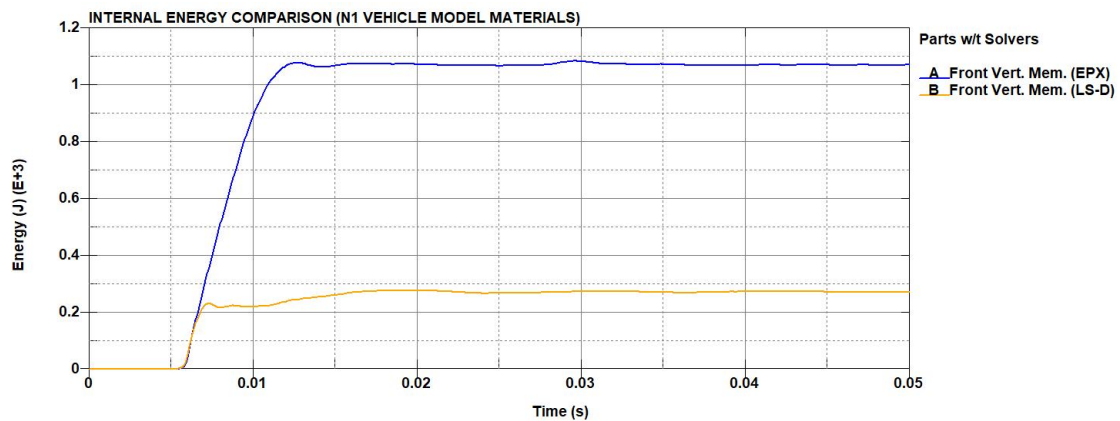


Figure 122 - Submodel 2 with materials from N1 vehicle model "Front vertical member" internal energy

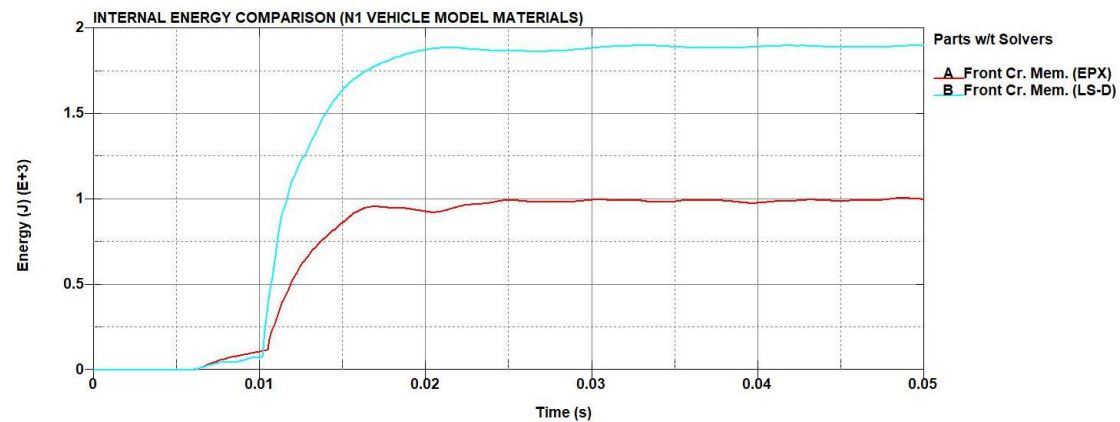


Figure 123 - Submodel 2 with materials from N1 vehicle model "Front cross member" internal energy

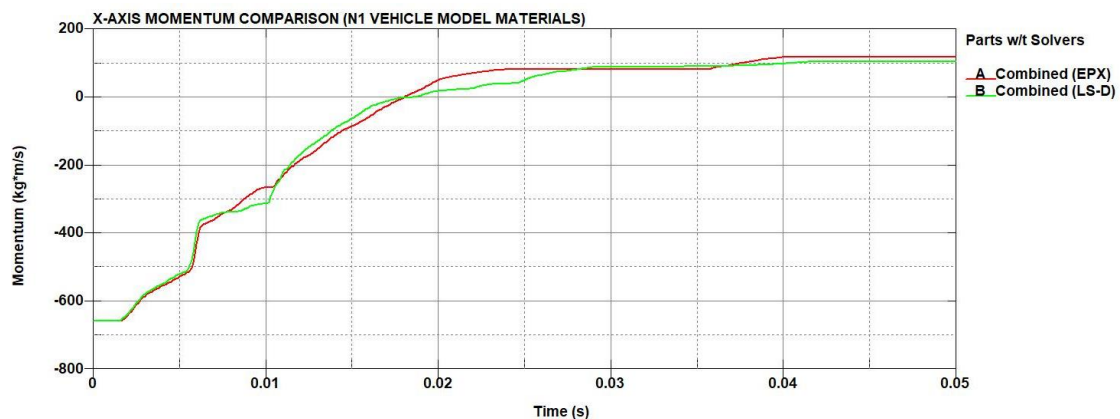


Figure 124 - Submodel 2 with materials from N1 vehicle model "Front vertical member" x-axis momentum

of the part during impact was also observed in this case. To conclude, the behaviour of the part in the case of the original materials from the NI vehicle model is close to the elastoplastic material behaviour and although the difference between the results in the last two cases can be considered as acceptable, due to the rotation of the model after impact, submodel 2 is not considered realistic for this study.

5.6. Submodel 3

The final model in the code comparison between Europlexus and LS-Dyna is a more complex variation of the submodel 2 model, called "submodel 3" (or "subassembly 3") (figure 125). This is the most complex

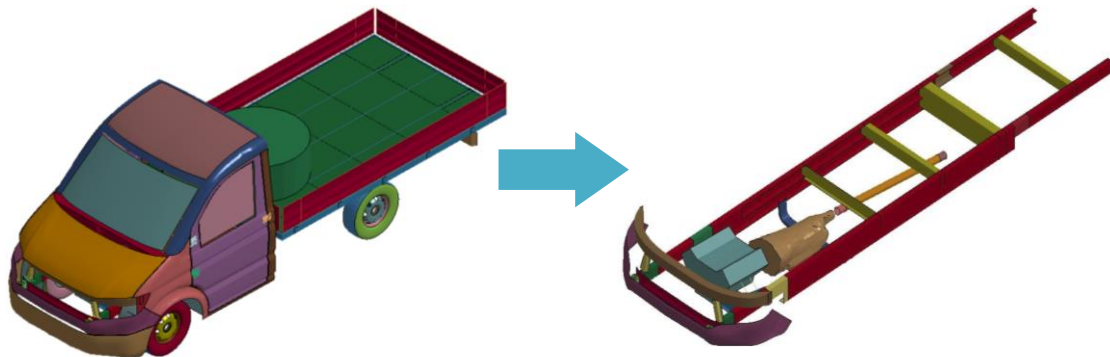


Figure 125 - Submodel 3 model extraction

model so far, with many different element types and connections included in the model. The model is also extracted as well from the first release of the NI Generic Vehicle Model, and it is comprised of 21 parts (figure 126):

- PART 1 – Frame longitudinal beams
- PART 2 – Frame front bumper under engine
- PART 3 – Frame crush zone
- PART 6 – Frame front bumper
- PART 7 – Frame cross member under engine
- PART 8 – Frame - wheel FR – rigid
- PART 9 – Frame - wheel FL – rigid
- PART 10 – Frame - wheel RR – rigid
- PART 11 – Frame - wheel RL – rigid
- PART 101 – Engine
- PART 102 – Gearbox
- PART 104 – Driving shaft
- PART 105 – Driving shaft - rigid F

- PART 106 – Driving shaft – rigid R
- PART 110 – Engine bolts
- PART 111 – Engine surface
- PART 125 – Front Vertical Member
- PART 126 – Front Cross Member
- PART 132 – Front Fascia Bottom
- PART 142 – Front Bumper Absorbing Member

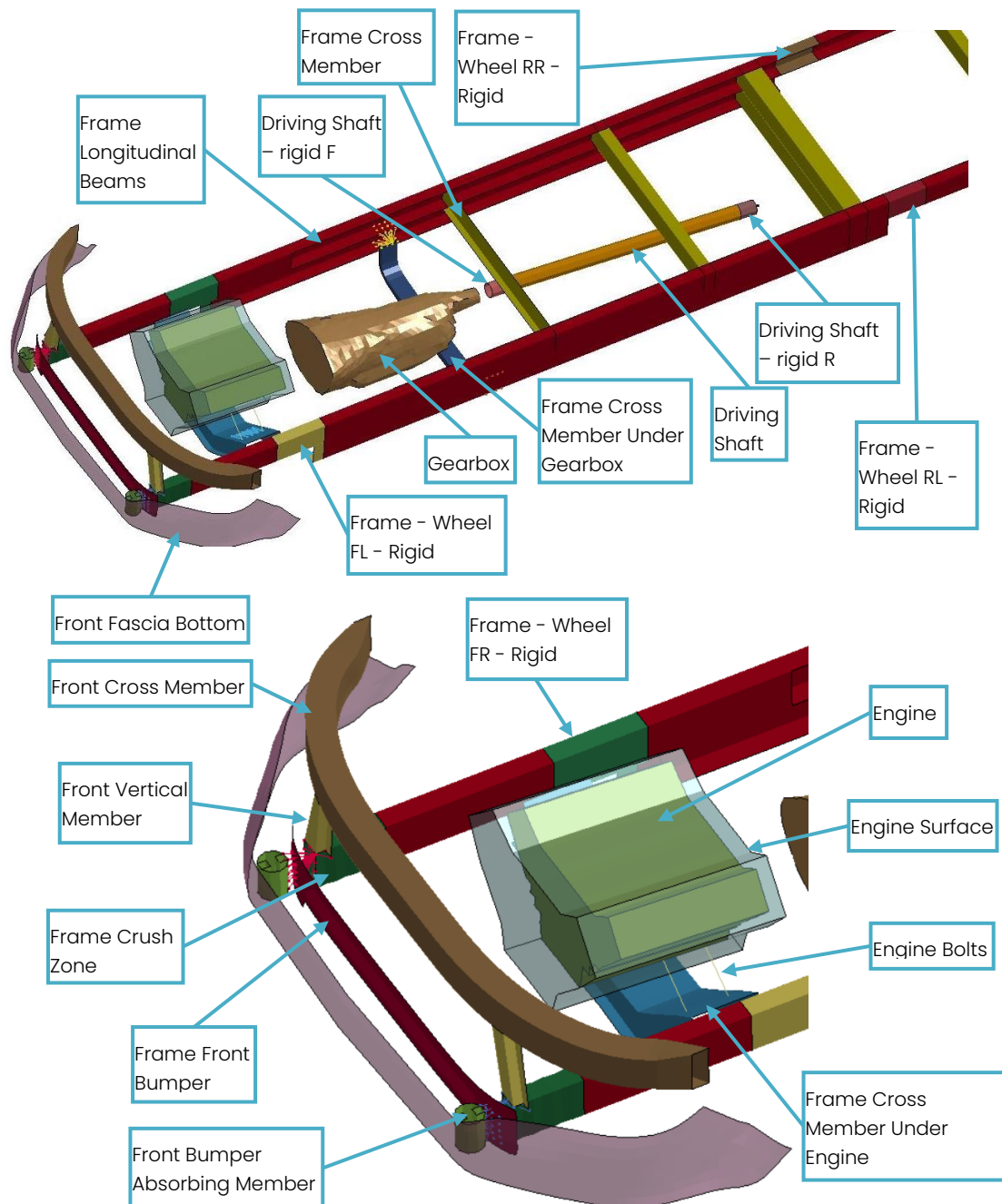


Figure 126 – Submodel 3 parts

Some of the parts are also included in the submodel 2. The parts have retained their original thickness from the NI model and have a fully integrated element formulation where possible. Thus the element formulations used are:

- Parts 101, 102 and 11 are solid elements, with element formulation EL. FORM 2: Fully integrated S/R solid.
- Part 110 is beam element, with element formulation EL. FORM 1: Hughes-Liu with cross section integration.
- All of the rest of the parts are shell elements, with element formulation EL. FORM 16: Fully integrated shell element.

The materials used for the simulation are the same from the first version of the NI vehicle model for each part. There are two types of material cards used:

- 020-RIGID, which is for the parts 8, 9, 10, 11, 101 and 102
- 024-PIECEWISE_LINEAR_PLASTICITY for all the rest of the parts

For the 024-PIECEWISE_LINEAR_PLASTICITY, there are two methods used to simulate the stress-strain curve after the yield stress point. Either by assigning the stress-strain curve by points, (here is performed by assigning the EPS and ES points from 1-8 on the material card), or by assigning a tangent modulus (ETAN) for the materials which we do not have a realistic stress-strain curve. One velocity was used for this simulation of 20 m/s. Regarding the contact model, the keywords used were AUTOMATIC_SINGLE_SURFACE and AUTOMATIC_SURFACE_TO_SURFACE. However, upon initial simulations, there were issues of the engine penetrating the barrier, and there were sudden changes in the total energy output. So, in this case the parameters used were taken from the NI Generic Vehicle Model, with the friction removed as in the Europlexus solver simulations. Through this modification, there was no penetration of the wall through the barrier and the total energy was correctly preserved throughout the simulation. The LS-Dyna solver version used for these simulations is the R12 double precision SMP.

5.6.1. Code comparison of connections from both versions of NI and JRC model

Initial simulation is performed regarding the connections in the submodel 3. There are small differences between the connections used in the model of Politecnico di Torino (which replicated the ones used in the NI vehicle model) and the model used by JRC. The connections for both models are:

- CNRBs:
 - Used in various places in the model
 - The connections are the same in both models
- Spotwelds:
 - Spotwelds are assigned on the NI Vehicle model between “Front fascia bottom” (part 132) and “Front bumper absorbing member” (part 142).
 - Spotwelds were not active on the JRC model, so they were deleted for that version of the model.
- Connection between gearbox and drive axle (figure 127):
 - The connection between gearbox and drive axle is performed with a spherical joint on the NI Vehicle model and the keyword used is `CONSTRAINED_JOINT_SPHERICAL`.
 - The connection between gearbox and drive axle is performed with a rigid connection on the JRC model and the keyword used is `CONSTRAINED_RIGID_BODIES`.

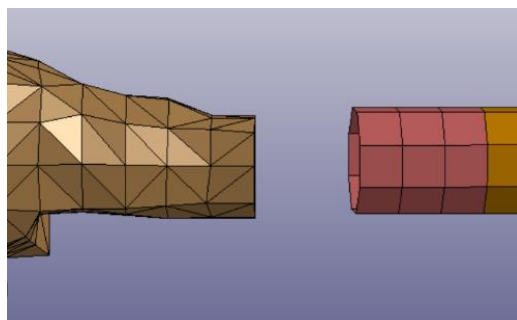


Figure 127 - Connection between gearbox and drive axle

- Drive axle:
 - In the JRC model there is a rigid connection with all the parts of the drive axle (parts 105 - 104 - 106).

- The keyword used for this model is `CONSTRAINED_RIGID_BODIES` between parts 105 and 106 (cannot be used with non rigid parts, such as 104).
- Engine – Gearbox:
 - Rigid connection between engine and gearbox on both models
 - Connection between engine and gearbox is assigned via `CONSTRAINED_RIGID_BODIES`.
- Cross member under engine – frame (figure 128):
 - Rigid connection between node set on edge of “Cross member under engine” (part 2) with rigid parts on the frame (parts 8 and 9) on both models.
 - Connection between engine and gearbox is assigned via `CONSTRAINED_EXTRA_NODES_SET`.

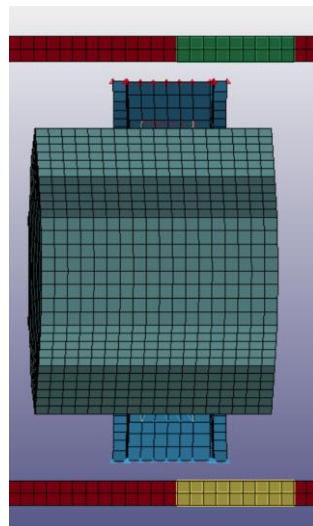


Figure 128 - Connection between gearbox and drive axle

The version of the connections according to LS-Dyna is indicated as LS-D_V1 and the version of the connections according to JRC model is indicated as

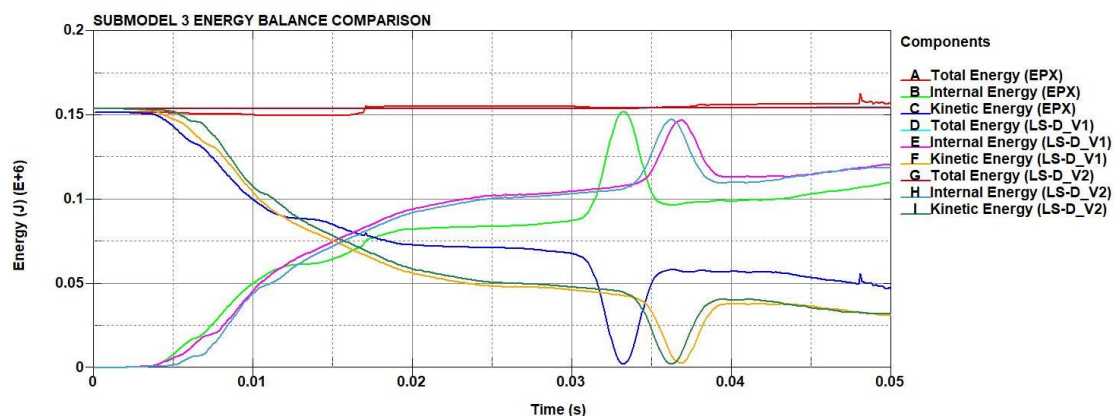


Figure 129 - Submodel 3 energy balance

LS-D_V2. Examining the energy balance (figure 129), the internal energy of the Europlexus simulations is lower than the LS-Dyna simulations after 0.0125 s, thus the submodel in LS-Dyna has dissipated less energy. The peak of the internal energy is at the point where the engine comes in contact with the barrier. This peak occurs at a different time instant for both solvers, but it has a higher value in Europlexus (figure 130). The total energy in the LS-Dyna simulations is much more stable than Europlexus (figure 131). There were also noticeable differences in the part “Engine bolts” regarding its internal energy,

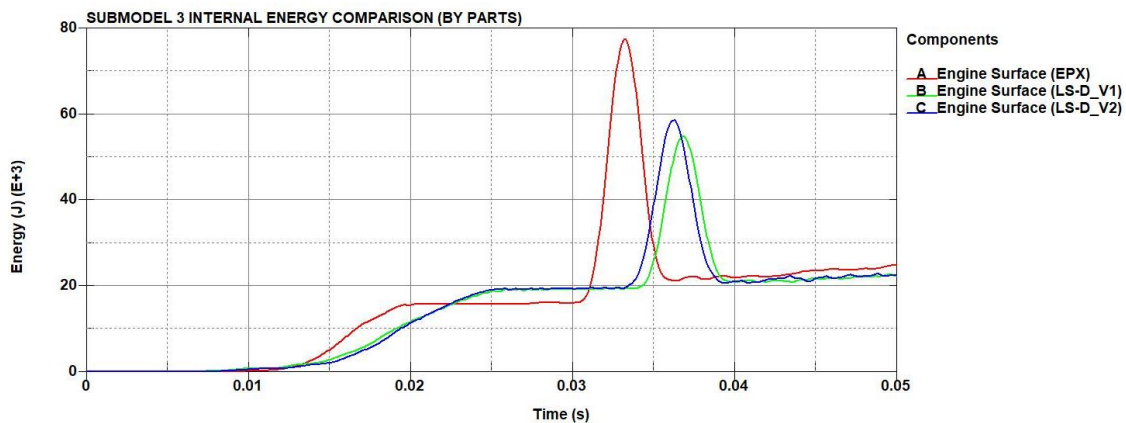


Figure 130 - Submodel 3 “Engine surface” internal energy

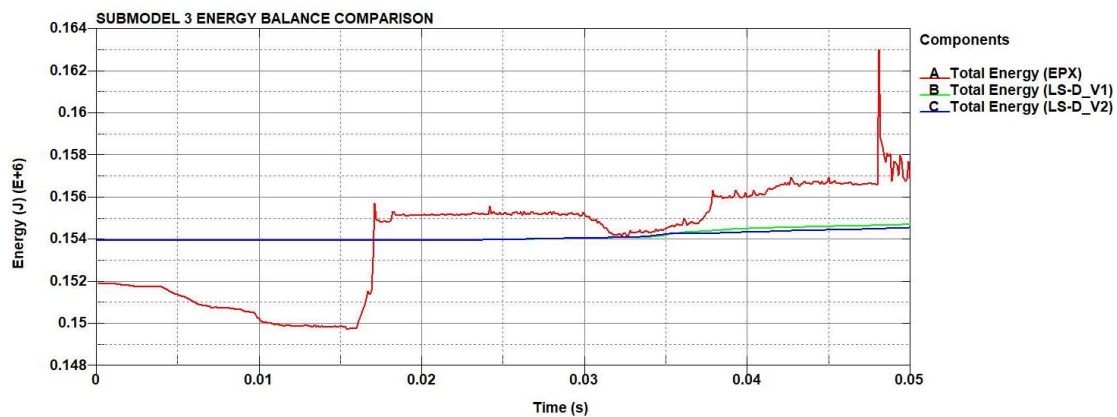


Figure 131 - Submodel 3 total energy

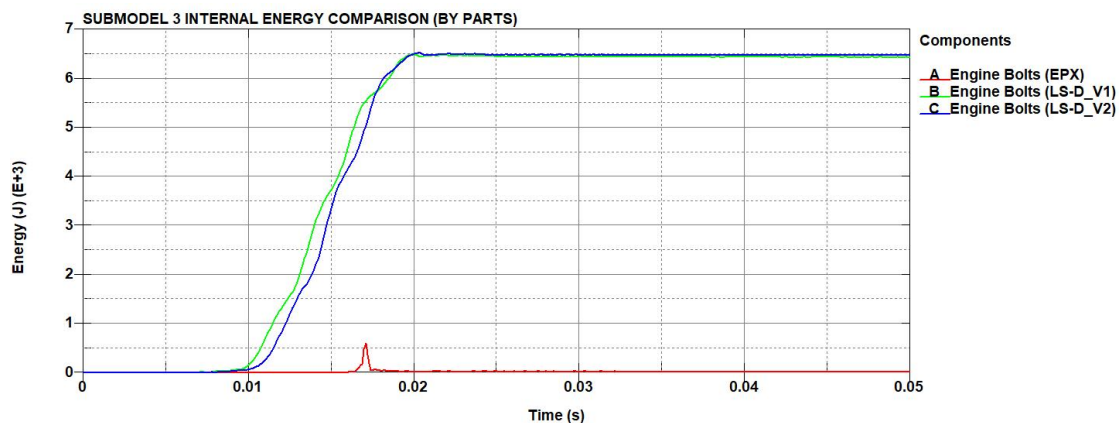


Figure 132 - Submodel 3 “Engine bolts” internal energy

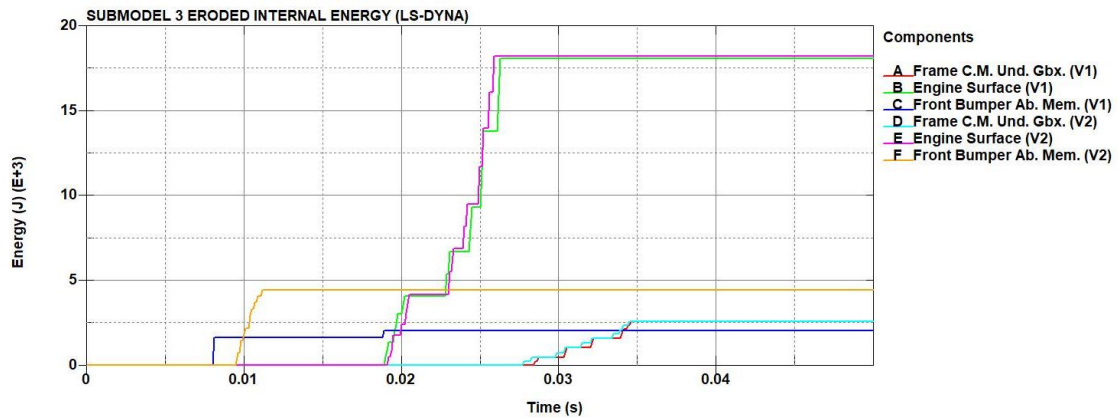


Figure 133 - Submodel 3 internal eroded energy

where in Europlexus it does not absorb any energy, contrary to LS-Dyna, where there is an absorption of energy (figure 132). The model displayed eroded internal energy in some parts (figure 133). The results between the two versions are almost identical, apart from the “Front bumper absorbing member”, where there is a higher eroded energy in the second version of the model, where the spotwelds were not present between the parts “Front fascia bottom” and “Front bumper absorbing member”. From the contact force (figure 134) and momentum (figure 135) graphs, there are also some

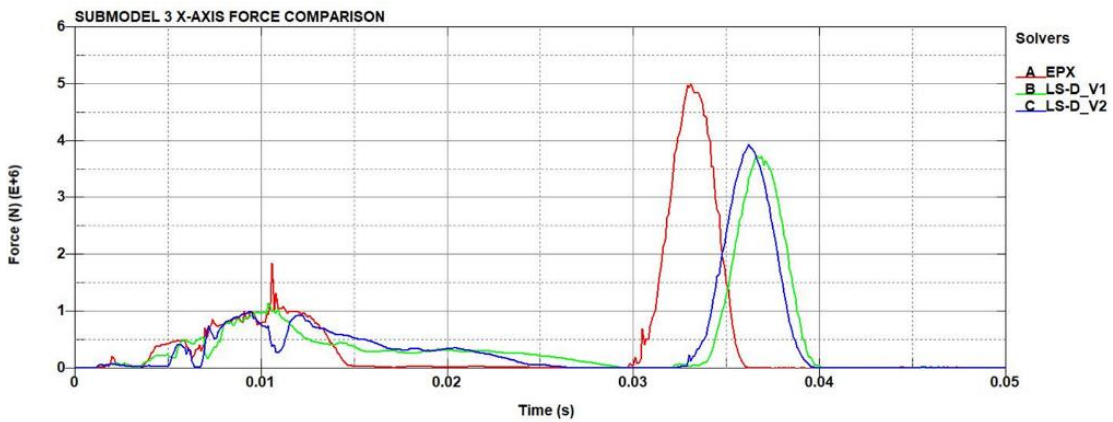


Figure 134 - Submodel 3 x-axis contact force

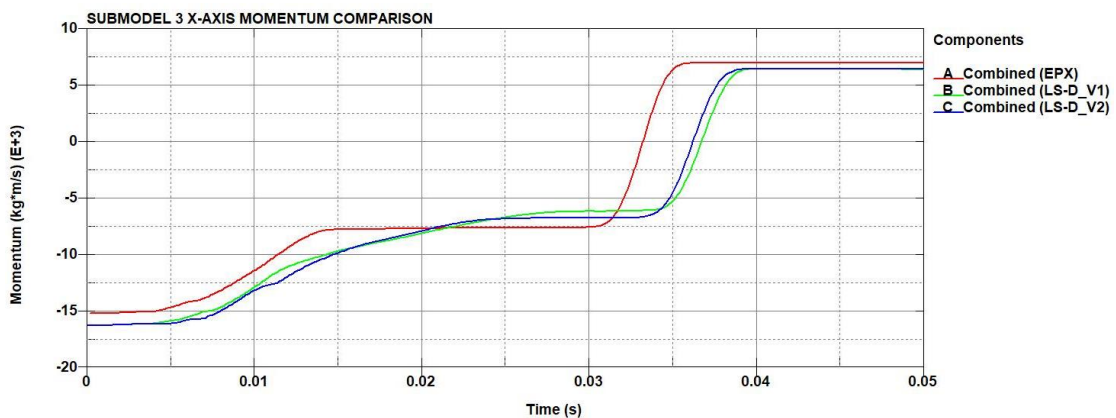


Figure 135 - Submodel 3 x-axis momentum

noticeable differences between the two solvers. The results between the two versions of the model in the LS-Dyna solver are very similar, also in terms of contact force and total momentum. Thus the difference lies between the code of the two solvers. From the submodel 2 simulations it is deduced that Europlexus cannot reproduce the rigid constraints exactly like LS-Dyna. In Europlexus, a part or a set of points can only be rigid by blocking translations and rotations, whereas in LS-Dyna rigid bodies can rotate freely. For the vehicle model, the rigid constraints on NSETs 7 & 8 have an important role, since they connect three crash absorbing parts (parts 3,6 and 142) (figure 136). Initial testing from the JRC was to check the effect on blocking rotations

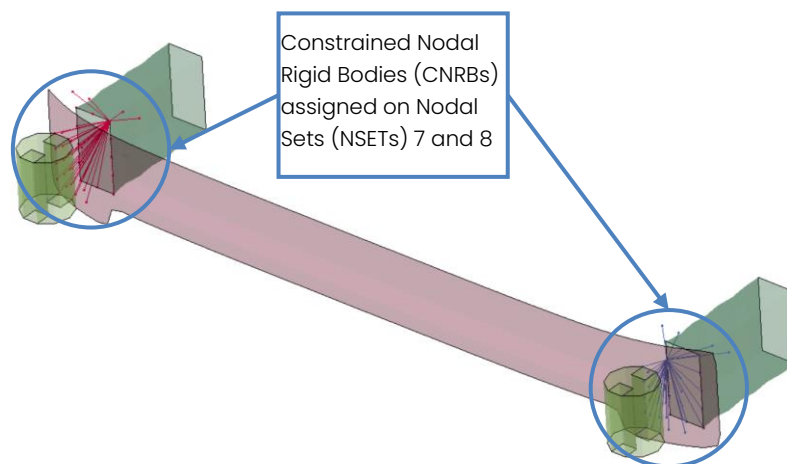


Figure 136 - Parts connected by the constraint nodal rigid bodies (CNRBs) defined by the nodal set (NSET) 7 and 8

through post-processing reaction forces, but without a useful output. The next step was to change the rigid constraint from blocking all directions (X, Y and Z) to blocking only the main (X) direction and leaving the other two free. This is not realistic, however an effect of changing the rigid condition is visible. In the figure 137, the internal energy evolution for three of the most affected parts is shown, with varying assumptions on constraints and with different meshes (in the refined line indicated on the figure, there are 4 times more elements only of the PART 142). What is observed is that, by changing the mesh and/or the rigid constraint assumption, the crashing behaviour of these parts is quite different. In this stage, it is too hazardous to explain these results rationally since the crashing behaviour of the structure seems far from trivial. In conclusion, it makes no sense continuing the comparisons

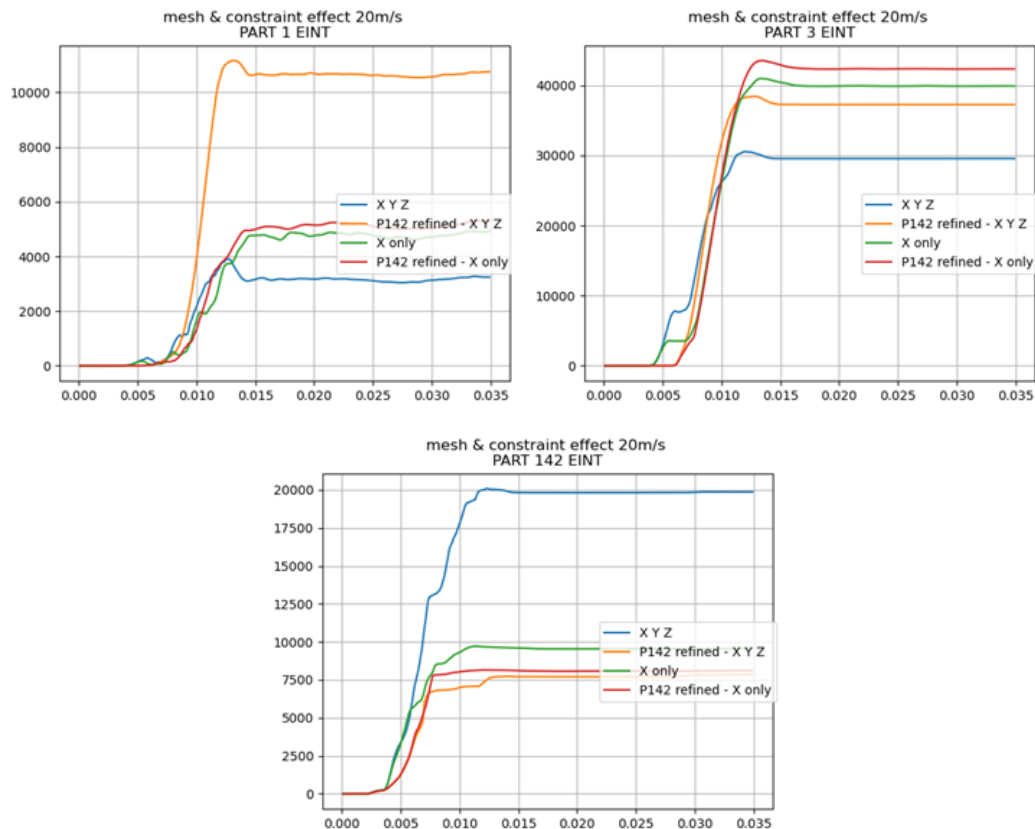


Figure 137 – Submodel 3 internal energy time evolution of parts “Frame longitudinal beams” (part 1), “Frame crush zone” (part 3) and “Front bumper absorbing member” (part 142)

between Europlexus and LS-Dyna in the submodel 3, until the rigid constraints are simulated properly in Europlexus.

5.6.2. Submodel 3 Frame mesh sensitivity analysis

In the next steps, a small case study is considered regarding the frame of the submodel 3, in order to check for the sensitivity of the results on the mesh size and type. The model is comprised from the following parts of the submodel 3:

- PART 1 – Frame longitudinal beams
- PART 3 – Frame crush zone
- PART 8 – Frame - wheel FR – rigid

Since the frame is symmetrical, only one of the two longitudinal members with its parts, is considered. The same materials and part thicknesses as in the submodel 3 were used (i.e., from the NI model), with a change in density in the material of part 8 at a value of $30 \cdot 10^4 \text{ kg/m}^3$, as proposed by JRC, to have more mass in the system, in order to simulate a more realistic

behaviour. All elements are in fully integrated formulation (EL. FORM 16). The initial velocity is 20 m/s. The contact model used is the AUTOMATIC_SURFACE_TO_SURFACE and AUTOMATIC_SINGLE_SURFACE with no friction assigned to the part and with the same parameters as the previous simulations (except from the submodel 3, where the parameters assigned were from the NI Vehicle model). The LS-Dyna solver version used for these simulations is the R12 double precision SMP.

5.6.2.1. Quadrilateral vs Triangular element comparison on frame

The first comparison is a comparison between quadrilateral (Q4) versus triangular (T3) elements. Only the “Frame crush zone” is changed

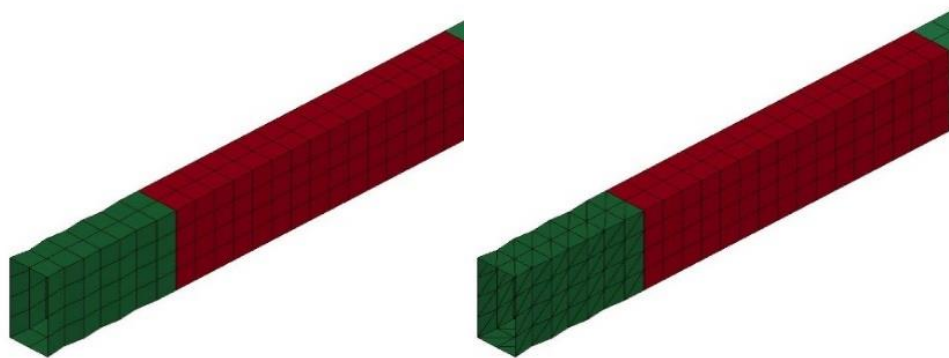


Figure 138 - Frame quadrilateral element case (left) and triangular element case (right)

between quadrilateral and triangular elements in the two cases (figure 138). From the energy results, the total energy is more stable in LS-Dyna than Europlexus (figure 139). Also, the internal energy results are affected by the element type (figure 140), which is not good for the overall accuracy of the

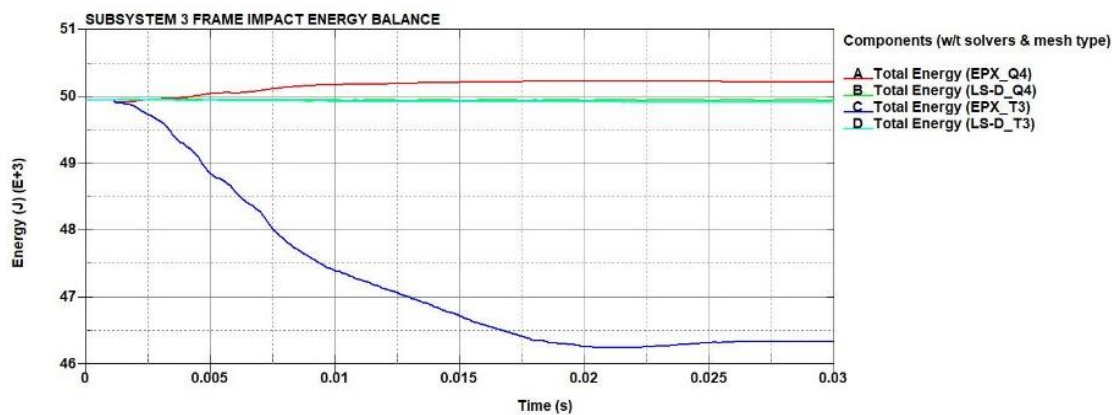


Figure 139 - Frame quadrilateral vs triangular elements total energy



Figure 140 - Frame quadrilateral vs triangular elements internal energy

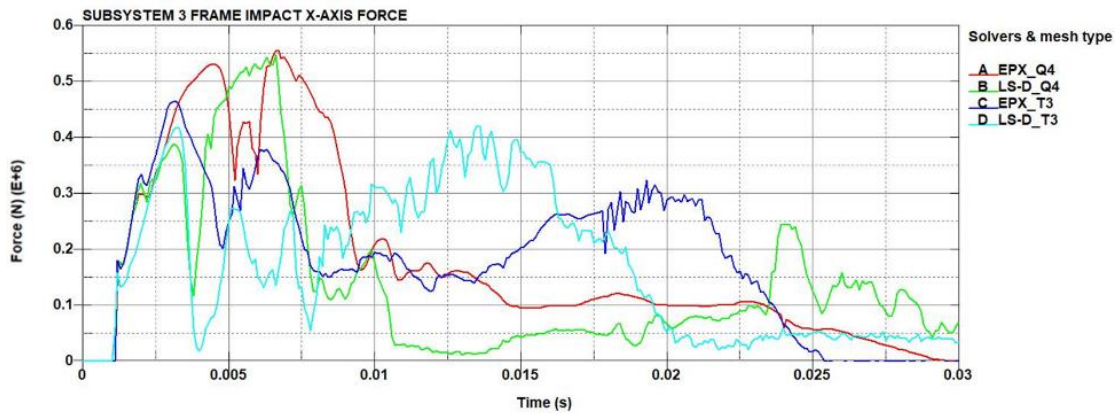


Figure 141 - Submodel 3 frame quadrilateral vs triangular elements x-axis contact force

current vehicle model, since in the full simulation the frame which absorbs most energy and has a fundamental role in the impact. As in previous cases, the momentum graph is the preferred method of estimating the contact force since the contact force output is affected by noise due to high frequency components (figure 141). However, differences between the two element types are also visible in the momentum graph (figure 142). From the effective plastic strain (figures 143 and 144), even if the initial mesh is composed exclusively of quadrilateral shell elements, in some places the structure is deforming as there were triangular elements. Many of the

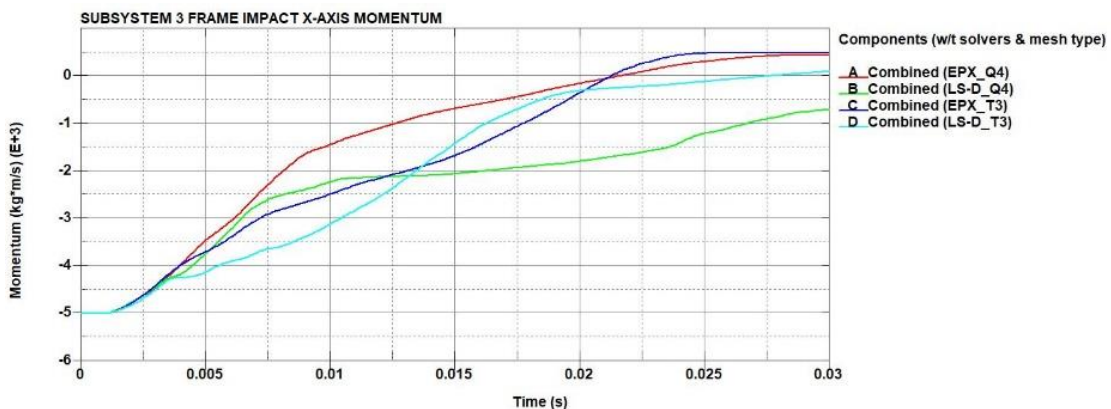


Figure 142 - Frame quadrilateral vs triangular elements x-axis momentum

quadrilateral elements are subject to a strong out-of-plane bending. It is important to note that the basic quadrilateral shell formulation requires the nodes to be coplanar. As the node coordinates are updated with the deformation (node displacements), the coplanarity is no longer guaranteed. From the LS-Dyna effective plastic strain figures, the elements do not remain completely coplanar, but also that the out-of-plane distortions are very limited. Because triangular elements remain coplanar by definition, the case of replacing the quadrilateral elements of the part “Frame crush zone” with triangular elements was proposed. With the modified mesh, the results are different from the quadrilateral case, but the behaviour is similar between Europlexus and LS-Dyna.

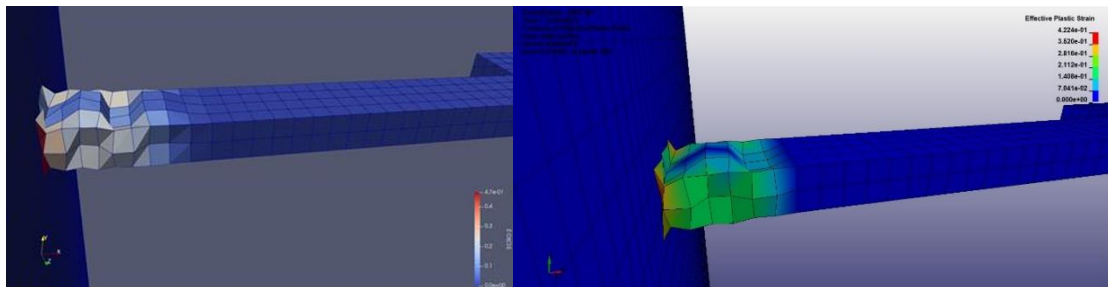


Figure 143 - Frame quadrilateral vs triangular elements effective plastic strain of quadrilateral elements of Europlexus (left) and LS-Dyna (right)

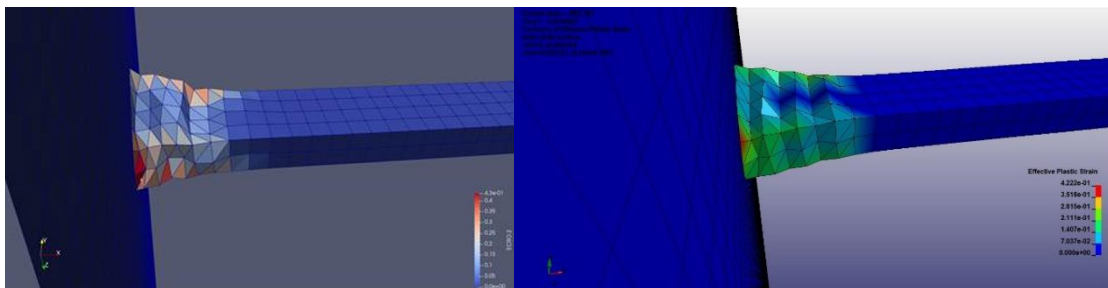


Figure 144 - Frame quadrilateral vs triangular elements effective plastic strain of triangular elements of Europlexus (left) and LS-Dyna (right)

5.6.2.2. Quadrilateral vs Triangular element comparison on example from Dynaexamples

In the scope of confirming the difference between the different element types, a case of a simple tube is considered according to the example “Crashbox” from Dynaexamples [10]. In this case, a tube of 100 mm x 100 mm x 270 mm, with element size of 5 mm is considered for both element types (figures 145 and 146). Shell elements are considered with fully integrated element formulation. The material used is the same as in the

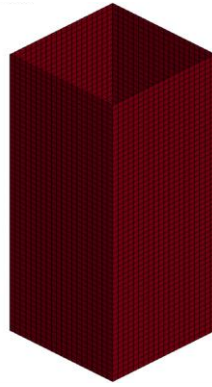


Figure 145 - Simple tube

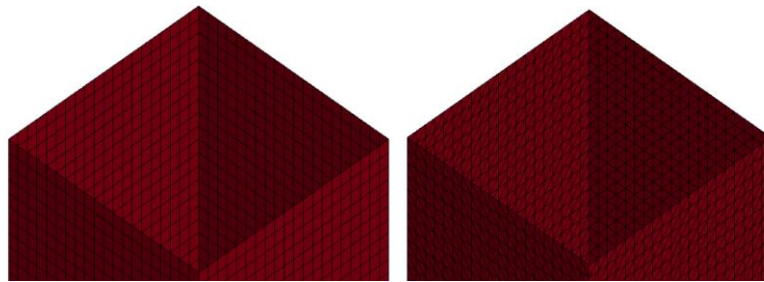


Figure 146 - Quadrilateral (left) and Triangular (right) element case

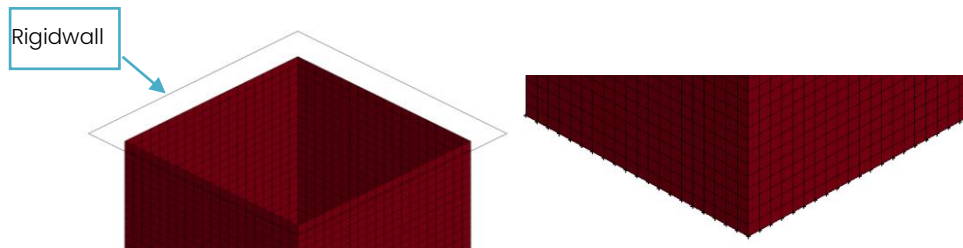


Figure 147 - Rigidwall (left) and DOF constraints (right)

Frame crush zone in the NI vehicle model. The experiment is performed with a rigid wall, of 800 kg and initial velocity of 8.94 mm/ms, which is crushing the square tube, who is constrained at the bottom nodes on all DOFs (figure 147). The LS-Dyna solver version used in this case, is the R11.2 double precision SMP. From the energy results, it is visible that the triangular elements dissipate more energy than the quadrilateral elements (figures 148 and 149).

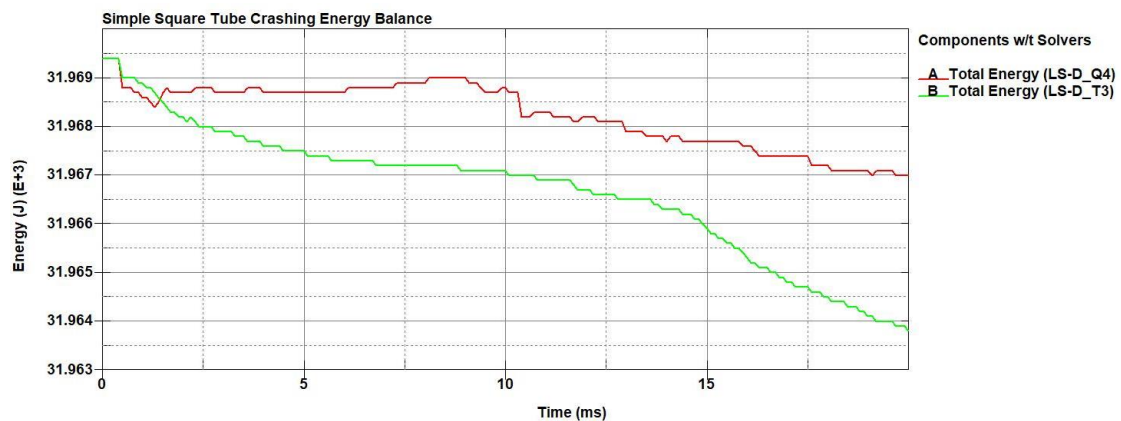


Figure 148 - Simple tube example total energy



Figure 149 – Simple tube example internal energy

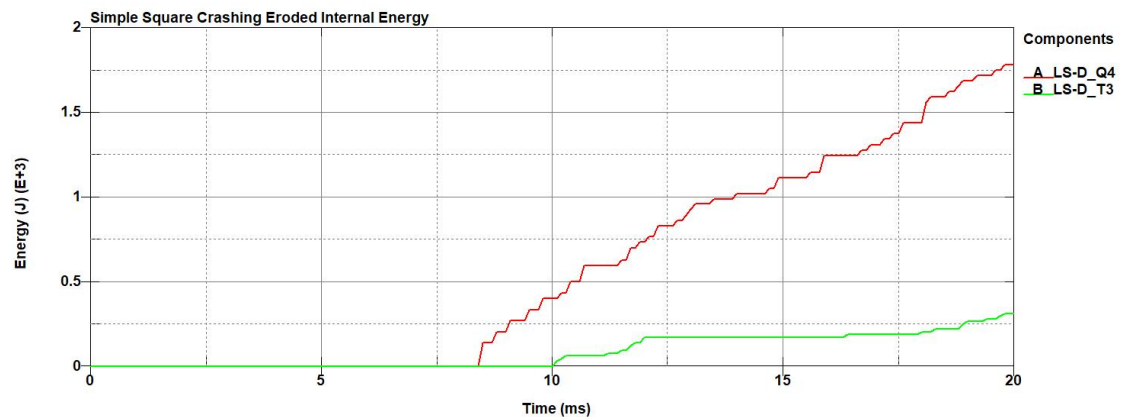


Figure 150 – Simple tube example eroded energy

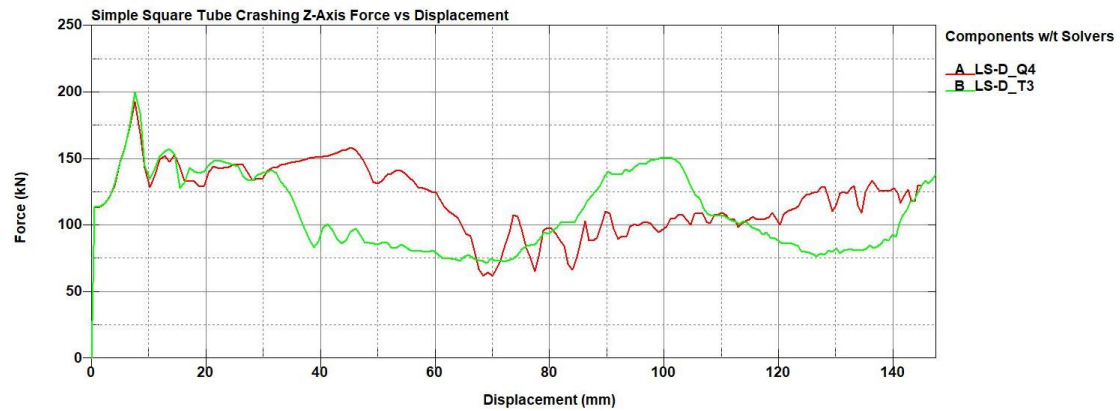


Figure 151 – Simple tube example force vs displacement graph

Also there is a difference in the eroded energy, where the triangular elements display less eroded internal energy (figure 150). The difference between the two element types are also apparent in the force vs displacement graph (figure 151) where the different element types display different behaviour, thus confirming the results from the previous comparison.

5.6.2.3. Quadrilateral vs Triangular elements comparison on frame mesh refining

Returning to the submodel 3 frame case, the next step in the comparison is to perform a mesh size sensitivity analysis on the model. The remeshing is performed on the whole model. Three mesh sizes are considered:

- Original mesh (avg. element size: 30 mm)
- Fine, with element size half of the original mesh (avg. element size: 15mm)
- Very fine, with element size half of the fine mesh (avg. element size: 7.5mm)

The mesh types are considered for both quadrilateral and triangular elements, thus having six different configurations (figure 152). As before the triangular elements are only applied on the “Frame crush zone” part. All the

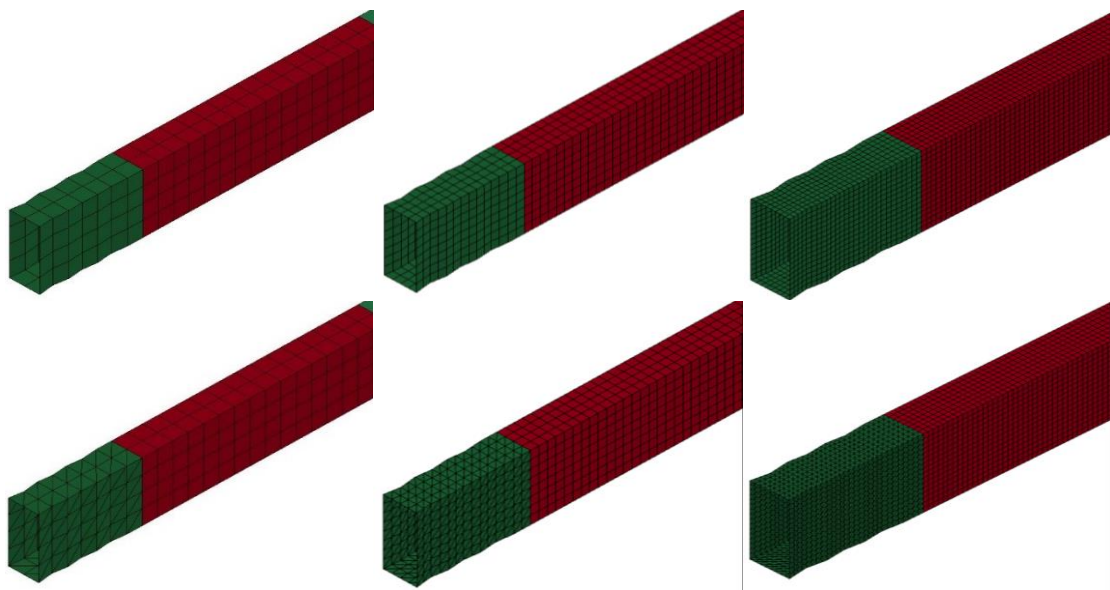


Figure 152 - Frame mesh refinement cases of quadrilateral (top) and triangular (bottom) elements of original (left), fine (middle) and very fine mesh (right)

parameters of the simulations are the same from the original comparison of Q4 vs T3 element types. The simulations, in this case, are performed using the R11.2 double precision SMP version of LS-Dyna. The cases in the following graphs are denoted as such:

- Quadrilateral original mesh: Q4
- Quadrilateral fine: Q4_REFINED
- Quadrilateral very fine: Q4_DOUBLE_REFINED

- Triangle original mesh: T3
- Triangle fine: T3_REFINED
- Triangle very fine: T3_DOUBLE_REFINED

From the internal energy results (figure 153), comparing quadrilateral vs triangular elements at each level of refinement it is observed that as the mesh size decreases, the results between the two solvers get closer together. More consistent results are obtained from the quadrilateral elements, as a difference in the internal energy is observed, for the triangular elements in the fine mesh, between the two solvers at 0.025 seconds and in the finer

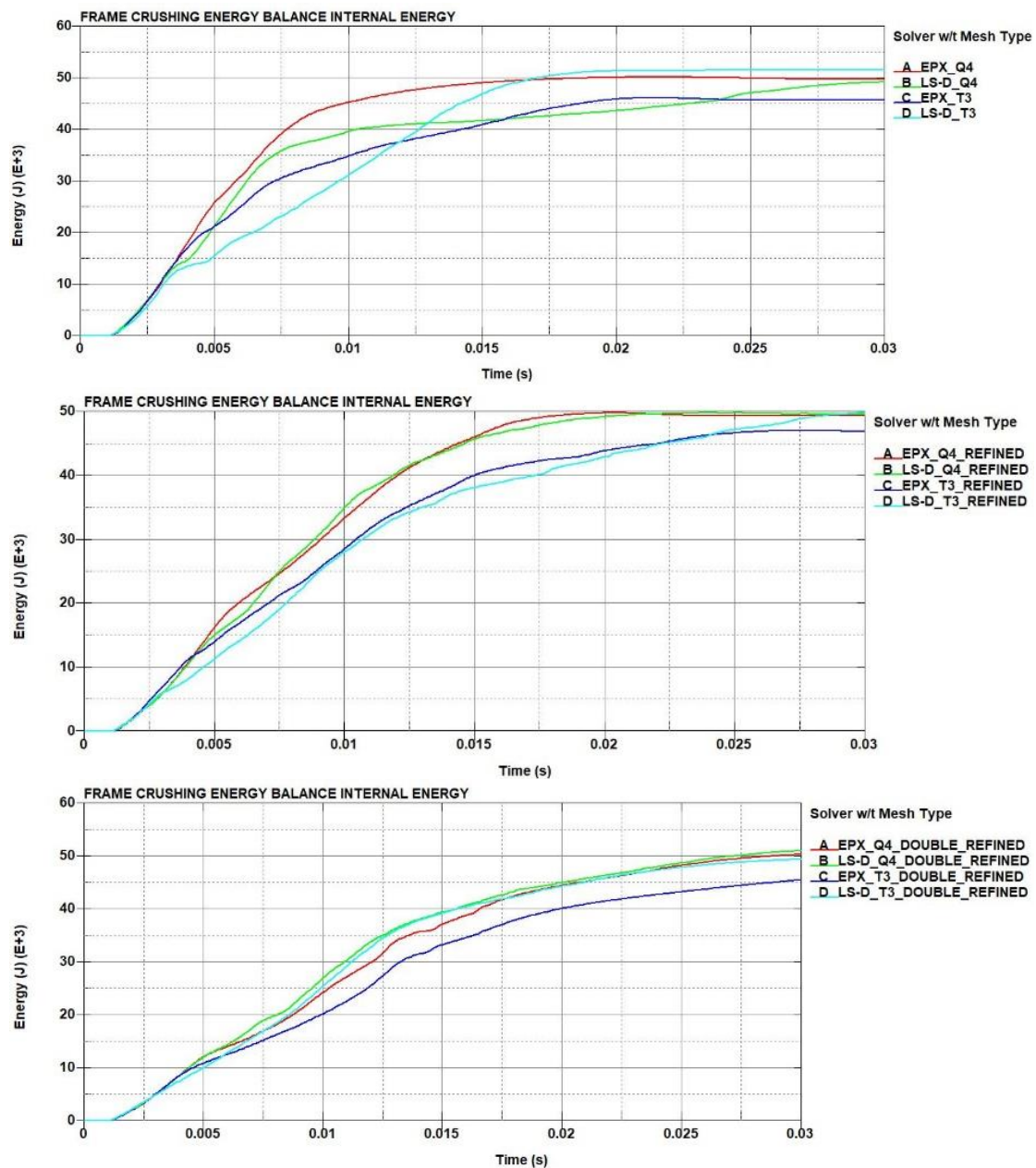


Figure 153 - Frame mesh refinement internal energy of original model (top), fine mesh (middle) and finer mesh (bottom)

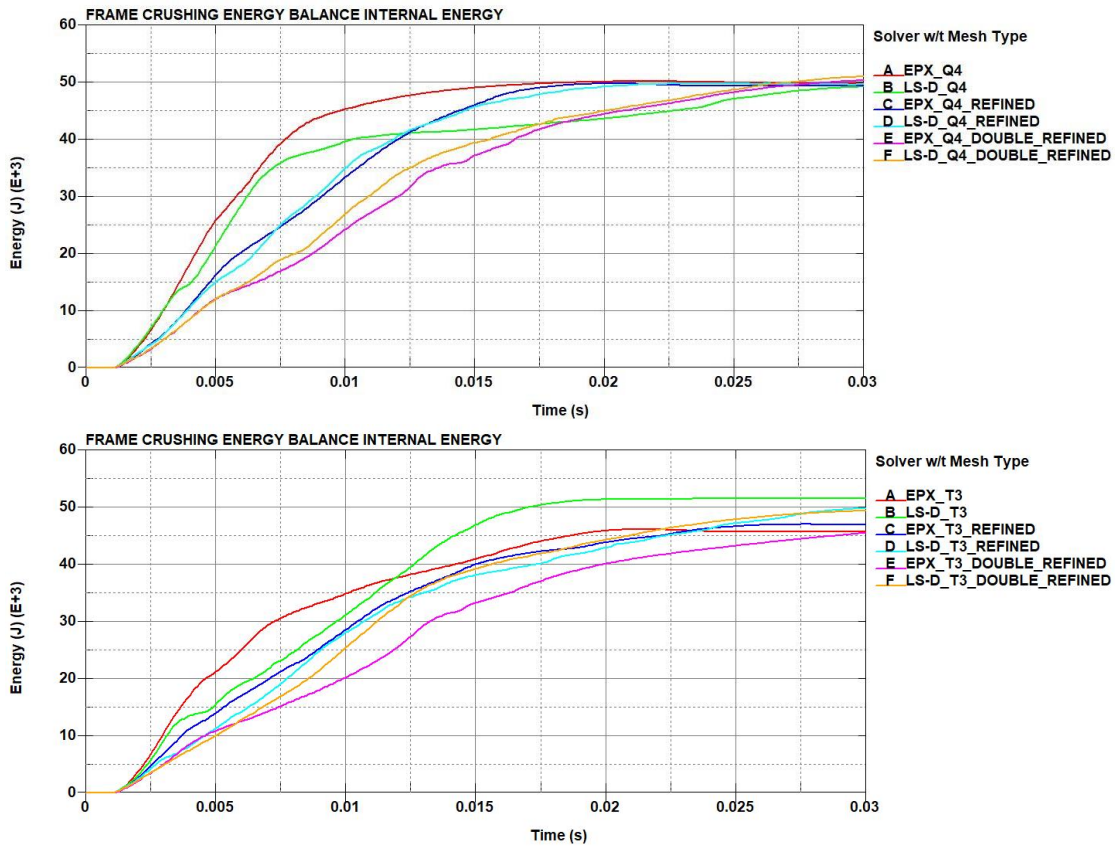


Figure 154 - Frame mesh refinement internal energy of quadrilateral (top) and triangular (bottom) elements

mesh, the results from the LS-Dyna being closer to the quadrilateral elements. If the above results are compared for all mesh sizes separately according to their type (figure 154), more consistent results can be obtained in the quadrilateral element compared to the triangular elements, where the convergence is more easily obtained with the quadrilateral elements. The total energy results (figure 155) are much more stable in the LS-Dyna solver compared to the Europlexus. It is worth noting that in the triangular elements, the LS-Dyna output of the finer version of the mesh is affected by a sliding energy component. However, the results are more stable than Europlexus.

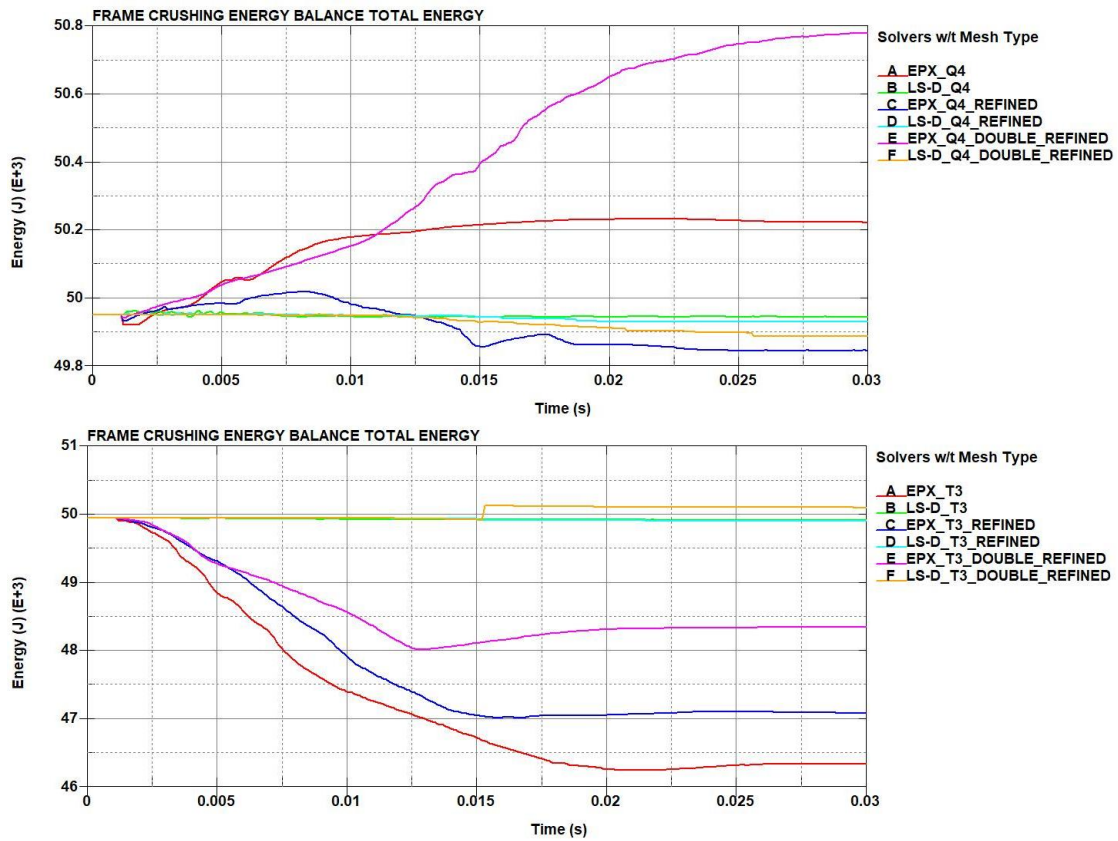


Figure 155 - Frame mesh refinement total energy of quadrilateral (top) and triangular (bottom) elements

The contact force outputs (figure 156), in this case as well, are affected by high frequency components, so they cannot be considered as a suitable method to calculate the contact force. It is worth mentioning that as the mesh size decreases, the output results follow a specific trend. Thus, the momentum graphs (figure 157) are more eligible to be used to measure the contact force.

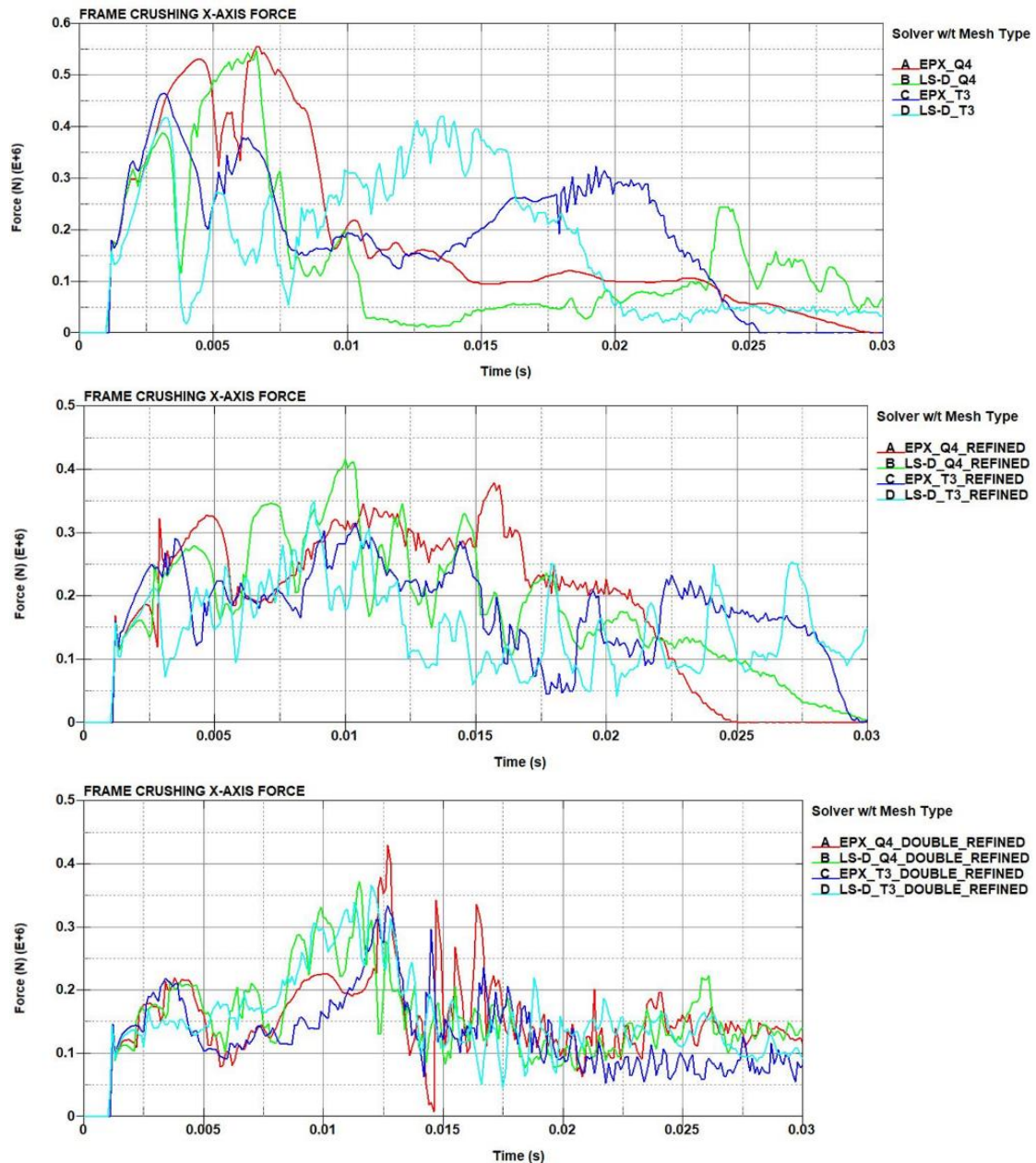


Figure 156 - Frame mesh refinement x-axis contact force of original model (top), fine mesh (middle) and finer mesh (bottom)

Overall, in the quadrilateral case, the results are closer together in the refined cases than the original mesh. This is not the case with the triangular elements where the results are different between cases. However, the termination time of 0.03 s is small time to access the convergence, since the convergence becomes slower as the mesh size decreases.

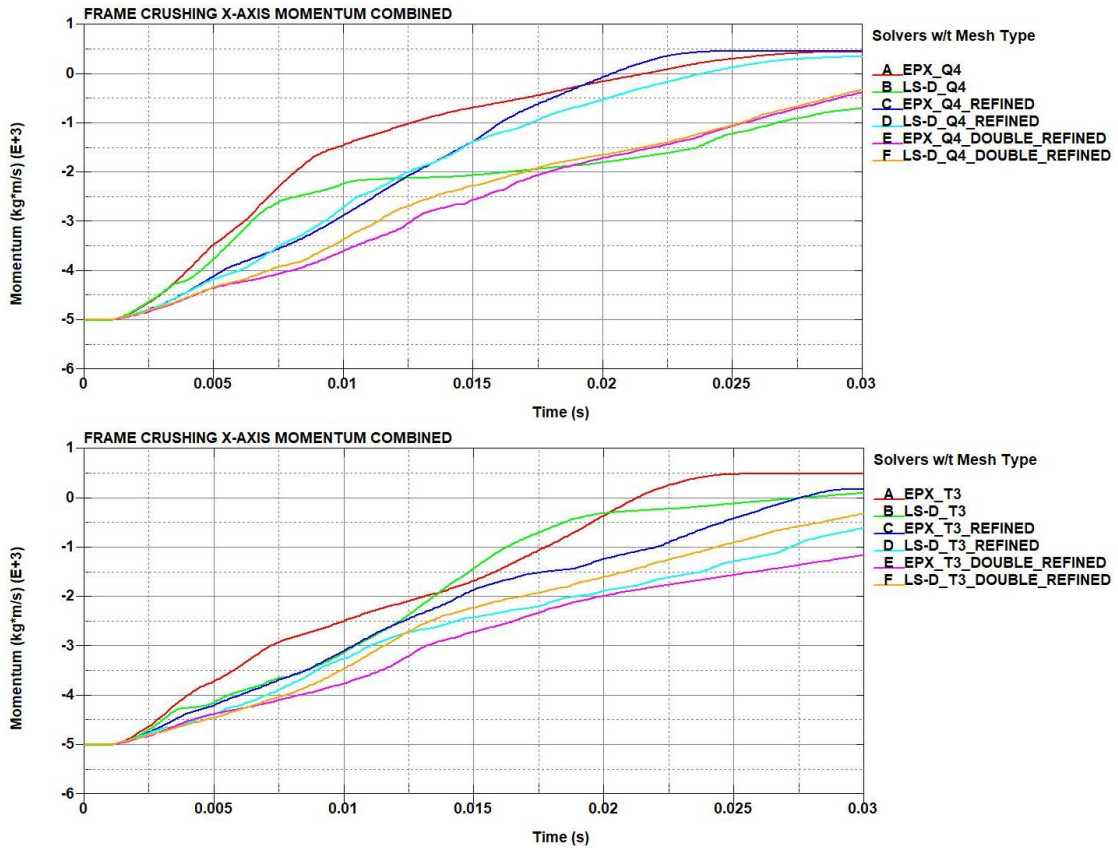


Figure 157 - Frame mesh refinement x-axis momentum of quadrilateral (top) and triangular (bottom) elements

Comparing the crushing behaviour of the frame at 5 ms, the behaviour of the quadrilateral elements between Europlexus and LS-Dyna is very similar (figures 158 and 159). Contrary to the triangular elements, where the behaviour of the model in the impact between the two solvers differs slightly in the coarse mesh case, and the difference being more obvious in the refined versions.

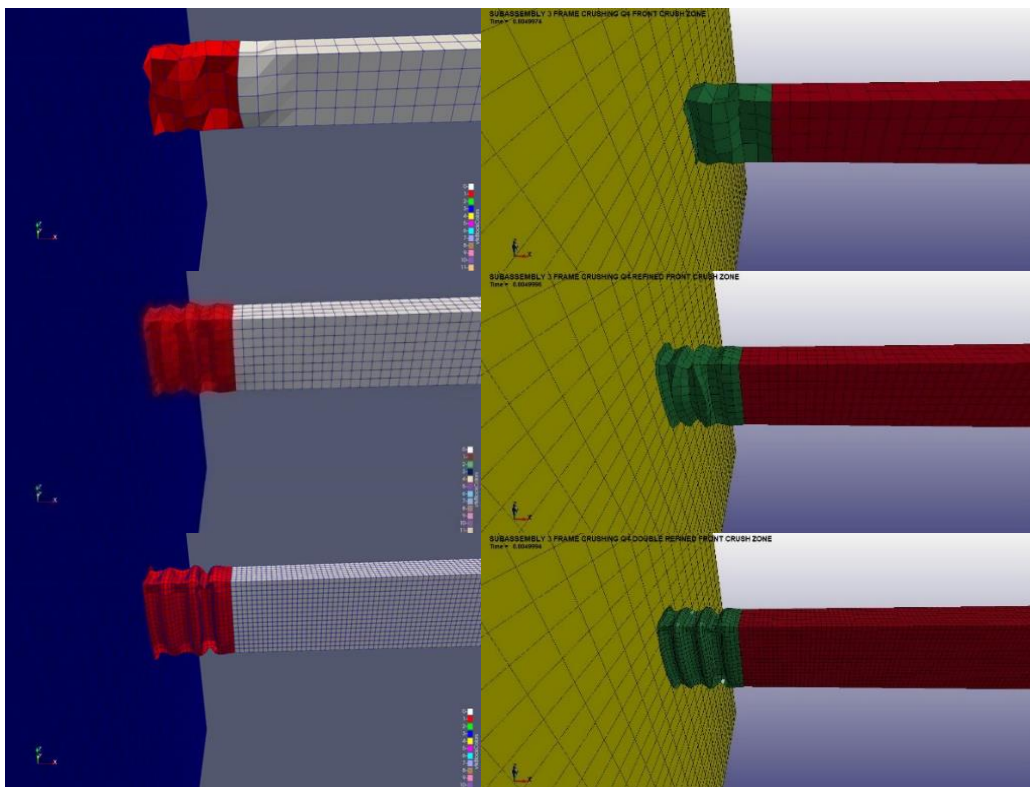


Figure 158 – Frame mesh refinement crushing behaviour @ 5 ms of quadrilateral elements case of Europlexus (left) and LS-Dyna (right) of original mesh (top), fine mesh (middle) and very fine mesh (bottom)

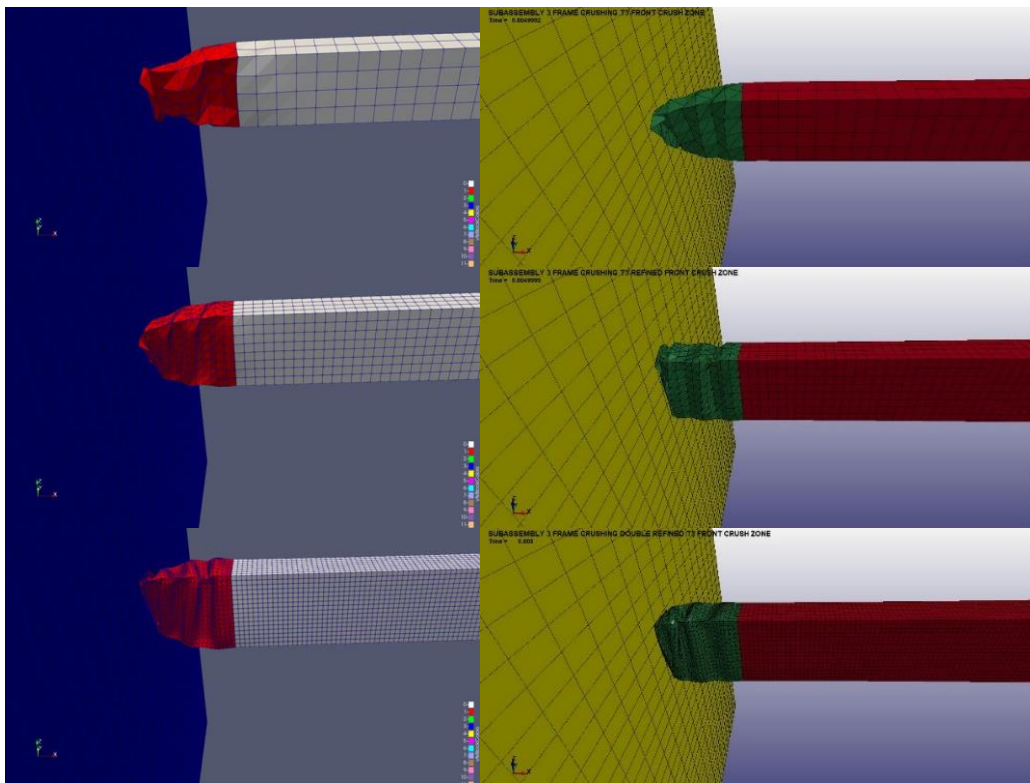


Figure 159 – Frame mesh refinement crushing behaviour @ 5 ms of triangular elements case of Europlexus (left) and LS-Dyna (right) of original mesh (top), fine mesh (middle) and very fine mesh (bottom)

5.6.2.4. Quadrilateral vs Triangular elements comparison on frame mesh refining control card effect

To verify the convergence of the results, the termination time has been increased to 50 ms. In the previous simulations of frame remeshing the CONTROL_SHELL keyword was used from the NI generic vehicle model. The option to be noted is the option ESORT, which is the only parameter changed by SVS FEM to the option 2, which is the “full sorting (DKT triangular shells)”. The rest of the parameters are assigned from default by the LS-Prepost software, as in the NI generic vehicle model. The ESORT option allows to switch from quadrilateral to triangular when the quadrilaterals become degenerated (i.e., very deformed). In this situation, it would concern only the “Frame longitudinal beams” (Part 1), which remains meshed with quadrilateral elements, while the “Frame crush zone” (Part 3) which is the main crushed part, is already in triangular elements. The simulations are performed, in this case, using the R11.2 double precision SMP version of LS-Dyna and are denoted by the previous denomination of quadrilateral (Q4) and triangular (T3), with the addition of:

- Primary: with the CONTROL_SHELL keyword
- Secondary: without the CONTROL_SHELL keyword

The comparison is performed only on the results from LS-Dyna. From the internal and total energy (figures 160 and 161), it is observed that only the results from the triangular elements are affected by the keyword. The cases with the quadrilateral elements on the “Frame crush zone” display the same results with and without the keyword.

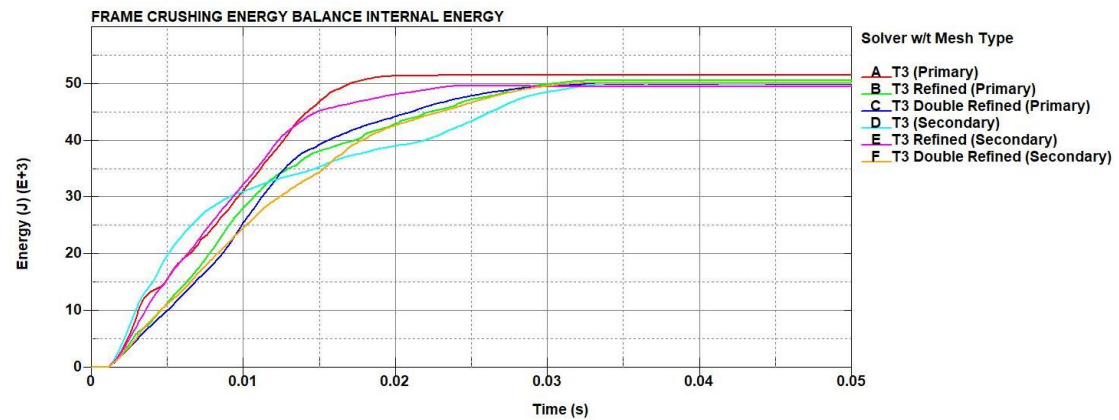
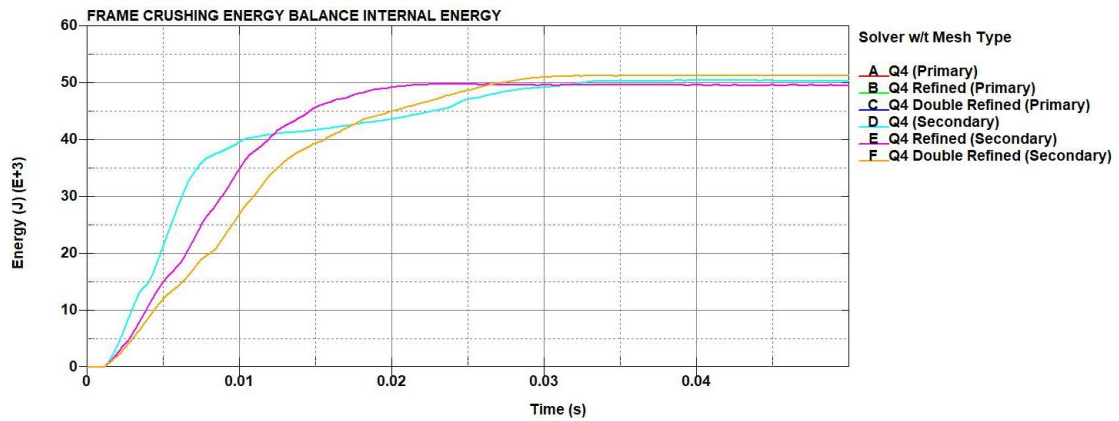


Figure 160 - Frame mesh refinement (*CONTROL_SHELL* influence) internal energy of quadrilateral (top) and triangular (bottom) elements

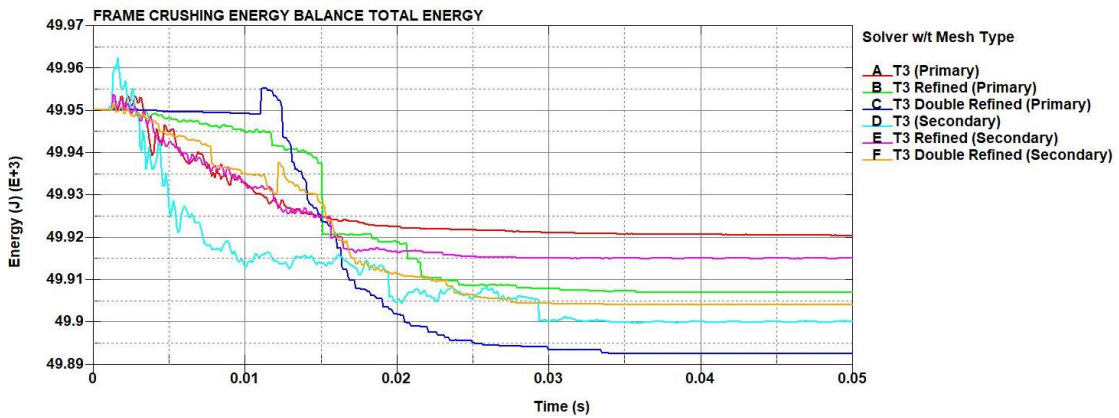
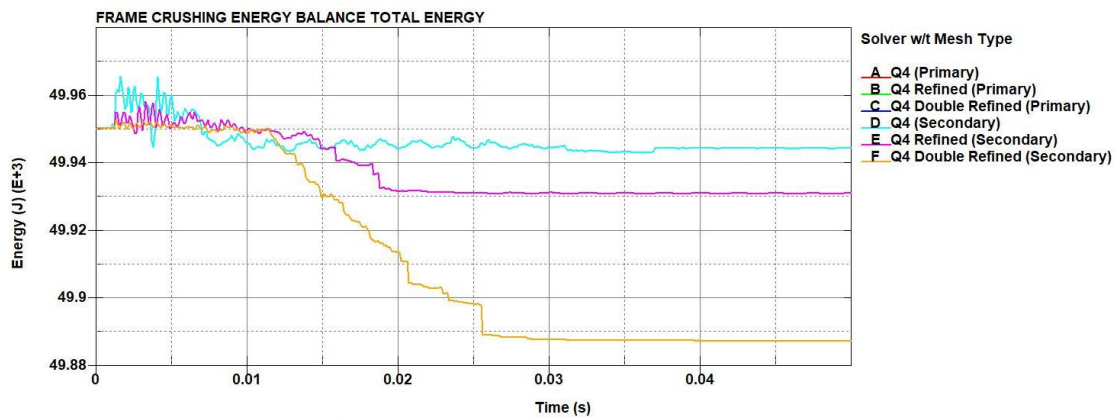


Figure 161 - Frame mesh refinement (*CONTROL_SHELL* influence) total energy of quadrilateral (top) and triangular (bottom) elements

From the results of the momentum (figure 162), not only the results on the triangular elements are affected but also the convergence. Finally, accessing visually the crashing behaviour of the model without the CONTROL_SHELL keyword during the impact at 5 ms only for the triangular elements (figure 163), since the impact behaviour without the control keyword is unaffected for the quadrilateral elements, the crashing behaviour resembles the behaviour in Europlexus, especially in the more refined cases. For the consideration of switching the element type into triangular elements, the modelling in LS-Prepost must be taken into caution on which part is going to be re-meshed, and to carefully assign the control cards in order to not affect the results. However, the quadrilateral element cases do not have the same sensitivity to the CONTROL_SHELL as the triangular element cases. In conclusion, the crushing behaviour of the frame is very dependent both on mesh element size, element type and solver specific keywords.

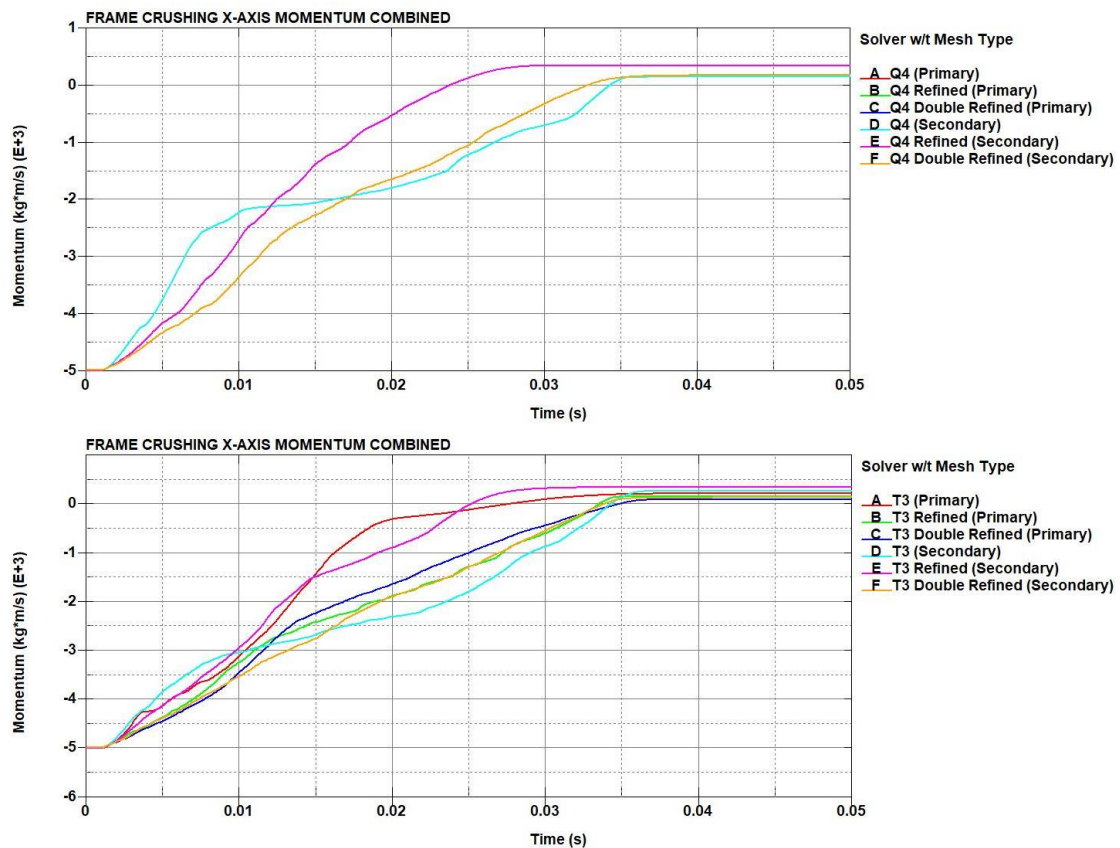


Figure 162 - Frame mesh refinement (CONTROL_SHELL influence) x-axis momentum of quadrilateral (top) and triangular (bottom) elements

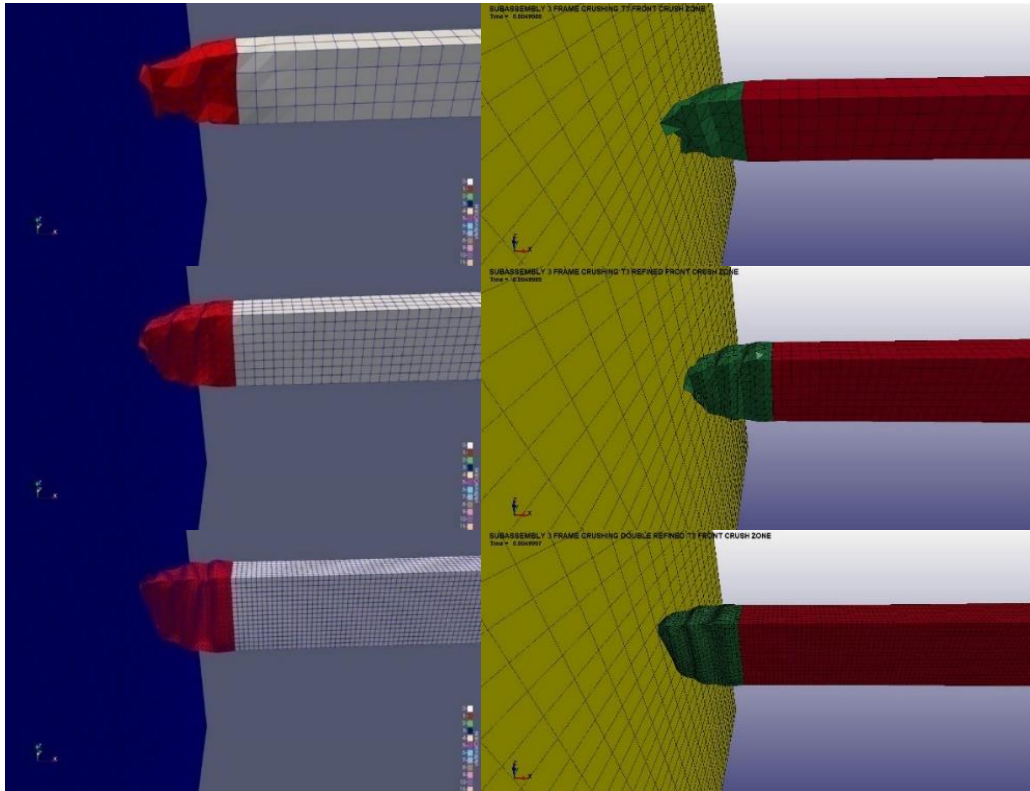


Figure 163 – Frame mesh refinement (*CONTROL_SHELL* influence) crushing behaviour @ 5 ms of triangular elements case of Europlexus (left) and LS-Dyna without control card (right) of original mesh (top), fine mesh (middle) and very fine mesh (bottom)

5.6.3. Submodel 3 remeshing

The last task in the is to perform a remeshing on the complete model (submodel 3) to access the sensitivity of the model by changing the mesh and the connections on the remeshed part (i.e., the constraint nodal rigid body (CNRB)). In these simulations all of the parameters are identical to the parameters in the original submodel 3 simulations. Since Europlexus gave doubtful results in those simulations, the current ones are performed only in LS-Dyna, checking the sensitivity of the performed modifications only in a single solver. The simulations are performed using the R12 double precision SMP version of LS-Dyna.

5.6.3.1. “Frame crush zone” remeshing without transitioning zone

In the first case study the element length is halved (from 30 mm to 15mm), but only on the “Frame crush zone” (part 3) (figure 164). Another modification is to change the constraint nodal rigid bodies on the remeshed part, by assigning the newly created nodes from the remeshing, on the *NODE_SETs* assigned to those CNRBs (figure 165). Thus, in this first step, there are three cases (with their respective denominations):

- Original version of the model as OV
- Remeshed version with unmodified CNRB as R_V1

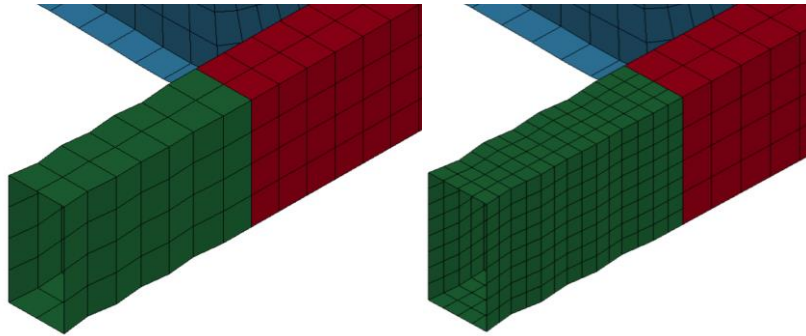


Figure 164 - Submodel 3 remeshing (without transitioning zone) original model (left) and modified model (right)

- Remeshed version with modified CNRB as R_V2

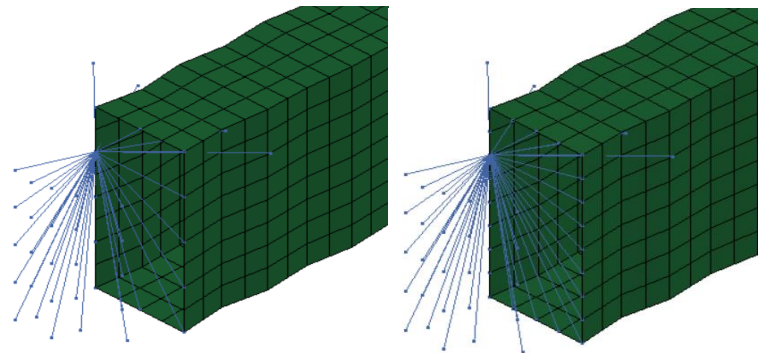


Figure 165 - Submodel 3 remeshing (without transitioning zone) modification on the CNRB connection on the remeshed version original connection (left) and modified connection (right)

The model that is used from the original simulation is the model as in the Case 1, the model with the connections just as the NI vehicle model first release. The remeshing influences the energy results (figure 166). The internal energy results are different in behaviour. This means that the internal energy distribution is different for the remeshed parts, as it is observed from

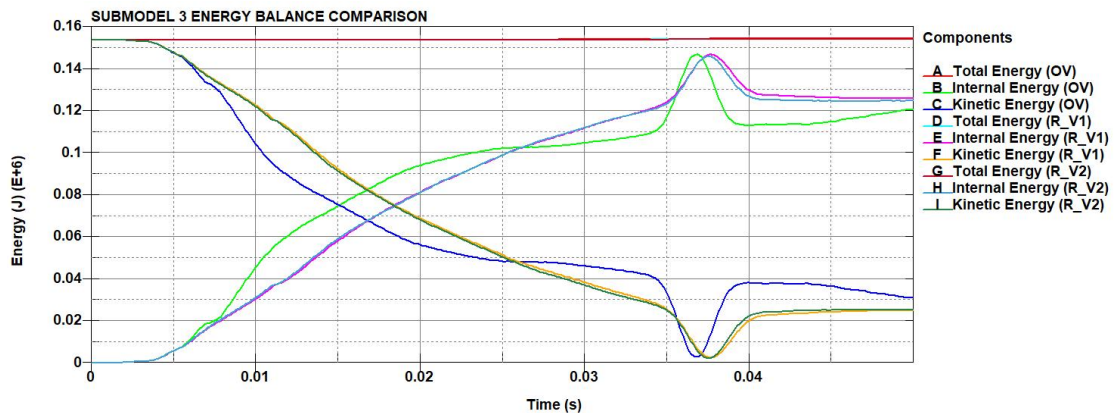


Figure 166 - Submodel 3 remeshing (without transitioning zone) energy balance

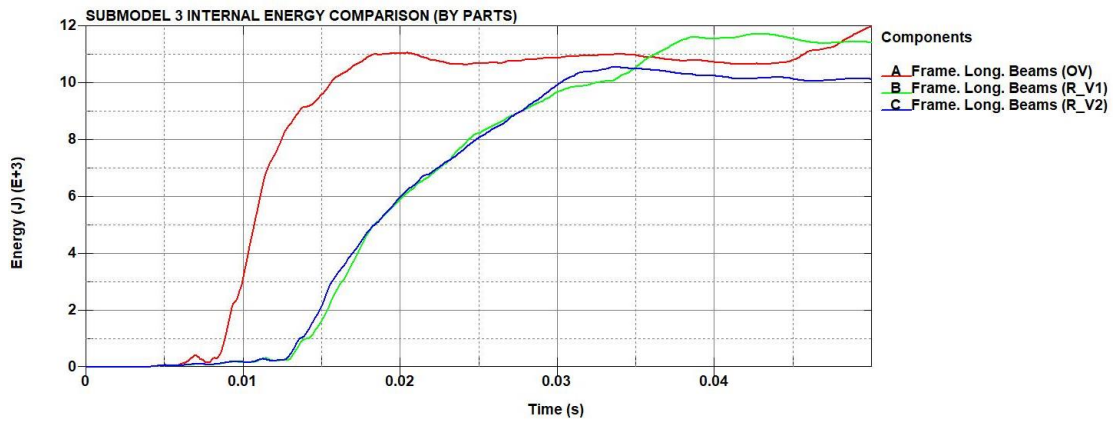


Figure 167 - Submodel 3 remeshing (without transitioning zone) "Frame longitudinal beams" internal energy



Figure 168 - Submodel 3 remeshing (without transitioning zone) "Frame cross member under engine" internal energy

of the internal energy of some components (figures 167 and 168). However, the two remeshed models (with modified and non-modified constraints) give practically identical results, especially before the engine hits the target. After the engine impact (at about 35–40 ms), the difference is more visible but remains globally acceptable. From the contact force and momentum results, the relative coarseness of the initial mesh of the "Frame crush zone" (part 3) introduces a significant artificial stiffness to the system. According to the contact force curves (figure 169), it is estimated that the force on the target obtained with the coarse mesh is about twice the force obtained with a refined mesh during the time interval from 5 ms to 15 ms. At the same time, the duration of the impact is similar for both mesh sizes. Thus, the average force on the target is similar since the total momentum is conserved (figure 170). In conclusion, the modification on the CNRBs do not give a different result than the unmodified one. However, the LS-Prepost software allowed the remeshing of the model, without creating a transitioning zone between

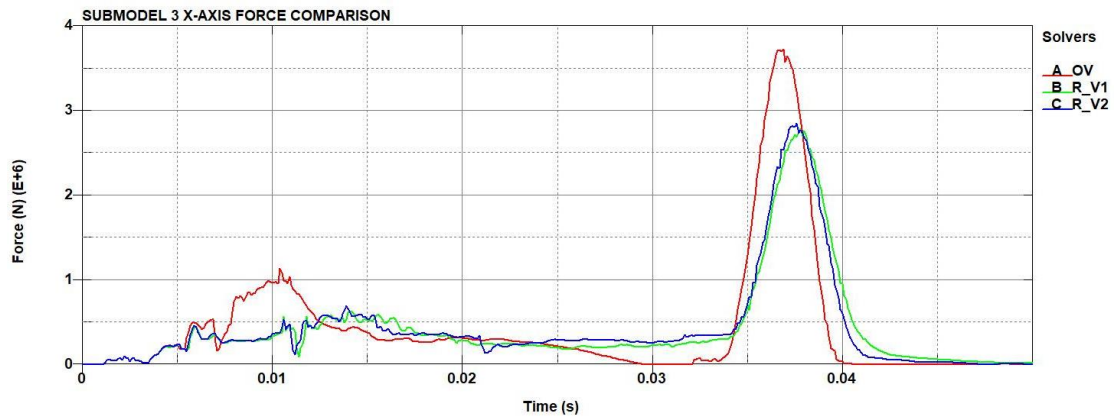


Figure 169 - Submodel 3 remeshing (without transitioning zone) x-axis contact force

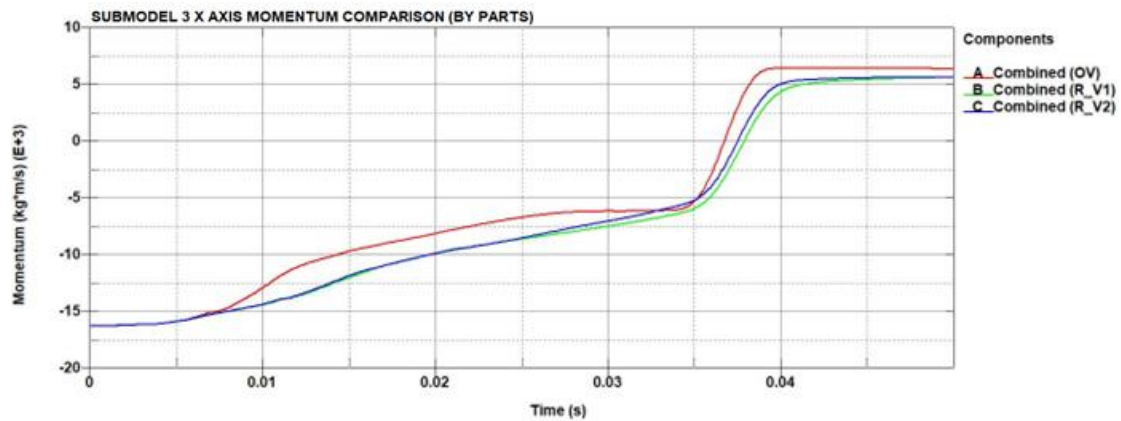


Figure 170 - Submodel 3 remeshing (without transitioning zone) x-axis momentum

the remeshed part and the frame with the coarse mesh, by fixing the new nodes on the edges of the elements of the coarse mesh.

5.6.3.2. "Frame crush zone" remeshing with transitioning zone

In order to guarantee that the parts are perfectly attached and a smooth transition from smaller to bigger elements, new simulations with revised mesh are performed. In these cases, the CNRBs are not modified since there is a relatively insignificant effect on the results with a single refinement and because the initial vehicle model was not conceived for easy mesh refinement, thus minimal modifications should be performed on the rest of the model (figure 171). Two types of remeshing are performed, as in the submodel 3 frame impact case:

- Original mesh (Avg. element size: 30 mm)
- Fine, with element size half of the original mesh (Avg. element size: 15mm)
- Very fine, with element size half of the fine mesh (Avg. element size: 7.5mm)

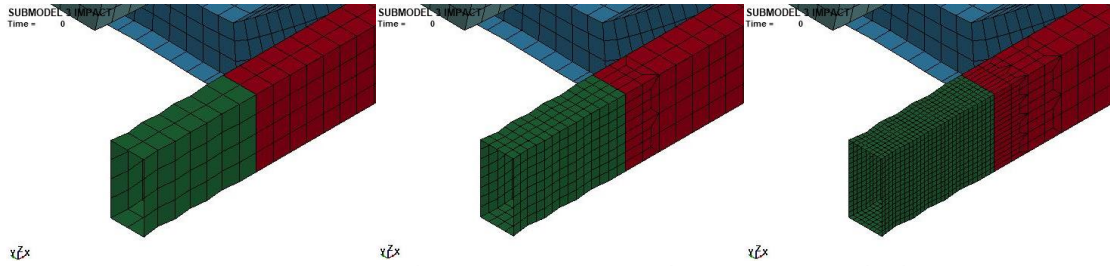


Figure 171 - Submodel 3 remeshing (with transitioning zone) original model (left), fine mesh model (middle) and finer mesh model (right)

In the new proposed cases, a transitioning zone on the “Frame longitudinal beams” (part 1) between the refined part and the coarse mesh of the frame is created to guarantee the connection of the new nodes to the frame. Again, the parameters are the same as in the submodel 3 case. The simulations are denoted as:

- Original version of the model as OV
- Fine version as R
- Very fine version as R_F

From the energy balance graph (figure 172) and in the internal energies of several components confirm the results on the submodel 3 frame impact,

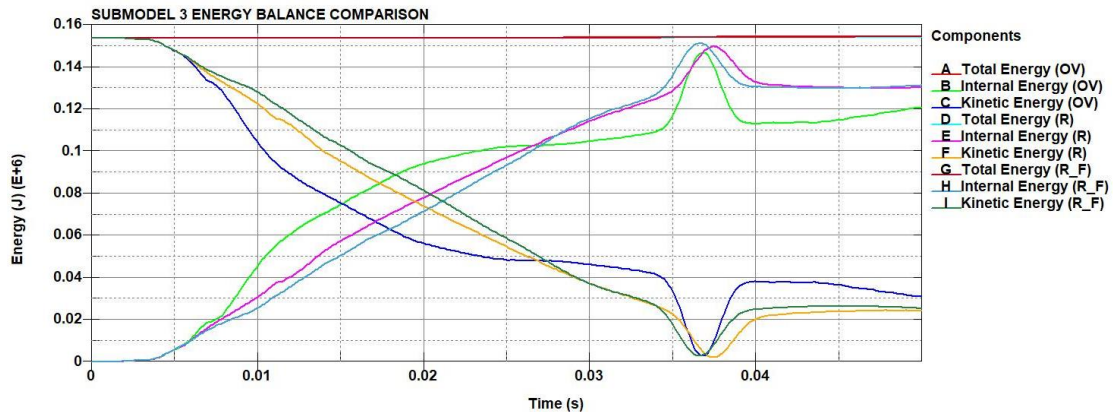


Figure 172 - Submodel 3 remeshing (with transitioning zone) energy balance



Figure 173 - Submodel 3 remeshing (with transitioning zone) “Frame longitudinal beams” internal energy

that the initial mesh of the frame is too coarse to correctly capture the crushing behaviour. In particular, the coarse mesh of the “Frame crush zone” underestimates the dissipated energy by about 30%, which has a direct consequence on internal energy distribution between different components (figures 173 and 174). The change in energy distribution can also be seen from the internal energy results of the engine surface (figure 175), where for the coarse mesh, more energy is left over for the engine, and therefore undergoes a more severe impact. However, the most important

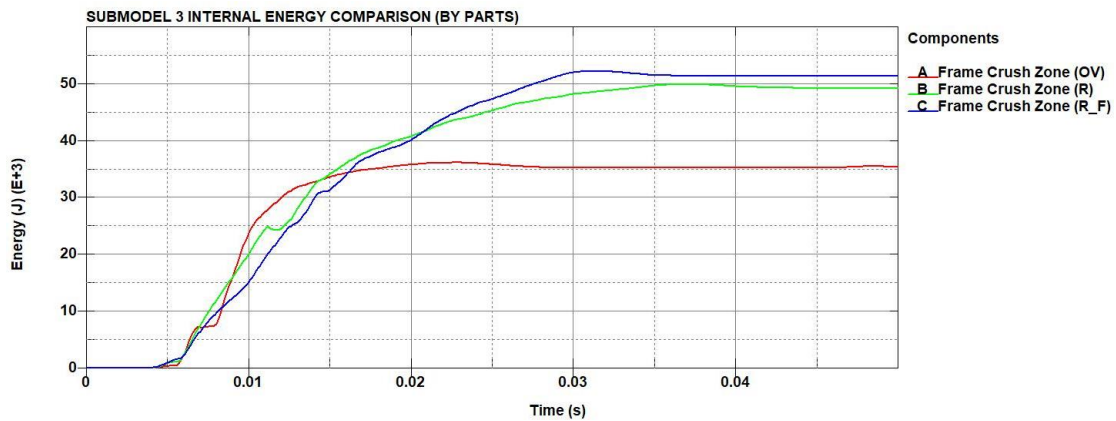


Figure 174 - Submodel 3 remeshing (with transitioning zone) “Frame crush zone” internal energy

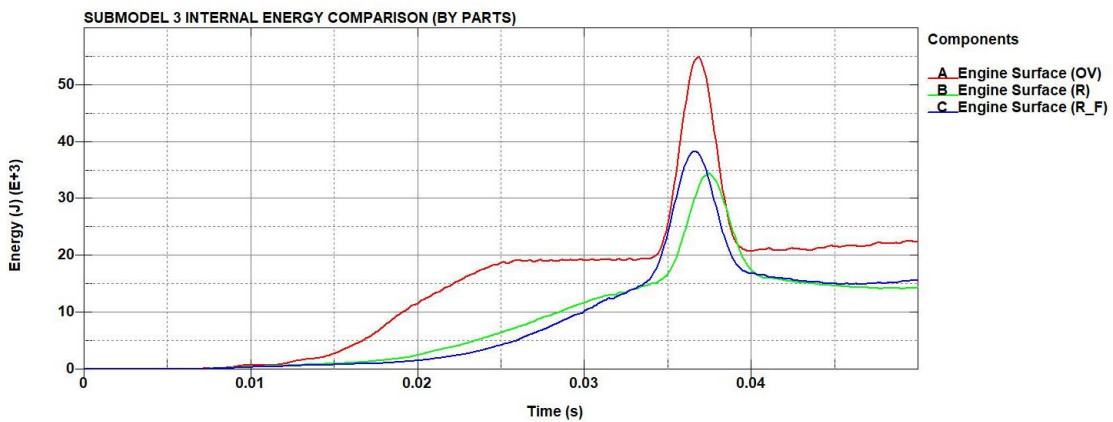


Figure 175 - Submodel 3 remeshing (with transitioning zone) “Engine surface” internal energy

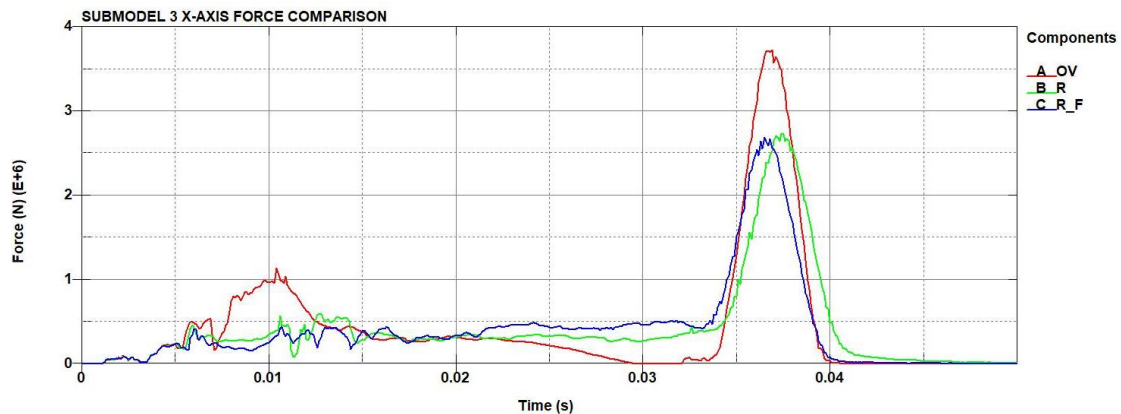


Figure 176 - Submodel 3 remeshing (with transitioning zone) x-axis contact force

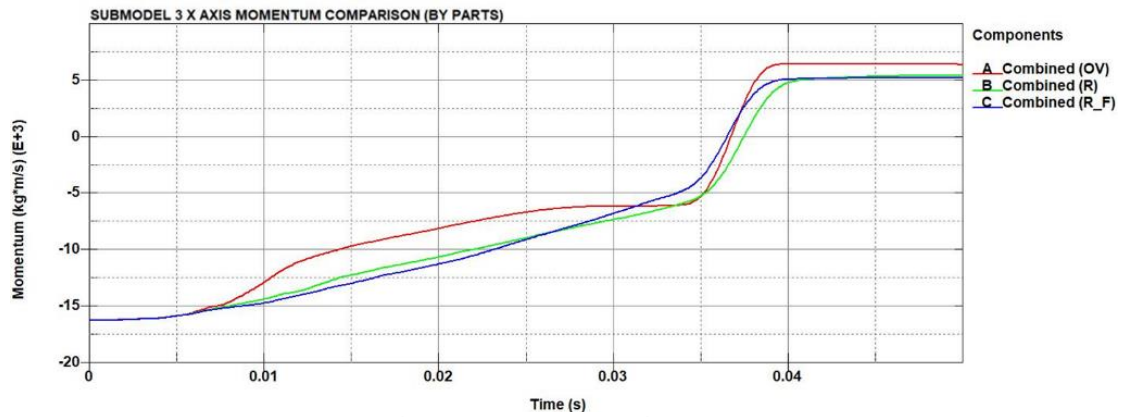


Figure 177 - Submodel 3 remeshing (with transitioning zone) x-axis momentum

consequence is that the coarse mesh model overestimates significantly the impact force on the target (figure 176), especially in the beginning of the crash from 5 ms to 15 ms. These high peaks should not be taken entirely into consideration, because the submodel 3 is not very realistic on simulating this point. Nevertheless, the coarse mesh overestimates also this peak. The momentum graph (figure 177) is also affected from the different mesh modification cases. A verification required to check the behaviour of the new created noded from the remesh (figure 178), which are not constrained by the CNRB, in order to verify their motion during the impact. Realistically the nodes should be constrained. However, from the figure 181 which display the

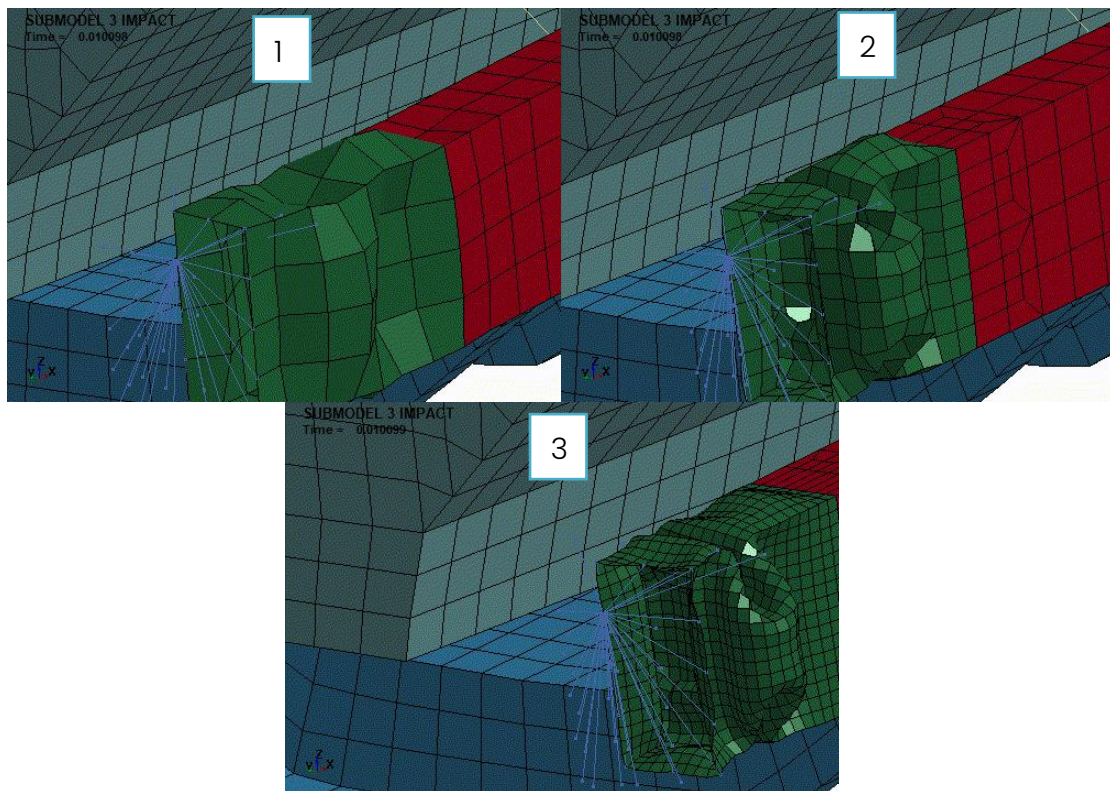


Figure 178 - Submodel 3 remeshing (with transitioning zone) crushing behaviour @ 10 ms of "Frame crush zone" part @ 1 ms on original model (1), fine mesh model (2) and finer mesh model (3)

impact of the frame at 1 ms, the unconstrained nodes do not appear to have irregular motion during the impact. The final aspect to be verified is the timestep of the simulation. Although the remeshing is very local and does not increase significantly the number of elements, reducing the minimum element size reduces also the critical time step. By verifying from the results of the simulation, the smallest timestep is:

- Coarse mesh: $3.0254 \cdot 10^{-6}$ s
- Fine mesh: $2.2053 \cdot 10^{-6}$ s
- Finer mesh: $1.1027 \cdot 10^{-6}$ s

As the mesh size decreases, the critical timestep also decreases, thus making the model slower. The NI vehicle model was conceived with the philosophy to be a fast and light model. However, from the results it is clear that a trade off in element size and speed must be performed for the sake of better accuracy.

6. Conclusion and future work

The purpose of this thesis was to contribute to the development of the NI vehicle model in order to achieve an accurate, fast model and readily available for the user. Initial work on a preliminary version of the NI vehicle model helped identify criticalities in the contact model used in the model, and in some components, in terms of the design as well as discretization of the components. Following the initial work on the preliminary model, the focus of the work was on the comparison of the two solvers, LS-Dyna and Europlexus. Initially working on a simple part (cross beam) extracted from the NI Generic Vehicle Model, the comparison began on a simple elastic material, where a dissipation of energy on the Europlexus solver due to its contact model with respect to LS-Dyna which preserved the energy. The next step was a comparison of the different element formulations (reduced and full integration). There is no exact equivalence between the two codes, because they both implement the same shell theory (Reisner-Mindlin) differently. The difference in the results between the two solvers can be considered acceptable. However, since Europlexus used a fully integrated scheme the results of the two solvers lied again on the energy dissipation due to the different contact model between the two solvers. By changing the

material law to elastoplastic with perfect plasticity and elastoplastic with hardening line, for different velocities it was observed that the behaviour of the two material laws displayed a similar behaviour in LS-Dyna when compared to Europlexus. More specifically for higher initial velocity, the difference of the results between the two solvers was smaller. The addition of mass on the part did not affect the results of LS-Dyna between the two element formulations. Thus, for the material parameters, a consistence between the two codes is confirmed. Following the comparison, a more complex model was introduced (submodel 1), comprised of 3 parts and rigid connections between the parts. The results obtained in the elastic case displayed small differences between the two solvers, however when switched to an elastoplastic material the results between the solvers were almost similar. In this model a mesh refinement was performed, where it was observed that the original model underestimated the internal energy i.e., absorbed less energy. The elastoplastic case gave more accurate contact force results between the two solvers, something not achieved on the crossbeam part or the original version of the submodel 1. In all the cases, the previously observed energy dissipation of Europlexus was present. The next step was to increase even more the complexity of the model (submodel 2), of a model comprising of six parts. The comparison of the elastic case gave different results between the two solvers, so the focus turned to the elastoplastic material, since it is more realistic for this purpose. In that case, there was an energy dissipation in the Europlexus solver due to the contact model used, for both the case of the same material applied to all the part and the case of the parts having the materials from the NI model. The results were acceptable, however, the main difference between the two solvers lied on the rotation of the model upon impact on the LS-Dyna. The reason is the rigid constraints on the model, which operate differently in Europlexus, by blocking some degrees of freedom. Thus, identifying the connection definition as a crucial parameter, that could affect the results the simulation. In order to compensate for these rotations, in the final step, the most complex version of the model (submodel 3), with 21 parts of different element type and additional connections introduced, was tested. Initial simulation was performed between two versions of the submodel 3, with some differences in the connections according to the model used by JRC and the connections in the NI vehicle model. Results between the two solvers were

different between them. The reason behind these differences, is how the rigid connections are defined in both solvers. The next step was to make a comparison on a model defined of three important parts of the submodel 3, in order to check how much the results are affected by mesh type and size. The comparison performed with quadrilateral vs triangular elements on three different mesh sizes displayed that the results of the quadrilateral elements have more stable results than the triangular elements. Because triangular elements are affected by specific keywords in LS-Dyna, caution must be used when assigning parts with triangular elements in the complete model. The mesh size affects the convergence time for both element types. Finally, a remesh was performed on specific parts on the submodel 3 to observe the global effect of the remeshing. The coarse mesh underestimated the internal energy by about 30%, as well as the contact force upon impact and was too coarse to correctly capture the crushing of the frame. However, the remeshing made the critical timestep smaller, which is a significant parameter to take into consideration for this model (and thus the complete NI vehicle model), since the original selection of the mesh size was performed in order to keep the critical timestep large, for a fast model. Future work can be performed on this model. The contact algorithm can be improved in order to avoid the dissipation of energy. Next, the rigid body constraints must be correctly defined, in order to accurately simulate the connection between elements without blocking some degrees of freedom. Also, a specific balance between accuracy of results and run time must be performed in order for the model to be fast enough, but also accurate in order to correctly estimate the impact upon a barrier. Due to the fact that heavier vehicles are mostly preferred as a terrorist attack median, generic models for vehicles of these categories can be developed, for further validation of the design of barriers when larger and heavier vehicles are used for terrorist attacks.

Acknowledgements

Today marks the end of a long cycle of studies, and the achievement of a goal that seemed impossible in the beginning. I would like to thank my family for the extreme support and encouragement they provided during my studies, especially in the tough times affected by the COVID-19 pandemic. I would also like to thank my friends Athena, Dimosthenis and Athanasios who listened to me, advised me, gave me hope and support to give my best and achieve my goal. A special thanks to the JRC institute, to Dr. Larcher Martin and Dr. Markovic Damijan for the opportunity to collaborate in this significant project. Finally, I would like to thank the Politecnico di Torino professors, represented by Professor Andrea Tonoli, for their teachings, and especially Professor Alessandro Scattina for the opportunity of this thesis, as well as the diligence and support provided to me in the whole duration, but most of all his personal strive to help me grow as an engineer.

Grigorios Theodoridis

December 2022

Bibliography

- [1] Meriam-Webster.com, "Definition of word "barrier"," [Online]. Available: <https://www.merriam-webster.com/dictionary/barrier>. [Accessed 2022 June 13].
- [2] V. Karlos and M. Larcher, "Guideline: Building Perimeter Protection: Design recommendations for enhanced security," European Commission, Ispra, Italy, 2020.
- [3] M. T. & M. Company, "The Benefits of Finite Element Analysis in Manufacturing," [Online]. Available: <https://www.manortool.com/finite-element-analysis>.
- [4] Europlexus, "EPX short description," [Online]. Available: <http://www-epx.cea.fr/index.php/what-is-epx>.
- [5] V. Faucher, "Advanced parallel strategy for strongly coupled fast transient fluid-structure dynamics with dual management of kinematic," 2013.
- [6] Europlexus, "Structural dynamics," [Online]. Available: <http://www-epx.cea.fr/index.php/what-is-epx/7-structural-dynamics>.
- [7] G. Valsamos, M. Larcher, F. Casadei and G. Karlos, "A numerical framework to support the certification of barrier testing," European Commission, Ispra, Italy, 2020.
- [8] G. G. L. B. D. HALLQUIST J. O., "Sliding interfaces with contact-impact in large scale Lagrangian computation," *Computer Methods in Applied Mechanics and Engineering*, vol. Vol. 11, p. 107-135, 1985.
- [9] Livemore Software Technology, LS-Dyna R12 keyword user's manual, vol. 1, AES, 2020.

- [10] Dynamore, "Crashbox example," [Online]. Available: <https://www.dynaexamples.com/introduction/intro-by-j.-reid/crashbox>).
- [11] C. F., "A General Impact-Contact Algorithm Based on Hierarchic Pinballs for the EUROPLEXUS Software System," JRC Technical Note, 2003.
- [12] J. R. C. (JRC), "N1 vehicle model," in *4th Workshop*, Ispra, 2021.
- [13] "Highway barriers," TATA Steel, [Online]. Available: <https://www.tatasteleurope.com/construction/products/other/high-way-engineering/barriers>.
- [14] Reliance Foundry, "8 Reasons Why Cities are Installing Bollards in High Traffic Areas," [Online]. Available: <https://www.reliance-foundry.com/blog/bollards-in-high-traffic-areas>.
- [15] AFP, "Vehicle-ramming attacks," [Online]. Available: https://interactive.afp.com/graphics/vehicle-ramming-attacks_214/.
- [16] RS Security Consulting, "Vehicle Crash Barriers," [Online]. Available: <http://www.rssecurityconsulting.com/products/vehicle-crash-barriers/>.
- [17] Archiproducts, "ACKORD by Nola Industrier," [Online]. Available: https://www.archiproducts.com/en/products/nola-industrier/fixed-reinforced-concrete-bollard-ackord_96646.
- [18] Crowd Control Warehouse, "Plain Concrete Jersey Barrier," [Online]. Available: <https://www.crowdcontrolwarehouse.com/products/plain-concrete-jersey-barriers>.
- [19] Securiscape, "HVM Planters," [Online]. Available: <https://www.securiscape.co.uk/hvm-planters/>.

- [20 Amtrac, "Security Barriers," [Online]. Available:
] <https://www.amtrac.com.hk/security-barriers>.
- [21] LEDA Security, "Retractable bollard system," [Online]. Available:
<https://www.ledasecurity.com.au/retractable-bollard-system/>.
- [22 G. McEwan, "How practical are trees as an alternative to hard barriers
] in protecting public spaces?," HortWeek, [Online]. Available:
<https://www.hortweek.com/practical-trees-alternative-hard-barriers-protecting-public-spaces/arboriculture/article/1443274>.
- [23 Hiphen Solutions, "Rising Kerb Road Blocker," [Online]. Available:
] <https://hiphensolutions.com/rising-kerb-road-blocker/>.
- [24 Α. Κωβαίος, "Η Παράνομη είσοδος στη Βουλή και ο χειρότερος εαυτός μας,"
] Reporter, [Online]. Available: <https://www.reporter.gr/Apipseis/Apo-theseis/Aggelos-Kwbaios/474702-H-paranomh-eisodos-sth-Boylh-kai-o-cheirotos-eaytos-mas>.
- [25 Architecture and Design, "Crash tested speed gates for high security
] buildings," [Online]. Available:
<https://www.architectureanddesign.com.au/suppliers/leda-security-products/crash-tested-speed-gates-for-high-security-buildin>.
- [26 What is piping, "Introduction to Stress-Strain Curve," [Online]. Available:
] <https://whatispiping.com/stress-strain-curve/>.